UNIVERSITY OF SOUTHAMPTON

Faculty of Engineering, Science and Mathematics

School of Mathematics

# Asymptotically Null Slices in Numerical Relativity

by

David Matthew Hilditch

Submitted for the degree of Doctor of Philosophy

October 2007

UNIVERSITY OF SOUTHAMPTON

Faculty of Engineering, Science and Mathematics
School of Mathematics

Doctor of Philosophy

ABSTRACT

# Asymptotically Null Slices in Numerical Relativity

by David Matthew Hilditch

The work in this thesis concerns numerical evolution of the equations of General Relativity. The motivation is towards astrophysics through the choice of coordinates adapted to outgoing gravitational waves far from the strong-field region of a given spacetime. These asymptotically null coordinates allow a large region of spacetime to be evolved at a negligible computational cost.

The behavior of various gauge conditions (coordinate choices) can be studied without the resorting to the Einstein equations, but instead evolving coordinates on a known background. This "pure-gauge" approach is used to find gauge conditions suitable for evolving asymptotically null initial data.

Breakthroughs in numerical relativity have relied on a constraint damping technique. In the work that follows constraint damping is used to evolve asymptotically null initial data with various formulations of the Einstein equations.

Characteristic analysis of a given formulation allows for the construction of maximally dissipative and constraint preserving boundary conditions; such conditions are implemented and studied numerically on both flat and asymptotically null slices.

# Contents

List of Figures . . . . . i

List of Tables . . . . . vii

Declaration of authorship . . . . . ix

Acknowledgements . . . . . x

**1 Introduction** **1**

1.1 Numerical Relativity . . . . . 1

1.2 Asymptotically null slices . . . . . 3

1.3 End-states of evolved gauge conditions . . . . . 4

1.4 Thesis overview . . . . . 4

**2 Partial Differential Equations** **7**

2.1 Classification and Characteristics . . . . . 7

2.2 Evolution Problems . . . . . 9

2.2.1 Strong and symmetric hyperbolicity . . . . . 9

2.2.2 Matrix notation . . . . . 12

2.3 Well-posedness of the Cauchy Problem . . . . . 13

**3 Asymptotic Flatness** **15**

3.1 Conformal compactification of Minkowski spacetime . . . . . 15
3.2 Conformal compactification of Schwarzschild spacetime . . . . . 17
3.3 The formal definition of asymptotic flatness . . . . . 20

**4 The 3 + 1 Formalism** **22**

4.1 Foliations of spacetime . . . . . 23
4.2 The wave equation . . . . . 27
4.3 The ADM decomposition . . . . . 28
4.4 Hyperbolic Reformulation . . . . . 29
4.4.1 A toy problem . . . . . 30
4.4.2 Z4 . . . . . 32
4.4.3 NOR . . . . . 33
4.4.4 BSSN . . . . . 34
4.5 Gauge conditions . . . . . 37
4.6 Spherical reduction . . . . . 39
4.6.1 Reduction method . . . . . 40
4.6.2 Z4 . . . . . 42
4.6.3 NOR . . . . . 44
4.6.4 BSSN . . . . . 45
4.7 Constraint damping . . . . . 48
4.7.1 Damping terms . . . . . 49
4.7.2 Mode analysis . . . . . 50

**5 Mathematical analysis of asymptotically null slices** **52**

5.1 Introduction . . . . . 52

5.2 Mathematical analysis . . . . . 56

5.2.1 Spherically symmetric slices in Minkowski spacetime . . . . 56

5.2.2 Stability conditions . . . . . 57

5.2.3 Slicing, stretching, compactification, and lightcones . . . . . 59

5.2.4 Global structure . . . . . 61

5.2.5 Reissner-Nordström spacetime . . . . . 62

5.2.6 Characterisation of $n$ in terms of 3+1 variables . . . . . 71

5.2.7 Closed form coordinate transformations . . . . . 72

**6 Scalar field evolutions on asymptotically null slices** **74**

6.1 Method . . . . . 74

6.1.1 Grid and algorithm . . . . . 74

6.1.2 Outer boundary treatment . . . . . 75

6.1.3 Initial data, error and convergence . . . . . 76

6.2 Spherical wave equation on Minkowski spacetime . . . . . 78

6.2.1 Wave equation and boundary conditions . . . . . 78

6.2.2 Numerical boundary reflections . . . . . 79

6.2.3 Accuracy results . . . . . 80

6.3 Spherical wave equation on Schwarzschild spacetime . . . . . 87

6.3.1 Algorithm . . . . . 87

6.3.2 Tail results . . . . . 87

6.4 Conclusions . . . . . 94

**7 Pure gauge evolutions on asymptotically null slices** **98**

7.1 The pure gauge system . . . . . 98

7.1.1 Equations . . . . . 98

7.1.2 Hyperbolicity of the pure gauge system . . . . . 99

7.2 Evolutions on asymptotically null slices . . . . . 101

**8 Einstein equations on asymptotically null slices** **108**

8.1 Asymptotically null initial data . . . . . 108

8.2 Boundary conditions . . . . . 110

8.2.1 Construction method . . . . . 111

8.2.2 Maximally dissipative boundary conditions . . . . . 113

8.2.3 Constraint preserving boundary conditions . . . . . 119

8.2.4 Numerical tests of boundary conditions on flat slices . . . . 122

8.3 Numerical constraint damping tests . . . . . 127

8.4 Bona-Massó lapse conditions in blackhole space-times . . . . . 131

8.4.1 Numerical evolution of black hole spacetimes . . . . . 132

8.4.2 Killing coordinates on Schwarzschild spacetime in spherical symmetry . . . . . 138

8.4.3 Compatibility of Killing coordinates with BMn slicing on Schwarzschild spacetime . . . . . 139

8.4.4 Initial data . . . . . 141

8.4.5 Black hole evolutions . . . . . 143

8.4.6 Discussion . . . . . 152

8.5 Evolution of asymptotically null slices . . . . . 155

8.5.1 Spherical NOR . . . . . 155

8.5.2 Spherical BSSN . . . . . 163

8.5.3 Discussion . . . . . 167

**9 Conclusions** **169**

# List of Figures


3.1 The standard conformal diagram of Minkowski spacetime. . . . . 18

3.2 The standard conformal diagram of Schwarzschild spacetime. . . . . 20

4.1 Nearby spatial hypersurfaces of a foliation. . . . . 27

5.1 A schematic spacetime diagram to illustrate that if the artificial outer boundary is pushed out to sufficiently large radius (here $R = 2000M$) outgoing gravitational radiation can be read off at very large radius (here $R = 1000M$) for a long time (here $t = 1000M$) without being contaminated by unphysical BCs at the artificial outer boundary (assuming that no information travels faster than light). . . . . 55

5.2 $n = \frac{1}{2}$ slices plotted with $L = 1$ up to $R = 9$. The diagonal line is the boundary of the domain of dependence of the initial data. Slices with other $n$ look similar. 63

5.3 Flat ($n = 0$) slices plotted in the standard conformal diagram. The outer boundary radius and the domain of dependence of the initial data have been indicated, but the slices have been extended beyond $R_{\max}$ to infinite radius to demonstrate that they reach spacelike infinity. . . . . 64

5.4 $n = \frac{1}{2}$ slices. The slices end at spacelike infinity. . . . . 65

5.5 $n = 1$ slices embedded in the standard conformal diagram of Minkowski. They approach spacelike infinity tangential to future null infinity. . . . . 65

5.6 $n = \frac{3}{2}$ slices intersect future null infinity at finite retarded time. . . . . 66

5.7 $n = 2$ slices also intersect future null infinity at finite retarded time. . . . . 66

5.8 Coordinate speeds $c_+$ and $c_-$ in our examples with with $L = 1$, and $n = 1/2$ and $n = 1$ (dashed). Here $R = \infty$ corresponds to $r = \infty$. . . . . 67

5.9 Coordinate speeds $c_+$ and $c_-$ in our examples with $l = 1$ and $n = 3/2$ and $n = 2$ (dashed), so that $R = \infty$ corresponds to $r = 1$. . . . . 68

5.10 Coordinate speeds $c_+$ and $c_-$ in Kerr-Schild slicing. Here and in the following the black hole mass is $m = 1$. . . . . 68

5.11 Coordinate speeds $c_+$ and $c_-$ in modified Painlevé-Güllstrand slicing. . . . . 69

5.12 Coordinate speeds $c_+$ and $c_-$ in modified Kerr-Schild slicing, made asymptotically null with $n = \frac{1}{2}$ and $n = 1$ (dashed). $L = 1$ in both cases. . . . . 69

5.13 Coordinate speeds $c_+$ and $c_-$ in modified Painlevé-Güllstrand and $n = \frac{1}{2}$ and $n = 1$ (dashed). Again $L = 1$. . . . . 70

5.14 Coordinate speeds $c_+$ and $c_-$ in modified Kerr-Schild and $n = \frac{3}{2}$, with $l = 20$. . 70

5.15 Coordinate speeds $c_+$ and $c_-$ in modified Painlevé-Güllstrand and $n = \frac{3}{2}$. Again $l = 20$. . . . . 71

6.1 The error in $\phi$ for flat slicing at $R_* = 10$. $e(t, r_*)$ at $\Delta r = 0.1$ and $4e(r, t_*)$ at $\Delta r = 0.05$ are both plotted, but are indistinguishable here. . . . . 81

6.2 Error in $\phi$ for flat slicing at $R_* = 100$. . . . . 81

6.3 Error in $\phi$ for flat slicing at $R_* = 1000$. . . . . 82

6.4 Error in $\phi$ with $n = \frac{1}{2}$ and $L = 2.0$. The three coordinate times correspond to $R_* = 10, 100, 1000$ here and in the following plots. . . . . 82

6.5 Error in $\phi$ with $n = 1$ and $L = 5.77$. . . . . 83

6.6 Error in $\phi$ with $n = \frac{3}{2}$ and $L = 8.9$. . . . . 83

6.7 Error in $\phi$ with $n = 2$ and $L = 11.8$. The final coordinate time corresponds to $R_* = \infty$, at which the solution is still 2nd order accurate and remains so until late times, when error induced at the boundary directly after $R_* = \infty$ propagates to the central region. . . . . 84

6.8 Rescaled error plot in $\phi$ with $n = \frac{3}{2}$ and $L = 8.9$ at $R_* = \infty$. . . . . 84

6.9 Log-log plots of $\phi(t)$ and $\Pi(t)$ at $R = 10$ on Schwarzschild spacetime with $m = 1$, using standard Kerr-Schild slices (that is $n = 0$). The straight lines are $t^{-3}$ and $t^{-4}$, the expected power-law fall-off for the tails in $\phi$ and $\pi$, with an overall constant fixed to match the numerical data. The power-law tails are clearly visible at late times, after the outgoing wave has passed the observer. They are overwhelmed by spurious continuum reflections from the boundary. . 89

6.10 As in the previous plot, but at $R = 500$. . . . . 90

6.11 As in the previous plots, but with $n = 1/2$ slices, at $R = 10$. Here, and in all following $n > 0$ plots, the tails are overwhelmed by spurious numerical reflections from the boundary which propagate in faster than light. . . . . 90

6.12 As in the previous plots, but with $n = 1/2$ slices, at $R = 500$. . . . . 91

6.13 As in the previous plots, but with $n = 1$ slices, at $R = 10$. . . . . 91

6.14 As in the previous plots, but with $n = 1$ slices, at $R = 500$. . . . . 92

6.15 As in the previous plots, but with $n = 3/2$ slices, at $R = 10$. . . . . 92

6.16 As in the previous plots, but with $n = 3/2$ slices, at $R = 500$. . . . . 94

7.1 The Minkowski spacetime asymptotically null initial data (appropriately rescaled). $\gamma_{rr}$ is not an evolved variable but a derived quantity. The evolved $T$ field is not shown. . . . . 103

7.2 A snapshot of the evolution of asymptotically null coordinates on Minkowski spacetime at $t = 1000$. The evolution was made using the gauge condition (7.21) for the lapse and the area locking shift condition (4.88) for the shift. The feature at the outer boundary is caused by the numerical outer boundary conditions in which the evolved variables are overwritten by data from the exact solution. Eventually the feature grows large enough to prevent further evolution. . . . . 104

7.3 A snapshot as in Fig. 7.2 but now with the gauge conditions (7.21, 7.22). Again the feature at the outer boundary is caused by the outer boundary conditions. . 105

7.4 The Kerr-Schild asymptotically null slice (rescaled as in fig 7.1). . . . . 106

7.5 A snapshot of the evolution of the data shown in Fig. 7.4 at $t = 1000$ with (4.88,7.21). . . . . 106

7.6 As in Fig. 7.5 with (7.21,7.22). . . . . 107

8.1 *left:* Second order pointwise convergence of spherical NOR with $\rho = 2$, densitized lapse, fixed shift and maximally dissipative boundary conditions. *right:* Pointwise convergence of spherical NOR with $\rho = 1$, BMn lapse, fn-driver shift and maximally dissipative boundary conditions. Similar results are found with a densitized lapse, fixed shift and $\rho \neq 2$. . . . . 125

8.2 *left:* Second order pointwise convergence of spherical NOR with $\rho = 1$, densitized lapse, fixed shift and constraint preserving boundary conditions. *right:* Incoming constraint violation with maximally dissipative and constraint preserving boundary conditions. . . . . 125

8.3 *left:* As in Fig. 8.1:(*right*) with the modified condition (8.82). *right:* Incoming constraint violation with the modified maximally dissipative condition. . . . . 126

8.4 As in Fig. 8.1:*left* but with the BSSN system, densitized lapse and fixed shift. (*left:*) second order scheme. (*right:*) fourth order scheme. . . . . 127

8.5 As in Fig. 8.1:*left* but with the BSSN system, BMn lapse and gamma-driver shift. (*left:*) second order scheme. (*right:*) fourth order scheme. . . . . 128

8.6 The NOR constraints with and without damping, with fixed lapse and densitized shift . . . . . 129

8.7 The NOR constraints with and without damping with BMn lapse and fn-driver shift (with sources). . . . . 130

8.8 The BSSN constraints with and without damping with densitized lapse and fixed shift. $\kappa = 0.2$ was taken in the damped runs. . . . . 130

8.9 The BSSN constraints with and without damping with BMn lapse and gamma-driver shift. $\kappa = 0.2$ was taken in the damped runs. . . . . 131

8.10 Spacetime diagram of the Schwarzschild spacetime, with the angular coordinates suppressed. The horizontal line from $i^0_L$ to $i^0_R$ is the time-symmetric wormhole slice typically used as initial data in puncture evolutions of a Schwarzschild black holes. The curved lines schematically represent the slicing generated from these initial data by BMn lapse with $\alpha = 1$ initially. They approach the slice $R = R_0$, which links $i^+_L$ to $i^+_R$. The vertical dashed line represents the symmetry boundary which can replace the left-right reflection symmetry of this slicing. As the slices approach $R = R_0$, the approximately cylindrical wormhole grows longer linearly with time. . . . . 133

8.11 The same spacetime diagram, schematically showing a Killing slicing that ends at the future singularity, such as Kerr-Schild slices. The lines with arrows are trajectories of the Killing vector (lines of constant $R$) and the beads on them represent surfaces of constant coordinate $r$ if the Killing shift is used. In particular, the dashed line could serve as a Killing excision boundary. . . . . 134

8.12 The same spacetime diagram, schematically showing the unique regular spherical Killing slicing that is compatible with BMn slicing (for a given $\mu_L(\alpha)$). All slices are isometric to one another, and connect $i_L^+$ with $i_R^0$. The again asymptote to the slice $R = R_0$. . . . . 136

8.13 Schematic spacetime diagram of the collapse of a spherical star. Outside the collapsing star (shaded) the spacetime is Schwarzschild, comprising parts of regions R and F. A Killing slicing with excision as in Fig. 8.11 is shown. A Killing endstate cannot be reached without excision. . . . . 137

8.14 The $L^2$ distance of the lapse from the Killing endstate over the range from the excision boundary $R = 1.54$ (just inside the regular singular point) out to $R = 21.54$, with area locking shift. The power law decay indicates $||\alpha - \alpha_{\text{Killing}}|| \sim t^{-1}$. 145

8.15 The $L^2$ distance of the lapse from the Killing endstate from the excision boundary with approximately the same limits as in Fig. 8.14, using the fn shift driver (4.94). The power law decay again indicates $||\alpha - \alpha_{\text{Killing}}|| \sim t^{-1}$. . . . . 146

8.16 Snapshots of $R$ and $\alpha$ against proper distance $l$ from an evolution of an isometric slice as constructed in the "wormhole initial data" subsection 8.4.4. The throat of the slice (initially at $R = 1.5M$) is gradually stretched so that it becomes an infinitely long cylinder. The radius of the cylinder agrees with that computed in [48]. Note that low numerical resolution effectively smears out a gauge shock travelling left, so that this is not a correct continuum solution. The evolution was made with the spherical pure gauge system. . . . . 149

8.17 The $K = 0$ time symmetric slice through the bifurcation surface of Schwarzschild, evolved with BMn 1+log slicing, with $\alpha = 1$ initially. We show a snapshot of $K$ and $\alpha$ against proper distance radius. The edge at $r \simeq 7$ in this snapshot moves to the right, and leaves behind a cylinder of constant $R$ and $K$ with $\alpha \simeq 0$. The evolution was made with the full spherical NOR system. . . . . 150

8.18 As in Fig. (8.17), but with $\alpha$ not constant on the initial slice. The wave on the left travels left and is steepening, about to form a gauge shock, with large negative $K$. The wave on the right travels right and is also steepening: note $\alpha'' > 0$ there. . . . . 151

8.19 The $l2$ norm of the time derivative of the numerical solution. All dynamics cease by $t \simeq 600$. . . . . 156

8.20 Convergence factors for the second and fourth order accurate schemes. The evolutions also display perfect pointwise convergence to the appropriate order. . 157

8.21 This plot compares the growth of constraints on asymptotically null slices in the Minkowski spacetime with and without damping. Clearly damping is essential to keep the constraints under control on asymptotically null slices. . . . . 158

8.22 The plot shows the outgoing gauge perturbation at different times. The lapse was perturbed by a gaussian of width one, amplitude $1\text{x}10^{-4}$ centered at the origin. The perturbation leaves the grid with no boundary reflection whatsoever. 159

8.23 This plot shows initial data for asymptotically null evolutions in the Schwarchzschild spacetime. . . . . 163

8.24 This plot shows a snapshot of the data from Fig. (8.23) during the evolution. The slow growth of variables at the excision boundary can be seen. It is this growth that eventually kills the run. The far region of the slice is effectively frozen after about $t \sim 100M$. . . . . 164

8.25 $\phi$, $\bar{\gamma}_{rr}$, $\bar{\gamma}_T$ and $K$ with $\tau(r) = r$, on an $n = 1$ asymptotically null slice in Minkowski. Note that $\phi$ (blue) grows linearly, whilst $\bar{\gamma}_{rr}$ diminishes ($\bar{\gamma}_T$ grows) exponentially. . . . . 165

8.26 As in Fig. 8.25 with $\tau(r) = R(r)(1+(2R(r)/L)^2)^{-1/4}$. $\phi$ still grows linearly, but $\bar{\gamma}_{rr}$ and $\bar{\gamma}_T$ remain regular at large radius. . . . . 166

# List of Tables

6.1 Computational costs and errors for different slicings. . . . . 86

6.2 $t_d$ (time when the observer leaves the domain of dependence), $t_r$ (time when the reflection of the outgoing wave from the boundary reaches the observer) and $t_l$ (time when the tails are lost) for different slicings and two observer locations. Note that $T = t + \text{const}$ for these observers at fixed $R$, where the constant depends on $R$ and the slicing. "–" means this BC was not implemented. "*" means with this BC tails were not seen. The figures in boldface correspond to the figures. . . . . 93

8.1 $L_2$ distances of the perturbed solution from the static solution. With a very small perturbation, numerical error dominates the distance. These tests were made with the fourth order accurate scheme. . . . . 160

8.2 Comparing evolution of asymptotically null and flat slices. The evolutions of Minkowski on with flat slices were given an initial gaussian perturbation in the lapse to avoid trivial evolution. The amplitude of the pulse was $1\text{x}10^{-5}$ and it was centered initially at the origin. †: similar behavior can be seen as in the lower resolution case. 162

# Acknowledgements

Firstly I would like to thank my supervisor, Dr. Carsten Gundlach for his invaluable support and insight.

I would also like to thank the Southampton Relativity group as a whole for making my time here so enjoyable. My thanks particularly go to those who made me feel so welcome when I arrived, and to Darren Golbourne for proof reading my thesis.

I am grateful for the support and encouragement that my family have shown me; especially my mum for putting up with me in recent months.

Finally my thanks go to Rebecca (and Wizard); without your patience and love I could not have made it.

# Chapter 1

# Introduction

## 1.1 Numerical Relativity

General Relativity is a theory of gravity in which space and time are given a manifold structure with gravity represented by curvature. The curvature at a point is determined by the matter present. The Einstein field equations $G_{ab} = 8\pi T_{ab}$ are a system of 10 coupled nonlinear partial differential equations (PDEs) for the metric of the spacetime. The field equations are difficult to solve analytically without strong assumptions of symmetry. Often it is impossible to find solutions.

A major prediction of General Relativity still to be confirmed is the existence of gravitational waves; ripples in the spacetime manifold caused by the gravitational interaction of massive objects. Experiments to find such waves are currently being built, but gravitational waves are so weak that detection will require a technique called matched filtering. Matched filtering works by taking a template signal and calculating the probability that such a signal was present in experimental data. Whilst post-Newtonian methods can be used to describe the early stages of the merger of massive objects and perturbation techniques can be used to model the ringdown of the merged body, only fully numerical relativity can be used to describe

the merger itself.

For numerical solution the Einstein field equations are typically rewritten as an initial value problem with constraints. Constraint satisfying initial data representing some astrophysical situation must then be computed, a tricky task in its own right, because the Einstein constraint equations are a set of four coupled nonlinear PDEs in their own right. With a sensible choice of coordinates, the data can be evolved to find approximate solutions at later times. This approach is called free evolution because the constraints are solved once only; subsequent numerical error may violate them. An alternative is constrained evolution in which the constraints are enforced at every time-step.

The constraints allow the field equations to be written in versions of a fundamentally different character. Some of these formulations give rise to well-posed initial value problems whereas others do not. A well-posed initial value problem is one whose solutions exist, are unique and depend continuously on specified data. In a sufficiently simple context well-posed problems can be characterized completely in terms of an algebraic property called hyperbolicity. Hyperbolic systems are in some sense wave-like; physical effects travel with finite speed.

Once a formulation is chosen, approximate solutions can be garnered by for example representing fields over space at a finite number of points (grid-points) and approximating derivatives in space by finite differences. Known time derivatives can then be constructed and integrated numerically using (for example) the Runge-Kutta or Crank-Nicholson algorithms.

It is essential that numerical evolutions can run long enough to describe physical phenomena of interest and that they converge to a solution of General Relativity in the limit of high resolution (many grid-points). Well-posedness of the initial value problem is necessary for these properties, but the story is far from simple. Numerical relativists use the the techniques developed by numerical analysts to convince themselves (usually for some toy problem) that methods are sound.

Limited computer memory forces evolutions to be computed over a finite region of space. The continuum evolution system can be analyzed and boundary conditions admitting a well behaved initial boundary value problem can be constructed. Special consideration is needed for these boundary conditions to be discretized and implemented in numerical evolutions.

Near a very massive object the gravitational fields can become arbitrarily large. Two major methods have been developed to deal with the black hole boundary. Black Hole excision cuts the very strong field out of the numerical domain. The moving puncture method represents black holes by choosing slices through spacetime that never intersect the singularity. Instead a coordinate singularity (which represents spatial infinity at the other side of a wormhole) must be treated explicitly on the numerical grid.

## 1.2 Asymptotically null slices

Possible sources of gravitational waves are burst sources such as black holes mergers, or periodic sources like spinning neutron stars and binary black hole systems. These systems may be characterized by a central source region and an outer region where the fields are weak and most gravitational radiation is outgoing. There are therefore a broad class of astrophysical situations to simulate: sources which are so far separated from their nearest neighbors that the surrounding spacetime may be approximated accurately as asymptotically flat. Most of the dynamical activity in such a spacetime takes place in the central region, so it makes sense to use more computational power there.

The covariance of General Relativity allows the metric in arbitrary coordinates to be given as initial data for the evolution equations. If these coordinates are chosen naively, coordinate singularities may occur and cause evolutions to blow up after short times. On the other hand it may be possible to choose a foliation

with coordinates adapted to a particular type of problem, which presents vastly favorable error properties even with the same formulation.

Far from the source a coordinate system adapted to outgoing waves is desirable. The work in this thesis is primarily focused on constructing such coordinates, analyzing their properties and using them in numerical evolution.

## 1.3 End-states of evolved gauge conditions

Numerical evolution of binary black holes to merger has been made possible in part by the choice of certain evolved gauge conditions. These gauge conditions admit stationary states (configurations such that the coordinates cease to evolve) which, surprisingly, can be constructed analytically. More surprising still is the fact that numerical evolutions appear to settle at the analytical end-states. The attraction can be studied without the complication of the Einstein constraints by evolving coordinates on top of a known spacetime which rules out constraint violating error from the computation.

Nonlinear hyperbolic PDEs are often susceptible to the formation of shocks; solutions that are initially smooth lose differentiability or even continuity in finite time. Gauge conditions used in numerical relativity are not immune from shock-formation, indeed shocks seem to be a generic feature of their behavior and their formation may prevent a given set of initial data from settling to a time- independent state.

## 1.4 Thesis overview

In Chapter 2 key notions from the theory of PDEs are introduced. In particular the relationship between well-posedness and hyperbolicity is described.

In Chapter 3 the conformal compactifications of the Minkowski and Schwarzschild spacetimes are presented, motivating the formal definition of asymptotic flatness.

In Chapter 4 the $3+1$ decomposition of spacetime is reviewed. The Einstein equations are written as an initial boundary value problem called the ADM formulation. There are many ways of formulating and solving the Einstein equations for numerical implementation, typically these differ by the addition of the constraints to the ADM evolution equations. The Z4, BSSN and NOR formulations are introduced and reduced to spherical symmetry. Finally the Z4 constraint damping scheme [3] is described and extended to the other formulations.

In chapter 5 a one-parameter family of slices adapted to outgoing radiation is constructed. The slices are asymptotically null in the sense that the Lorentz factor between observers in the slices and those in coordinates adapted to asymptotic flatness blows up at large radius. The chapter contains a thorough motivation for and mathematical analysis of the slices. The analysis includes discussion of global structure and the asymptotic growth of the metric and extrinsic curvature on each slice.

In chapter 6 the wave equation is solved in a spherical background. Convergence, the relative size of errors on different slicings and the effects of boundaries are considered on different slices. Chapters 5 and 6 were researched in collaboration with C. Gundlach and G. Calabrese and were written largely by C. Gundlach. They were published as [1].

Chapter 7 introduces the pure-gauge evolution system for evolving coordinates on a fixed background. The evolution system is then used to find gauge conditions suitable for evolving asymptotically null slices in the Minkowski and Schwarzschild spacetimes.

Recent advances in numerical relativity have relied on the use of evolved gauge conditions. These gauge conditions are examined in detail in Chap. 8 pure gauge evolutions are made to investigate the approach to analytical end states. Gauge

shocks are discussed. The work on analytical end states and gauge shocks was performed in collaboration with D Garfinkle and C Gundlach. The sections in which that work is presented were written largely by C Gundlach and appeared as [2]. The effectiveness of the constraint damping scheme introduced in Chap. 4 is demonstrated. Boundary conditions that are either maximally dissipative or constraint preserving are constructed for the spherical NOR and BSSN systems and the first stable evolutions of asymptotically null initial data with the Einstein equations are presented.

All computer simulations were made by code written by the author. Unless otherwise stated the research presented was the work of the author.

Chapter 9 contains conclusions and an outlook for future research, which includes solving the Einstein equations on asymptotically null slices in 3 spatial dimensions.

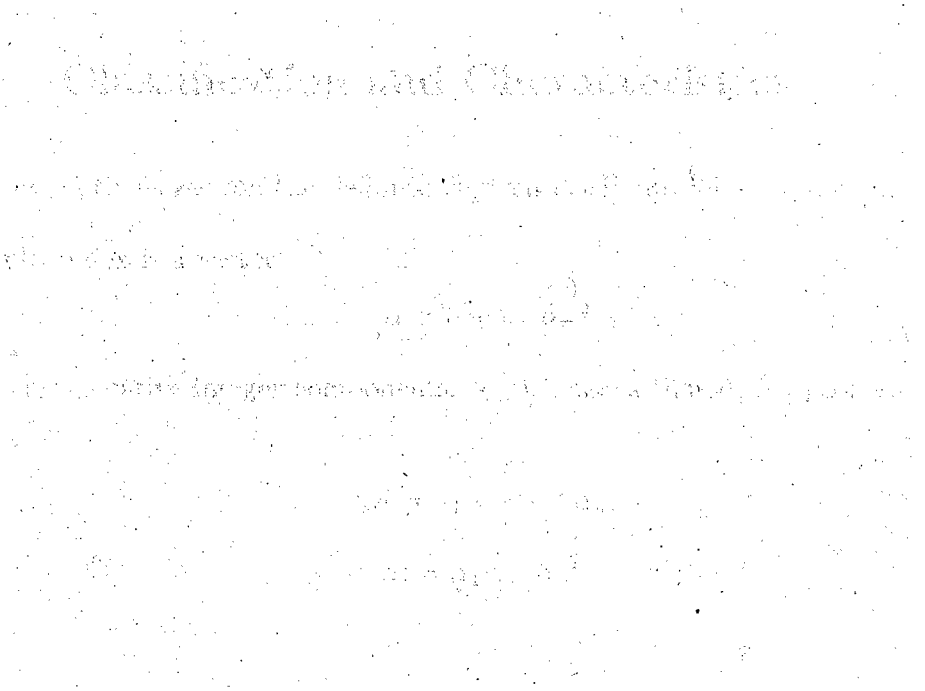

# Chapter 2

# Partial Differential Equations

In this chapter key concepts in the theory of PDEs are reviewed. The notions of hyperbolicity and well-posedness are introduced. Algebraic characterizations for systems of PDEs are described first. The restriction to evolution type equations is then made and further characterizations are given. The definition of well-posedness is given and its relationship with hyperbolicity is detailed. Finally issues related to variable coefficient and nonlinear problems are described.

## 2.1 Classification and Characteristics

Throughout this section the definitions given in [4] and [5] are followed.

A multi-index is a vector

$$\alpha = (\alpha_1, ..., \alpha_n) \tag{2.1}$$

with non-negative integer components. $\alpha \geq \beta$ means that $\alpha_i \geq \beta_i$ for each $i$. Also define

$$|\alpha| = \alpha_1 + \cdots + \alpha_n, \tag{2.2}$$

$$\alpha! = \alpha_1! \ldots \alpha_n!. \tag{2.3}$$

For any vector $\mathbf{x} = (x_1, ..., x_n) \in \mathbf{R}$ define

$$\mathbf{x}^\alpha = x_1^{\alpha_1} ... x_n^{\alpha_n}. \tag{2.4}$$

Denote partial derivatives by

$$\mathcal{D}^\alpha = \frac{\partial^{|\alpha|}}{\partial x_1^{\alpha_1} ... \partial x_1^{\alpha_1}}. \tag{2.5}$$

Consider the linear differential operator

$$L_{ij}(\mathbf{x}, \mathcal{D}) u_j = \sum_{|\alpha| \leq m} (a_\alpha(\mathbf{x}))_{ij} \mathcal{D}^\alpha u_j, \tag{2.6}$$

where $u : \mathbf{R}^k \to \mathbf{R}^k$, and $\mathbf{a}_\alpha(\mathbf{x})$ is a $k \times k$ matrix with components depending on $\mathbf{x}$. The symbol of the operator (partial derivative) $\mathbf{L}(\mathbf{x}, \mathcal{D})$ is defined by

$$L_{ij}(\mathbf{x}, i\boldsymbol{\xi}) := \sum_{|\alpha| \leq m} (a_\alpha(\mathbf{x}))_{ij} (i\boldsymbol{\xi})^\alpha. \tag{2.7}$$

The principal part of the symbol is defined by assigning *weights* $s_i$ and $t_j$ to each equation and dependent variable in such a way that the order of each operator $L_{ij}$ does not exceed $s_i + t_j$; the principal part is then defined to be those terms that have order exactly equal to $s_i + t_j$, i.e

$$L_{ij}^P(\mathbf{x}, i\boldsymbol{\xi}) := \sum_{|\alpha| = s_i + t_j} (a_\alpha(\mathbf{x}))_{ij} (i\boldsymbol{\xi})^\alpha. \tag{2.8}$$

It is assumed that the weights can be assigned in such a way that $\det \mathbf{L}^P$ does not vanish identically cf. [5].

$\phi(\mathbf{x})$ is said to be a characteristic surface of $\mathbf{L}(\mathbf{x}, \mathcal{D})$ if

$$\det \mathbf{L}^P(\mathbf{x}, \nabla\phi) = 0. \tag{2.9}$$

A system is called elliptic at $\mathbf{x}$ if if there are no real characteristics at $\mathbf{x}$, or, equivalently, if

$$\det \mathbf{L}^P(\mathbf{x}, i\boldsymbol{\xi}) \neq 0, \qquad \forall \boldsymbol{\xi} \neq 0. \tag{2.10}$$

An equation is called strictly hyperbolic at $\mathbf{x}$ in the direction $\mathbf{n}$ if

1. $\det \mathbf{L}^P(\mathbf{n}) \neq 0$ and

2. all the roots $\omega$ of the equation

$$\det \mathbf{L}^P(\mathbf{x}, i\boldsymbol{\xi} + i\omega\mathbf{n}) \tag{2.11}$$

are real and distinct for every $\boldsymbol{\xi} \in \mathbf{R}^n$ which is not collinear with $\mathbf{n}$.

The system is called strictly hyperbolic in the direction $\mathbf{n}$ if it is strictly hyperbolic in the direction of $\mathbf{n}$ everywhere. In physical terms $\mathbf{n}$ is considered a timelike direction.

Nonlinear systems are categorized at a given solution according to the type of the linearization of the system at that solution. Characteristic surfaces are similarly defined as the characteristic surfaces of the linearized system. A system is quasilinear if derivatives of principal order occur only linearly (with coefficients which may depend on derivatives of lower order). When considering linear problems with constant coefficients the symbol may be interpreted as the Fourier transform of the operator $\mathbf{L}$.

## 2.2 Evolution Problems

### 2.2.1 Strong and symmetric hyperbolicity

The work that follows will be primarily concerned with a quasilinear systems in an evolution form,

$$u_j = \sum_{|\alpha| \leq m} (a_\alpha(\mathbf{x}, u, D^\beta u))_{ij} D^\alpha u_j \tag{2.12}$$

where $u_j = \frac{\partial}{\partial x^n} u_j$, and $(a_\alpha(\mathbf{x}, u, D^\beta u))_{ij} = 0$ for $\alpha$ with $\alpha_n > 0$. An evolution form PDE has a preferred time-like coordinate $x^n$. If weights are assigned, the system

can be rewritten as

$$\begin{aligned} L_{ij}(\mathbf{x}, u, D^\beta u, D)u_j &= \sum_{|\alpha|=s_i+t_j} (a_\alpha(\mathbf{x}, u, D^\beta u))_{ij} D^\alpha u_j \\ &- \delta_{1(s_j+t_j)}\delta_{ij}\, D^{(0,\ldots,0,1)}u_j \\ &+ \sum_{|\alpha|<s_i+t_j} (a_\alpha(\mathbf{x}, u, D^\beta u))_{ij} D^\alpha u_j = 0 \end{aligned} \tag{2.13}$$

where $|\beta| < |\alpha| = s_i + t_j$ inside the first sum. The principal part of the symbol is therefore

$$\begin{aligned} L^P_{ij}(\mathbf{x}, u, D^\beta u, i\boldsymbol{\xi}) &= \sum_{|\alpha|=s_i+t_j} (a_\alpha(\mathbf{x}, u, D^\beta u))_{ij} (i\boldsymbol{\xi})^\alpha \\ &\quad -\delta_{1(s_j+t_j)}\delta_{ij}\, i\xi_n \end{aligned} \tag{2.14}$$

where again $|\beta| < |\alpha| = s_i + t_j$ inside the first sum. Choose coordinates so that $\mathbf{n} = (0, \ldots, 1)$. The evolution system is called strongly hyperbolic if

1. $\det \mathbf{L}^P(\mathbf{n}) \neq 0$, and

2. The matrix

$$(L^p_{\mathbf{n}}(i\boldsymbol{\xi})))_{ij} = \sum_{|\alpha|=s_i+t_j} (a_\alpha)_{ij} (i\boldsymbol{\xi})^\alpha$$

has purely imaginary eigenvalues, a complete set of eigenvectors and depends smoothly on $\boldsymbol{\xi}$, where $|\boldsymbol{\xi}| = 1$.

Note that $\boldsymbol{\xi}$ here is (as in the definition of strict hyperbolicity) of the form $\boldsymbol{\xi} = (\xi_1, \ldots, \xi_{n-1}, 0)$. This condition is equivalent to the diagonalizability of $\mathbf{L}^p_{\mathbf{n}}(i\boldsymbol{\xi})$ with the similarity (diagonalizing) matrix and inverse similarity matrix depending continuously on $\boldsymbol{\xi}$. Note that for condition 1. to be satisfied $s_i + t_i = 1$ must hold for every $i = 1, \ldots, k$. In other words the *ith* equation may not have more than first derivatives in the *ith* variable. Strong hyperbolicity is also equivalent to the existence of a so-called symmetrizer of the system. This symmetrizer is a matrix $\mathbf{H}(\boldsymbol{\xi})$ with

$$u^\dagger \mathbf{H}(\boldsymbol{\xi}) u > 0. \tag{2.15}$$

with equality if and only if $u = 0$,

$$\mathbf{H}(\boldsymbol{\xi})^\dagger = \mathbf{H}(\boldsymbol{\xi}), \tag{2.16}$$

and

$$(\mathbf{H}(\boldsymbol{\xi})\mathbf{L}_{\mathbf{n}}^p(i\boldsymbol{\xi}))^\dagger + \mathbf{H}(\boldsymbol{\xi})\mathbf{L}_{\mathbf{n}}^p(i\boldsymbol{\xi}) = 0, \tag{2.17}$$

i.e $\mathbf{H}(\boldsymbol{\xi})$ is positive definite, and is hermitian for every $\boldsymbol{\xi}$. The system is called symmetric hyperbolic if the symmetrizer has no dependence on $\boldsymbol{\xi}$.

Now restrict to a particular class of evolution problem: consider a strongly hyperbolic evolution problem as in (2.12) with $m = 2$, and $k = 2$. Such a system will be called $1st$ order in time, $2nd$ order in space, in one spatial dimension. With these restrictions the matrix $\mathbf{L}_{\mathbf{n}}^p$ takes the block form (possibly after relabeling equations and variables)

$$\begin{aligned} \mathbf{L}_{\mathbf{n}}^p &\sim \begin{pmatrix} (i\xi_1)^1 & (i\xi_1)^0 \\ (i\xi_1)^2 & (i\xi_1)^1 \end{pmatrix} \\ &= \begin{pmatrix} (i\xi_1)^0 & 0 \\ 0 & (i\xi_1)^1 \end{pmatrix} \bar{\mathbf{L}}_{\mathbf{n}}^p \begin{pmatrix} (i\xi_1)^1 & 0 \\ 0 & (i\xi_1)^0 \end{pmatrix} \end{aligned} \tag{2.18}$$

Consider solutions $u$ to the equation (where $\simeq$ here means "up to non-principal terms")

$$(i\xi_2)\delta_{ij}u_j \simeq (i\xi_1)(\mathbf{L}_{\mathbf{n}}^p)_{ij}u_j \tag{2.19}$$

which correspond to Fourier transforms of solutions of the original system (assuming linearity, and constant coefficients) up to principle part. Under the definition

$$\bar{u} = \begin{pmatrix} (i\xi_1)^1 & 0 \\ 0 & (i\xi_1)^0 \end{pmatrix} u, \tag{2.20}$$

multiplying (2.19) on the left by

$$\begin{pmatrix} (i\xi_1)^1 & 0 \\ 0 & (i\xi_1)^0 \end{pmatrix}$$

gives

$$i\xi_2\bar{u} = i\xi_1\bar{\mathbf{L}}_{\mathbf{n}}^{p}\bar{u}. \tag{2.21}$$

Clearly $\bar{\mathbf{L}}_{\mathbf{n}}^{p}$ is diagonalizable if and only if $\mathbf{L}_{\mathbf{n}}^{p}$ is. Therefore since the system is strongly hyperbolic, there is a matrix $\mathbf{S}$ with

$$\mathbf{S}^{-1}(\bar{\mathbf{L}}_{\mathbf{n}}^{p})\mathbf{S} = \mathbf{\Lambda} \tag{2.22}$$

diagonal. In the basis $(\hat{u}_i = (\mathbf{S}^{-1})_{ij}\bar{u}_j)$,

$$\delta_{ij}(i\xi_2)\hat{u}_j \simeq (\mathbf{\Lambda})_{ij}(i\xi_1)\hat{u}_j \tag{2.23}$$

the system is diagonalized. Components of $\hat{u}$ are called characteristic variables of the system. Characteristic variables are hence of the form

$$\hat{u}_i = c_1(i\xi_1)u_1 + \cdots + c_l(i\xi_1)u_l + c_{l+1}u_l + \cdots + c_k u_k. \tag{2.24}$$

Under the transformation $(i\xi_1) \rightarrow \frac{\partial}{\partial x_1}$ a linear combination of derivatives of primitive (evolved) variables and derivatives of primitive variables can be associated with the characteristic variable. This construct will also be called a characteristic variable of the system.

### 2.2.2 Matrix notation

This thesis is concerned with quasilinear first order in time second order in space systems given schematically by

$$\dot{u} = a(u)u_x + b(u)v + e(u), \tag{2.25}$$

$$\dot{v} = c(u, u_x, v)u_{xx} + d(u, u_x, v)v_x + f(u, v). \tag{2.26}$$

Where for example $v_x$ denotes the spatial derivative of $v$ in the $x$ direction. so that weights can be assigned $s_u = 0$, $s_v = 1$, $t_u = 1$ and $t_v = 0$. The principal part of the system (equivalent to the principal symbol) can be defined by the matrix equation

$$\begin{pmatrix} u_x \\ v \end{pmatrix} \simeq \begin{pmatrix} a & b \\ c & d \end{pmatrix} \begin{pmatrix} u_x \\ v \end{pmatrix}_x. \tag{2.27}$$

In the work that follows this matrix notation will be adopted.

Weak, strict, strong and symmetric hyperbolicity (defined up to now in terms of the principal symbol) are obviously equivalent to eigenvalue and diagonalizability conditions on the matrix on the right hand side of (2.27).

## 2.3 Well-posedness of the Cauchy Problem

The Cauchy or initial value problem problem for a system of PDEs consists of specifying initial data for all variables on a non-characteristic hypersurface and then finding a solution at later times. A Cauchy problem is well-posed (in the sense of Hadamard) if there exists a unique solution, which depends continuously on the initial data. Without these conditions the problem is called ill-posed. The notion of continuity requires the specification of a norm on the space of solutions. The form of the equations affects the natural choice of norm. Existence and uniqueness are obviously important. The continuity condition may or may not hold for systems of physical interest. However, in the context of numerical relativity, continuity with respect to initial data is a fundamental requirement. Without it, one would have no guarantee that in the limit of infinite resolution, numerical results would converge to an exact solution of the continuum system.

Formally an evolution system (2.12) is called well-posed in a norm $||\cdot||$ if for all initial data there is a unique smooth solution and there are real constants $\alpha$, $K$ independent of the initial data $u(\cdot, 0)$ such that

$$||u(\cdot, t)|| \leq K\, e^{\alpha t}\, ||u(\cdot, 0)||. \tag{2.28}$$

There is a wealth of literature on the first order case; the two key theorems are now described:

**Theorem** 2.2.2, [4] *For an evolution system (2.12) which is linear, has constant coefficients, and is first order in space and time, well-posedness is equivalent to the*

*existence of real constants* $\alpha$, $K$ *such that for every* $\boldsymbol{\xi}$,

$$|e^{\mathbf{L}_{\mathbf{n}}^{P}(i\boldsymbol{\xi})t}| \leq K\, e^{\alpha t}. \tag{2.29}$$

The next theorem illustrates that the well-posedness of first order constant coefficient linear problems may be characterized entirely in terms of strong hyperbolicity.

**Theorem** 2.4.1, [4] *An evolution system (2.12) which is linear, has constant coefficients, and is first order in space and time, is well-posed if and only if it is strongly hyperbolic (without the requirement that the matrix* $L_{\mathbf{n}}^{p}(i\boldsymbol{\xi})$ *depends smoothly on* $\boldsymbol{\xi}$*).*

Variable coefficient problems are considered by making the so called frozen coefficients approximation. Consider the Cauchy problem for the system at every point in space, assuming that the coefficients are fixed to those at the point under consideration. If every such Cauchy problem is strongly hyperbolic (without the smoothness requirement), the localization principle states that the system is well-posed. There is no proof of this statement, so for variable coefficient first order problems the situation is not clear cut. Strong hyperbolicity (with the smooth dependence condition) is sufficient for well-posedness [4], but whether or not this gives a necessary condition is unknown. Quasilinear problems are more complicated still. Analysis here proceeds by linearizing at a given solution, and then making the frozen coefficients approximation to reduce the system to the case of many linear constant coefficient problems.

# Chapter 3

# Asymptotic Flatness

In numerical relativity spacetimes with isolated blackholes or neutron stars are often evolved. Such spacetimes can be characterized by their asymptotic properties "at infinity".

In this chapter asymptotic flatness is defined. Two examples are given to motivate the definition, which by itself is abstract and uninformative. The examples demonstrate that the formal definition does indeed capture the notion intuitively meant by the phrase "asymptotically flat near infinity".

## 3.1 Conformal compactification of Minkowski spacetime

The calculations outlined in this and the following section are standard textbook results [6, 7].

Given the Minkowski metric in standard spherical polar coordinates

$$\mathrm{d}s^2 = -\mathrm{d}T^2 + \mathrm{d}R^2 + R^2 d\Omega^2 \tag{3.1}$$

where $d\Omega^2 \equiv d\theta^2 + \sin^2\theta\, d\varphi^2$; introduce a change of coordinates

$$U \equiv T - R, \quad -\infty < U < \infty, \tag{3.2}$$

$$V \equiv T + R, \quad -\infty < V < \infty, \quad V \geq U. \tag{3.3}$$

In these coordinates the metric becomes

$$\mathrm{d}s^2 = -\mathrm{d}U\mathrm{d}V + \frac{1}{4}(V-U)^2 d\Omega^2 \tag{3.4}$$

These null coordinates are compactified (infinity is brought to a finite coordinate) with a second change of coordinates so that null cones in the new coordinate system are preserved,

$$\hat{u} \equiv \arctan(U), \quad -\tfrac{\pi}{2} < \hat{u} < \tfrac{\pi}{2} \tag{3.5}$$

$$\hat{v} \equiv \arctan(V), \quad -\tfrac{\pi}{2} < \hat{v} < \tfrac{\pi}{2} \tag{3.6}$$

with $\hat{v} \geq \hat{u}$, the metric becomes

$$\mathrm{d}s^2 = \frac{1}{4\cos^2(\hat{u})\cos^2(\hat{v})}(-4\mathrm{d}\hat{u}\mathrm{d}\hat{v} + \sin^2(\hat{v}-\hat{u})d\Omega^2). \tag{3.7}$$

Finally define

$$\Theta^2 \equiv 4\cos^2(\hat{u})\cos^2(\hat{v}) \tag{3.8}$$

and

$$\hat{t} \equiv \hat{v} + \hat{u} \quad -\pi < \hat{t} < \pi \tag{3.9}$$

$$\hat{r} \equiv \hat{v} - \hat{u} \quad 0 \leq \hat{r} < \pi \tag{3.10}$$

with $\hat{r} < \pi - |\hat{t}|$.

With these definitions the line element is

$$\mathrm{d}s^2 = \Theta^{-2}(-\mathrm{d}\hat{t}^2 + \mathrm{d}\hat{r}^2 + \sin^2(\hat{r})^2 d\Omega^2). \tag{3.11}$$

An "unphysical conformal metric" is now defined

$$\mathrm{d}\bar{s}^2 \equiv \Theta^2 \mathrm{d}s^2 = -\mathrm{d}\hat{t}^2 + d\hat{r}^2 + \sin^2(\hat{r})^2 d\Omega^2. \tag{3.12}$$

It is so called because it is by definition related to the physical metric by a conformal transformation.

Whilst Minkowski is inextendible as a spacetime (it is geodesically complete) it is clear that the Minkowski manifold endowed with the unphysical conformal metric can be extended to include the finite boundaries defined as

- $\mathscr{I}^-$ past null infinity $(\hat{t} - \hat{r} = \pi)$
- $\mathscr{I}^+$ future null infinity $(\hat{t} + \hat{r} = \pi)$
- $i^0$ spatial infinity $(\hat{t} = 0, \hat{r} = \pi)$
- $i^-$ past timelike infinity $(\hat{t} = -\pi, \hat{r} = 0)$
- $i^+$ future timelike infinity $(\hat{t} = -\pi, \hat{r} = 0)$

which correspond to some or all of the original coordinates taking infinite values.

In this way infinity has been moved to a finite boundary; hence the spacetime can be analyzed "at infinity". Suppressing the 2 spatial dimensions $\theta$ and $\varphi$, the standard conformal diagram of the Minkowski spacetime can be plotted (see Fig. 3.1). Since metrics related by a conformal factor $\Theta$ as in (3.12) will make the same vector spacelike, timelike and null, it is clear that causal structure is preserved. Asymptotic flatness can now be defined in terms of the causal structure of flat space at infinity.

## 3.2 Conformal compactification of Schwarzschild spacetime

The same procedure is now carried out on the Schwarzschild spacetime. Begin with the metric

$$\mathrm{d}s^2 = -\Big(1 - \frac{2m}{R}\Big)\mathrm{d}T^2 + \Big(1 - \frac{2m}{R}\Big)^{-1}\mathrm{d}R^2 + R^2\mathrm{d}\Omega^2. \tag{3.13}$$

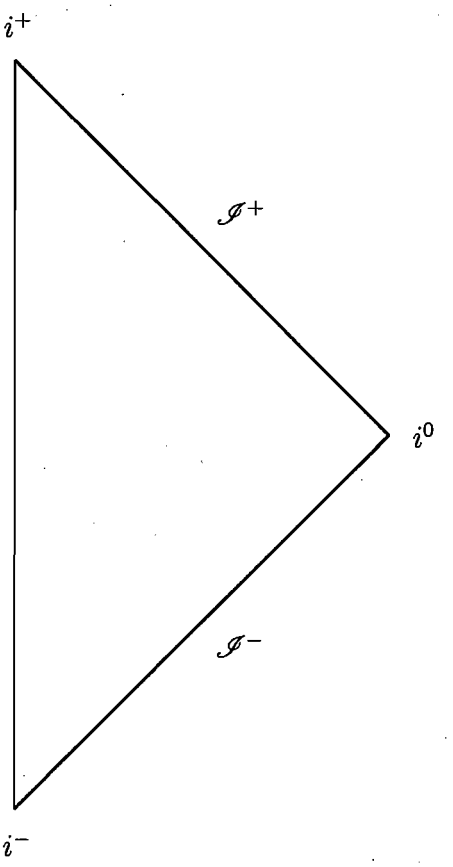


Figure 3.1: The standard conformal diagram of Minkowski spacetime.

The coordinate singularity at $R = 2\mathrm{m}$ suggests changing to a different coordinate scheme before carrying out the conformal compactification. Define advanced and retarded null coordinates $U$ and $V$ by

$$U \equiv T + 2m\log(R-2m) + R \tag{3.14}$$

$$V \equiv T - 2m\log(R-2m) - R. \tag{3.15}$$

Writing the metric in these coordinates,

$$\mathrm{d}s^2 = -\Big(1 - \frac{2m}{R}\Big)\mathrm{d}U\mathrm{d}V + R^2\mathrm{d}\Omega^2 \tag{3.16}$$

Now project into the 2-space $(U, V)$. The induced metric is

$$\mathrm{d}s^2 = -\Big(1 - \frac{2m}{R}\Big)\mathrm{d}U\mathrm{d}V, \tag{3.17}$$

where now, if referring back to the original spacetime it must be noted that every point in the 2-space represents a 2-sphere. Define

$$\bar{U} \equiv \exp\Big(\frac{V}{4m}\Big) \tag{3.18}$$

$$\bar{V} \equiv -\exp\Big(\frac{W}{4m}\Big) \tag{3.19}$$

and the metric takes the form

$$\mathrm{d}s^2 = -\frac{16m^2}{R}\exp\Big(-\frac{R}{2m}\Big)\mathrm{d}\bar{U}\mathrm{d}\bar{V}. \tag{3.20}$$

Define

$$\hat{u} \equiv \arctan\Big(\frac{\bar{U}}{\sqrt{2m}}\Big), \tag{3.21}$$

$$\hat{v} \equiv \arctan\Big(\frac{\bar{V}}{\sqrt{2m}}\Big), \tag{3.22}$$

and then

$$\hat{t} \equiv \hat{u} + \hat{v}, \tag{3.23}$$

$$\hat{r} \equiv \hat{u} - \hat{v}, \tag{3.24}$$

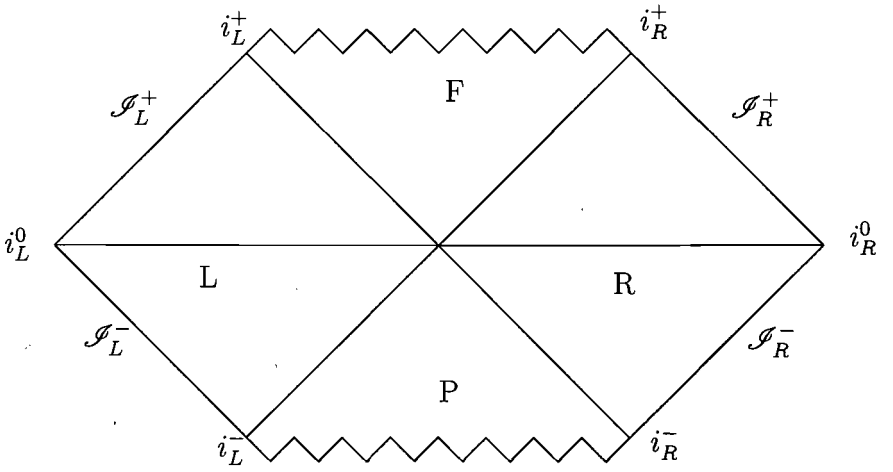


Figure 3.2: The standard conformal diagram of Schwarzschild spacetime.

in terms of which the unphysical metric is

$$\mathrm{d}\hat{s}^2 = -\mathrm{d}\hat{t}^2 + \mathrm{d}\hat{r}^2, \tag{3.25}$$

by taking our conformal factor

$$\Theta^2 = \frac{R}{32m^3}\exp\Big(-\frac{R}{2m}\Big)\cos^2\Big(\frac{\hat{t}+\hat{r}}{2}\Big)\cos^2\Big(\frac{\hat{t}-\hat{r}}{2}\Big)$$

where in these coordinates

$$\tan\Big(\frac{\hat{r}+\hat{t}}{2}\Big)\tan\Big(\frac{\hat{r}-\hat{t}}{2}\Big) = \Big(1-\frac{R}{2m}\Big)\exp\Big(\frac{R}{2m}\Big). \tag{3.26}$$

Considering lines of $R = 0$ and $R = 2m$, and those with $R \to \infty$, the standard conformal diagram of the Schwarzschild spacetime can be constructed as shown in Fig. 3.2.

## 3.3 The formal definition of asymptotic flatness

The formal definition and a brief explanation of asymptotic flatness is now given.

**Definition 1, [8]** A smooth spacetime $(\mathcal{M}, g_{ab})$ is called asymptotically flat if there exists another smooth Lorentz manifold $(\hat{\mathcal{M}}, \hat{g}_{ab})$ such that

1. $\mathcal{M}$ is an open submanifold of $\hat{\mathcal{M}}$ with smooth boundary $\partial\mathcal{M} = \mathscr{I}$,
2. there exists a smooth scalar field $\Theta$ on $\hat{\mathcal{M}}$ such that $\hat{g}_{ab} = \Theta^2 g_{ab}$ on $\mathcal{M}$, and so that $\Theta = 0$, $\mathrm{d}_a\Theta \neq 0$ on $\mathscr{I}$,
3. every null geodesic in $\mathcal{M}$ acquires a future and a past endpoint on $\mathscr{I}$,
4. $R_{ab} = 0$ in a neighborhood of $\mathscr{I}$.

In words the definition may be restated; the physical spacetime may be conformally compactified and a (reasonable) boundary may be appended. If the physical spacetime is close to flat space in a neighborhood of the boundary, then it is called asymptotically flat.

In the work that follows the following property is used; coordinates can be adapted to asymptotic flatness. For example in spherical symmetry, an asymptotically flat spacetime can always be written

$$\mathrm{d}s^2 = g_{TT}\mathrm{d}T^2 + 2g_{TR}\mathrm{d}T\mathrm{d}R + g_{RR}\mathrm{d}R^2 + R^2 d\Omega^2, \tag{3.27}$$

where at large radius the metric components go like $g_{TT} \to 1$, $g_{TR} \to 0$ and $g_{RR} \to 1$. In other words at large radius the spacetime can be written in coordinates that make the line-element look like the Minkowski metric.

# Chapter 4

# The $3+1$ Formalism

A Lorentzian manifold with metric can be decomposed into spacelike hypersurfaces labeled by a time coordinate. A set of equations on the manifold may then be reformulated on these slices as a time evolution problem (possibly with boundaries or constraints), to which numerical solutions may be sought.

Systems of evolution PDEs with constraints may be reformulated by adding those constraints to the evolution equations. Different formulations of the Einstein equations have differing algebraic characterizations; they have varying levels of hyperbolicity.

In this chapter the foliation of spacetime by spacelike hypersurfaces is outlined, the wave equation is presented (required for the numerical experiments in Chapter 6), the ADM form of Einsteins field equations is derived, several strongly hyperbolic extensions of the ADM equations are presented and several coordinate conditions popular in numerical relativity are introduced. Finally the spherical reduction of these systems is presented and constraint damping schemes are described.

## 4.1 Foliations of spacetime

This section follows closely the presentation in [9].

Begin by taking a closed timelike ($g^{ab}\Omega_a\Omega_b < 0$) 1-form $\Omega_a$ on the spacetime $(M, g_{ab})$. $\Omega_a$ is closed

$$\mathrm{d}\Omega_a = \nabla_{[a}\Omega_{b]} = 0, \tag{4.1}$$

so there exists at least locally a scalar function $t$ with the property

$$(\mathrm{d}t)_a = \nabla_a t = \Omega_a. \tag{4.2}$$

This function is used as a local time coordinate. A slice is defined as a surface of constant $t$. At a point $p$ on a slice $\Sigma_t$ we say that vectors $s^a$ such that $\Omega_a s^a = 0$ are in the slice (otherwise $t$ varies in the direction of $s^a$). Observe that $s^a$ is normal to a timelike vector, so must be spacelike ($g^{ab}s_a s_b > 0$). Hence the slice contains only spacelike vectors and is called spacelike.

Since $\Omega_a$ is timelike

$$g^{ab}\Omega_a\Omega_b = -\alpha^{-2} \tag{4.3}$$

for some positive scalar function $\alpha$ on the manifold. The lapse function $\alpha$ relates proper time to coordinate time between neighboring slices.

Define a normalized 1-form associated with the set of slices (foliation) $\{\Sigma\}$ by

$$\omega_a \equiv \alpha\Omega_a, \tag{4.4}$$

satisfying

$$g^{ab}\omega_a\omega_b = -1. \tag{4.5}$$

Vectors in the slice are normal to $\Omega_a$ and therefore to $\omega_a$. In other words $\omega_a$ is normal to the slice. The unit normal vector field to the slice is by definition

$$n^a \equiv -g^{ab}\omega_b \tag{4.6}$$

where the $-$ sign is chosen so that locally $n^a$ points in the direction of increasing $t$. Hence $n_a = -\omega_a = -\alpha\Omega_a$, and $g^{ab}\omega_a n_b = 1$.

The vector $n^a$ may be interpreted as the 4-velocity field of observers instantaneously at rest in the slices $\{\Sigma\}$. They are called Eulerian observers in analogy with fluid mechanics because their motion follows the slices.

The 3-metric $\gamma_{ab}$ induced on the slices by $g_{ab}$ is given by

$$\gamma_{ab} \equiv g_{ab} + n_a n_b \equiv g_{ab} + \omega_a \omega_b. \tag{4.7}$$

A tensor is called spatial if its contraction with $n^a$ on any index vanishes. $\gamma_{ab}$ is spatial, and has contravariant form

$$\gamma^{ab} \equiv g^{ab} + n^a n^b \equiv g^{ab} + \omega^a \omega^b. \tag{4.8}$$

The mixed form of $\gamma_{ab}$ is the operator of projection onto the slices

$$\gamma^a_b \equiv \perp^a_b = \delta^a_b - n^a n_b \tag{4.9}$$

and

$$\perp^a_c \perp^c_b = (\delta^a_c - n^a n_c)(\delta^c_b - n^c n_b) = \perp^a_b \tag{4.10}$$

$$\perp^a_a = 3. \tag{4.11}$$

When the projection operator appears without index it is to be applied to every index of whatever tensor it is acting on. The covariant derivative $D$ induced by $\nabla$ on the slices for a scalar $\psi$ and a spatial vector $v^a$ ($v^a n_a = 0$) is defined by

$$D_a \psi \equiv \perp^b_a \nabla_b \psi \tag{4.12}$$

$$D_a v^b \equiv \perp^b_d \perp^c_a \nabla_c v^d \tag{4.13}$$

with extensions to other derivatives defined similarly. In particular

$$\begin{aligned} D_a \gamma_{bc} &= \perp \nabla_a \gamma_{bc} \\ &= \perp^d_a \perp^e_b \perp^f_c \nabla_d \gamma_{ef} \\ &= 0. \end{aligned} \tag{4.14}$$

Note that $D$ depends only pointwise on $n^a$, hence given a slice, only the metric on that slice is required to determine the induced metric and hence the induced covariant derivative. Other geometric objects can be defined in terms of $D$. The 3-dimensional Riemann tensor $R^d{}_{cba}$, is defined by

$$D_{[a}D_{b]}v_c = \frac{1}{2}R^d{}_{cba}v_d, \tag{4.15}$$

$$R^d{}_{cba}n_d = 0 \tag{4.16}$$

where $v_d$ is spatial. The latter condition makes $R_{abcd}$ spatial.

The extrinsic curvature (second fundamental form) is defined in any one of the equivalent ways

$$K_{ab} \equiv -\perp \nabla_{(a}n_{b)} \tag{4.17}$$

$$\equiv -\frac{1}{2}\mathcal{L}_n\gamma_{ab} \tag{4.18}$$

$$\equiv -\frac{1}{2}\perp \mathcal{L}_n g_{ab}. \tag{4.19}$$

Intuitively $K_{ab}$ may be thought of as the time derivative of the 3-metric $\gamma_{ab}$. The intrinsic geometry of a slice $\Sigma$ is known when given $(\Sigma, \gamma_{ab})$. How this submanifold is embedded in the spacetime $(M, g_{ab})$ is not. For example the Gauss and Codazzi equations indicate that the Riemann tensor on a slice can not be constructed from the projected full four dimensional Riemann tensor $\mathcal{R}_{abcd}$ without the extrinsic curvature,

$$R_{abcd} = \perp \mathcal{R}_{abcd} + K_{ac}K_{bd} - K_{ad}K_{bc}, \tag{4.20}$$

$$\perp \left(\mathcal{R}_{abcd}n^d\right) = D_bK_{ac} - D_aK_{bc}. \tag{4.21}$$

Define

$$a^a \equiv n^b\nabla_b n^a, \tag{4.22}$$

where the acceleration of Eulerian observers $a^a$ is spatial ($a^a n_a = 0$) and satisfies

$$\nabla_a n_b \equiv K_{ab} - n_a a_b, \tag{4.23}$$

$$a_b = D_b \ln \alpha. \tag{4.24}$$

$N^a$ is actually the natural orthogonal vector field that connects slices of the foliation, since

$$1 = g^{ab}(\omega_a)(n_b) = g^{ab}(\Omega_a)(\alpha n_b). \tag{4.25}$$

Note that since

$$\mathcal{L}_n \perp^a_b = 0, \tag{4.26}$$

the time derivative (defined by $\mathcal{L}_t$ so that $\mathcal{L}_t \neq \mathcal{L}_n$) of a spatial tensor is a spatial tensor. Observe that

$$g^{ab}\Omega_a t_b = 1 \tag{4.27}$$

if

$$t^a \equiv \alpha n^a + \beta^a \tag{4.28}$$

where the shift vector $\beta^a$ is spatial, $n^a\beta_a = 0$. With $\beta^a$ chosen $t^a$ is tangent to a family of curves threading slices of $\{\Sigma\}$. Locally these curves are parametrized by $t$ since $\Omega_a = (\mathrm{d}t)_a$ and so

$$t^a(\mathrm{d}t)_a = 1. \tag{4.29}$$

Now consider a coordinate patch labeled by coordinates $(t, x^i)$, then the metric components can be written in terms of the lapse, shift and 3-metric,

$$g_{00} = g_{ab}t^a t^b = -\alpha^2 + \beta^a\beta_a, \tag{4.30}$$

$$g_{0i} = g_{ab}t^a\Big(\frac{\partial}{\partial x^i}\Big)^b = \beta_i, \tag{4.31}$$

$$g_{ij} = \gamma_{ij}. \tag{4.32}$$

The line element becomes

$$\mathrm{d}s^2 = -\alpha^2\mathrm{d}t^2 + \gamma_{ij}(\mathrm{d}x^i + \beta^i\mathrm{d}t)(\mathrm{d}x^j + \beta^j\mathrm{d}t) \tag{4.33}$$

confirming that $\alpha$ describes the proper time along integral curves of $t^a$. Note that spatial tensors have only three components per index.

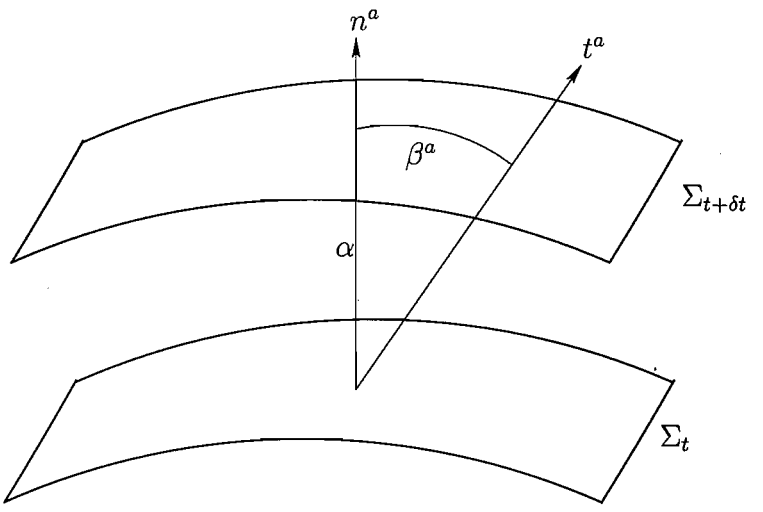


Figure 4.1: Nearby spatial hypersurfaces of a foliation.

## 4.2 The wave equation

The 3+1 split allows equations on spacetime to be solved as initial boundary value problems. Once initial data is prescribed solutions at later times can be found by numerical integration.

The linear, minimally coupled massless scalar wave equation

$$\Box\phi \equiv \nabla_a \nabla^a \phi = 0 \tag{4.34}$$

is often used in the work that follows. It is now decomposed.

Since $\phi$ is a scalar

$$\mathcal{L}_t \phi = \mathcal{L}_\beta \phi + \alpha \mathcal{L}_n \phi = \mathcal{L}_\beta \phi - \alpha \Pi \tag{4.35}$$

where $\Pi \equiv -\mathcal{L}_n \phi = -n^a \nabla_a \phi$. The wave equation can be rewritten as

$$\begin{aligned} 0 &= \nabla_a (g^{ab} \nabla_b \phi) \\ &= D_a (\perp^a_b \nabla^b \phi) - n_a n^b \nabla_b (\perp^a_c \nabla^c \phi) \\ &\quad -K\Pi + \mathcal{L}_n \Pi \\ &= D_a D^a \phi + a^b D_b \phi - K\Pi + \frac{1}{\alpha}(\mathcal{L}_t \Pi - \mathcal{L}_\beta \Pi). \end{aligned} \tag{4.36}$$

Solving for $\mathcal{L}_t\Pi$ gives

$$\mathcal{L}_t\Pi = \mathcal{L}_\beta\Pi - \alpha D_a D^a\phi - \alpha a^b D_b\phi + \alpha K\Pi. \tag{4.37}$$

This second order in space form of the wave equation is chosen as it is similar to popular formalisms of the Einstein equations. The major difference is that the Einstein equations dictate the behavior of geometry, whereas the wave equation describes an additional field on the spacetime.

## 4.3 The ADM decomposition

In this section the derivation of the ADM formulation of the field equations

$$G_{ab} = 8\pi T_{ab} \tag{4.38}$$

is outlined.

Begin by taking the Gauss equation (4.20) and contracting twice with the spatial metric. Rearranging for the Einstein tensor contracted twice with $n^a$ gives the Hamiltonian constraint,

$$G_{ab}n^a n^b = R + K^2 - K_{ij}K^{ij} = 16\pi\rho. \tag{4.39}$$

This is a scalar equation so gives 1 of the 10 Einstein equations.

Taking the Codazzi equation (4.21), contracting once with the spatial metric and rearranging for the projected normal contracted Einstein tensor gives

$$-\perp^i_a G^{ab}n_b = D_j(K^{ij} - \gamma^{ij}K) = j^i \tag{4.40}$$

the momentum constraint, where $j^a \equiv -\perp T^{ab}n_b$. This is a vector equation and so encodes 3 equations. Constraints are a complication that toy problems like the wave equation do not have.

The other 6 equations are given by a coupled evolution system for $\gamma_{ij}$ and $K_{ij}$. To calculate the time derivatives of the spatial metric, take the Lie derivative $\mathcal{L}_t\gamma_{ij}$.

By the definition of the extrinsic curvature

$$\mathcal{L}_t \gamma_{ij} = -2\alpha K_{ij} + \mathcal{L}_\beta \gamma_{ij}. \tag{4.41}$$

For the extrinsic curvature the same procedure must be followed and after some work the final result is

$$\begin{aligned} \mathcal{L}_t K_{ij} &= -D_i D_j \alpha + \alpha[R_{ij} - 2K_{ik}K^k_j + K_{ij}K \\ &\quad -\kappa(S_{ij} - \frac{1}{2}\gamma_{ij}S) - \frac{1}{2}\kappa\rho\gamma_{ij}] + \mathcal{L}_\beta K_{ij}, \end{aligned} \tag{4.42}$$

where $S_{ab} \equiv\perp T_{ab}$ and $S = \gamma^{ab}S_{ab}$.

When closed with a gauge choice (some prescription for the lapse and the shift vector) the ADM formulation is typically only weakly hyperbolic, which means that it does not have a well-posed initial boundary value problem. This motivates the reformulation of the system.

## 4.4 Hyperbolic Reformulation

A common way to rewrite the ADM equations in a strongly hyperbolic form is to add auxiliary variables (with definition constraints) to the set of evolved quantities and add certain combinations of (both physical and definition) constraints to the evolution equations. Examples include the popular Baumgarte-Shapiro-Shibata-Nakamura (BSSN) [10, 11, 12] and the Nagy-Ortiz-Reula (NOR) [13] formulations. BSSN adds another level of complexity by performing a so-called conformal decomposition of the 3-metric and extrinsic curvature, so that the majority of evolved variables become tensor densities.

There are other approaches, notably the Z4 formulation of Bona, Ledvinka and Palenzuela [14, 15, 16] in which a vector of constraints $Z^a$ is added to the full Einstein equations before carrying out the 3+1 split. Z4 is particularly aesthetically pleasing since it maintains the covariance of the Einstein equations, whereas both

BSSN and NOR break the covariance by adding non-covariant auxiliary unknowns to the system.

The relationship between these formulations is fascinating. If the time component of the $Z^a$ vector is set to zero and the spacelike components are replaced with the NOR definition constraint, the NOR system is recovered. If one starts with an appropriate flavor of NOR, there exists a direct relationship between the NOR system and the BSSN system [17].

### 4.4.1 A toy problem

In this section the method for creating strongly hyperbolic evolution systems from ADM-like (weakly hyperbolic) systems with constraints is investigated by means of a toy problem.

Start with a model for the ADM equations; an evolution form equation with a particular structure and a differential constraint $M$. The system is then modified analogously to the way that NOR modifies ADM. The resulting set of equations are strongly hyperbolic.

Consider the linear constant coefficient problem given by

$$\partial_t U = \beta \partial_x U + l.o.t, \tag{4.43}$$

$$\partial_t V = \alpha \partial_{xx} U + \beta \partial_x V + l.o.t, \tag{4.44}$$

($l.o.t$ represents any "lower order terms") with "momentum" constraint

$$M \equiv \partial_x V + l.o.t = 0, \tag{4.45}$$

where in this subsection $\alpha$ and $\beta$ are constant. The principal part is $(U_x, V)_t^T = P(U_x, V)_x^T$, with

$$P = \begin{pmatrix} \beta & 0 \\ \alpha & \beta \end{pmatrix} \tag{4.46}$$

which has the repeated real eigenvalue $\pm\beta$, so the system is at least weakly hyperbolic. It is not strongly hyperbolic; the Jordan decomposition (normal form) [18] of the principal matrix is

$$J = \begin{pmatrix} \beta & 0 \\ 1 & \beta \end{pmatrix} \tag{4.47}$$

with similarity matrix

$$S = \begin{pmatrix} \beta & 0 \\ \alpha & \beta \end{pmatrix}. \tag{4.48}$$

These matrices are defined to satisfy $J = SPS^{-1}$. If a matrix is diagonalizable its Jordan decomposition will be diagonal. This system can not be diagonalized. It can however be expanded as follows; define a new constraint $G$ by

$$G \equiv W - \partial_x U = 0 \tag{4.49}$$

and evolve $W$ along with the other variables. The principal part is then given by

$$\begin{pmatrix} U_x \\ V \\ W \end{pmatrix} = \begin{pmatrix} \beta & 0 & 0 \\ \alpha & \beta & 0 \\ \beta & 0 & 0 \end{pmatrix} \begin{pmatrix} U_x \\ V \\ W \end{pmatrix}_x \tag{4.50}$$

which is still not diagonalizable. If the evolution equations for $V$ and $W$ are replaced (dropping lower order terms) with

$$\partial_t V \simeq \alpha\partial_{xx}U + \beta\partial_x V + \alpha\partial_x G = \beta\partial_x V + \alpha\partial_x W, \tag{4.51}$$

$$\partial_t W \simeq \beta\partial_{xx}U + \beta\partial_x G + \alpha M = \alpha\partial_x V + \beta\partial_x W, \tag{4.52}$$

the principal matrix becomes symmetric,

$$\begin{pmatrix} \beta & 0 & 0 \\ 0 & \beta & \alpha \\ 0 & \alpha & \beta \end{pmatrix} \tag{4.53}$$

so is obviously diagonalizable. It has eigenvalues $\beta \pm \alpha$, $\beta$ and similarity matrix

$$\begin{pmatrix} 1 & 0 & 0 \\ 0 & -1 & 1 \\ 0 & 1 & 1 \end{pmatrix}. \tag{4.54}$$

The example demonstrates that if a weakly hyperbolic system of an ADM-like structure (with constraint) is expanded by introducing auxiliary constraints and carefully adding constraints to the evolution system, then the resulting system can be made strongly hyperbolic. There may be other ways of trying to render the system strongly hyperbolic. The "momentum" constraint could be added to the $\partial_t V$ equation without evolving new variables. These approaches are not canonical and will not be considered further here.

### 4.4.2 Z4

To construct the 4-dimensional covariant Z4 system start with the Einstein equations $G_{ab} = 8\pi T_{ab}$ and replace them with

$$G_{ab} + \nabla_a Z_b + \nabla_b Z_a - g_{ab}\nabla^c Z_c = 8\pi T_{ab}, \tag{4.55}$$

where the vector $Z_a$ is a vector of constraints. Writing $Z^a = X^a + n^a\Theta$ with $\Theta \equiv -n_a Z^a$, gives $\Theta = \alpha Z^0$ and $X_i = Z_i$ in coordinates $t, x_i$. Decomposing the expanded system and relabeling $X_i$ as $Z_i$ gives the evolution equations

$$\begin{aligned}
\dot{\gamma}_{ij} &= \text{ADM}, && (4.56)\\
\dot{K}_{ij} &= \text{ADM} + \alpha\Big(D_i Z_j + D_j Z_i - 2\Theta K_{ij}\Big), && (4.57)\\
\dot{\Theta} &= \mathcal{L}_\beta \Theta + \alpha\Big(\frac{1}{2}H - \Theta K + D_k Z^k - D_k(\ln\alpha)Z^k\Big), && (4.58)\\
\dot{Z}_i &= \mathcal{L}_\beta Z_i + \alpha\Big(M_i + D_i\Theta - D_i(\ln\alpha)\Theta - 2K_i^k Z_k\Big). && (4.59)
\end{aligned}$$

The system has physical constraints $H$, $M_i$ and evolved definition constraints $\Theta$ and $Z_i$.

### 4.4.3 NOR

NOR expands the ADM system (4.39-4.42) with the evolved variable $f_i$ satisfying the definition constraint

$$G_i \equiv f_i - \gamma^{jk}\Big(\gamma_{ij,k} - \frac{\rho}{2}\gamma_{jk,i}\Big). \tag{4.60}$$

The ADM equations are then augmented by coupling with derivatives of the $G_i$ constraint and the Hamiltonian and Momentum constraints as follows,

$$\begin{aligned}
\dot{\gamma}_{ij} &= \text{ADM}, && (4.61)\\
\dot{K}_{ij} &= \text{ADM} + a\alpha G_{(i,j)} + \alpha\gamma_{ij}\left(cH + dG^{,k}_{k}\right), && (4.62)\\
\dot{f}_i &= \partial_t\left(\gamma^{jk}\gamma_{ij,k} - \frac{\rho}{2}\gamma^{jk}\gamma_{jk,i}\right)_{\text{ADM}} + \mathcal{L}_\beta G_i + 2b\alpha M_i. && (4.63)
\end{aligned}$$

The NOR system is strongly (or even symmetric) hyperbolic for a variety of gauge conditions, some of which are discussed below (see Section 4.5). If the covariant derivatives $D$ acting on the $Z_i$ constraints are interpreted as (replaced by) just partial derivatives (breaking the covariance of the full system) NOR can be recovered from the Z4 system under the substitution [3]

$$\Theta \to 0, \quad Z_i \to \frac{1}{2}\Big(f_i - \gamma^{jk}\gamma_{ij,k} + \frac{\rho}{2}\gamma^{jk}\gamma_{jk,i}\Big). \tag{4.64}$$

The first of these conditions need not be enforced. The result is the NOR-$\Theta$ system (up to lower order constraint addition and interpretation of covariant derivatives on constraint variables as partial derivatives only). To get the Hamiltonian and constraint divergence additions in (4.62) the change of dependent variable

$$K_{ij} \to K_{ij} + c\gamma_{ij}\Theta \tag{4.65}$$

(and the restriction $c = d$ is made) must be taken before the $\Theta \to 0$ condition is imposed.

### 4.4.4 BSSN

The BSSN formulation is usually presented as the conformal decomposition of the ADM equations (4.39-4.42) with several substitutions from definition and physical constraints. In the following exposition constraint addition and conformal decomposition are explicitly separated; the BSSN system is the conformal decomposition of a special case of NOR.

**Definition constraint** As in NOR the definition constraint

$$G_i \equiv f_i - \gamma^{jk}\left(\gamma_{ij,k} - \frac{\rho}{2}\gamma_{jk,i}\right) \tag{4.66}$$

is taken, but now $\rho = 2/3$ is fixed. Below it will be seen that this choice of $\rho$ naturally makes $f_i$ coincide with the relevant BSSN variable.

**Constraint addition** The ADM equations are adjusted to

$$\dot{\gamma}_{ij} = \text{ADM}, \tag{4.67}$$

$$\dot{K}_{ij} = \text{ADM} + \alpha G_{(i,j)} - \frac{1}{3}\alpha\gamma_{ij}\left(H + G^k_k\right), \tag{4.68}$$

$$\dot{f}_i = \partial_t\left(\gamma^{jk}\gamma_{ij,k} - \frac{\rho}{2}\gamma^{jk}\gamma_{jk,i}\right)_{\text{ADM}} + 2\alpha M_i + \beta^j G_{i,j} + \frac{1}{\gamma}\beta^j \log(\gamma)_{,j} G_i + \beta^j\gamma_{il}(\gamma^{\frac{1}{3}}\gamma^{lm}_{,j})G_m. \tag{4.69}$$

Note that the highest (principal) derivatives of variables added correspond exactly to those added in the NOR formulation (with $a = b = 1$, $c = d = -1/3$). It is for this reason that Gundlach and Martín-García [17] were able to identify the two systems when analyzing only the principal part.

**Conformal variables and algebraic constraints** The BSSN system takes as its evolved variables

$$\bar{\gamma}_{ij} = e^{-4\phi}\gamma_{ij}, \qquad \phi = \frac{1}{12}\ln(\det\gamma), \tag{4.70}$$

$$K = \gamma^{ij}K_{ij}, \qquad \bar{A}_{ij} = e^{-4\phi}(K_{ij} - \gamma_{ij}K/3), \tag{4.71}$$

$$\bar{\Gamma}^i = \bar{\gamma}^{jk}\bar{\Gamma}^i_{jk} = -\bar{\gamma}^{ij}_{,j}. \tag{4.72}$$

Now note that with $\rho = 2/3$ in the definition of $G_i$

$$G_i = f_i - \gamma^{jk}\Big(\gamma_{ij,k} - \frac{\rho}{2}\gamma_{jk,i}\Big) = \bar{\gamma}_{ij}\bar{\Gamma}^j - \bar{\gamma}^{jk}\bar{\gamma}_{ij,k}. \tag{4.73}$$

**Evolution equations and constraints** Taking a time derivative of the definitions, substituting the evolution equations and rewriting in terms of the evolved variables gives (up to the algebraic constraints $D = \ln(\det\bar{\gamma})$, $T = \bar{\gamma}^{ij}\bar{A}_{ij}$, which are assumed satisfied exactly) the standard BSSN equations. The unknowns evolve according to

$$\dot{\bar{\gamma}}_{ij} = -2\alpha\bar{A}_{ij} + \beta^k\bar{\gamma}_{ij,k} + \bar{\gamma}_{ik}\beta^k_{,j} - \frac{2}{3}\bar{\gamma}_{ij}\beta^k_{,k}, \tag{4.74}$$

$$\dot{\phi} = -\frac{1}{6}\alpha K + \beta^k\phi_{,k} + \frac{1}{6}\beta^k_{,k}, \tag{4.75}$$

$$\begin{aligned}\dot{\bar{A}}_{ij} &= e^{-4\phi}[-D_iD_j\alpha + \alpha R_{ij}]^{\mathrm{TF}} + \alpha(K\bar{A}_{ij} - 2\bar{A}_{ik}\bar{A}^k_j) \\ &\quad +\beta^k\bar{A}_{ij,k} + \bar{A}_{ik}\beta^k_{,j} - \frac{2}{3}\bar{A}_{ij}\beta^k_{,k},\end{aligned} \tag{4.76}$$

$$\dot{K} = -D_iD^i\alpha + \alpha(\bar{A}_{ij}\bar{A}^{ij} + \frac{1}{3}K^2) + \beta^iK_{,i}, \tag{4.77}$$

$$\begin{aligned}\dot{\bar{\Gamma}}^i &= -2\bar{A}^{ij}\alpha_{,j} + 2\alpha(\bar{\Gamma}^i_{jk}\bar{A}^{jk} + 8\bar{A}^ij\phi_{,j} - \frac{2}{3}\bar{\gamma}^{ij}K_{,j}) \\ &\quad \bar{\gamma}^{jk}\beta^i_{,jk} + \frac{1}{3}\bar{\gamma}^{ij}\beta^k_{,kj} + \beta^j\bar{\Gamma}^i_{,j} - (\bar{\Gamma})^j_{\mathrm{DEF}}\beta^i_{,j} + \frac{2}{3}(\bar{\Gamma})^i_{\mathrm{DEF}}\beta^j_{,j},\end{aligned} \tag{4.78}$$

where $[\,]^{\mathrm{TF}}$ denotes the trace free part, $(\,)_{\mathrm{DEF}}$ denotes the definition of those terms rather than the evolved variable and $R_{ij}$ is partially rewritten in terms of $\bar{\Gamma}^i$,

$$R_{ij} = R^\phi_{ij} + \bar{R}_{ij}, \tag{4.79}$$

$$R^\phi_{ij} = -2\bar{D}_i\bar{D}_j\phi - 2\bar{\gamma}_{ij}\bar{D}^k\bar{D}_k\phi + 4\bar{D}_i\phi\bar{D}_j\phi - 4\bar{\gamma}_{ij}\bar{D}^k\phi\bar{D}_k\phi, \tag{4.80}$$

$$\begin{aligned}\bar{R}_{ij} &= -\frac{1}{2}\bar{\gamma}^{lm}\bar{\gamma}_{ij,lm} + \bar{\gamma}_{k(i|}\bar{\Gamma}^k_{|,j)} + (\bar{\Gamma})^k_{\mathrm{DEF}}\bar{\Gamma}_{(ij)k} + \\ &\quad \bar{\gamma}^{lm}\left(2\bar{\Gamma}^k_{l(i}\bar{\Gamma}_{j)km} + \bar{\Gamma}^k_{im}\bar{\Gamma}_{klj}\right).\end{aligned} \tag{4.81}$$

$\bar{D}_i$ denotes the covariant derivative compatible with the conformal metric. The physical constraints are rewritten

$$H = R + \frac{2}{3}K^2 - \bar{A}_{ij}\bar{A}^{ij}, \tag{4.82}$$

$$\bar{M}^i = \bar{A}^{ij}_{,j} + \bar{\Gamma}^i_{jk}\bar{A}^{jk} + 6\bar{A}^{ij}\phi_{,j} - \frac{2}{3}\bar{\gamma}^{ij}K_{,j}, \tag{4.83}$$

where $\bar{M}^i$ denotes $M_i$ with the index raised by the conformal metric. The definition constraints are given by

$$G_i = \bar{\Gamma}^i - \bar{\gamma}^{jk}\bar{\Gamma}^i_{jk}, \tag{4.84}$$

and algebraic constraints by

$$D \equiv \ln(\det\bar{\gamma}) = 0, \qquad T \equiv \bar{\gamma}^{ij}\bar{A}_{ij} = 0. \tag{4.85}$$

Numerical relativity codes use a technique called constraint projection to enforce the algebraic constraints. When operations are performed which may violate the $D$ and $T$ constraints they are enforced explicitly. It is for this reason that we need not worry about the addition of $D$ or $T$ constraints in the construction of (4.74-4.78); the continuum system they represent is identical to that of (4.67-4.69).

If non-principal terms are appropriately added to the Z4 system before the restriction (4.64) and the choice $\rho = 2/3$, $a = b = 1$, $c = d = -1/3$ is made BSSN can be retrieved. The system obtained if the $\Theta \to 0$ condition is not imposed will be called BSSN-$\Theta$.

Hopefully separating the two aspects of the BSSN system will help to clarify its relationship with other formulations. Studying numerically the behavior of the constraint adjusted versus the conformally decomposed system may be of interest when trying to understand what exactly it is about the BSSN system that has lead to its success.

## 4.5 Gauge conditions

In the previous section the Einstein equations were reduced to an evolution PDE problem with constraints. To do this the spacetime was foliated by spacelike slices. The choice of slice is of crucial importance and is equivalent to a choice of lapse $\alpha$ and shift $\beta^j$.

It is essential that coordinates are chosen so that unphysical coordinate singularities do not form as in the case of geodesic slicing in which the lapse is fixed $\alpha = 1$, and the shift vanishes [10].

Broadly speaking, one may characterize gauge conditions as either fixed, algebraic or differential (evolved or elliptic) [19].

**Fixed gauge conditions** Fixed gauge conditions prescribe the lapse and shift a priori as functions which depend on only local coordinates. Such gauges typically give rise to an ill-posed initial value problem for the Einstein equations [19]. They are not discussed further here.

**Algebraic gauge conditions** Algebraic gauge conditions are those which construct a lapse and shift vector as a function of the metric and extrinsic curvature, or other auxiliary evolved variables. A key example of an algebraic gauge condition is a densitized lapse

$$\alpha = \gamma^{\sigma} Q(t, x^i) \tag{4.86}$$

where $Q$ is some given function. When either the NOR or BSSN systems are closed with densitized lapse and fixed shift the resulting system is strongly hyperbolic [13]. The only algebraic condition for the shift to be considered in this thesis is the so-called area locking shift condition [20]. In spherical symmetry the ADM equations for the radial component of the metric $\gamma_{\theta\theta} \equiv \gamma_T r^2$, becomes (see sect. 4.6),

$$\dot{\gamma}_T = -2\alpha K_T + \beta\Big(\gamma_{T,r} + \frac{2\gamma_T}{r}\Big). \tag{4.87}$$

The condition $\dot{\gamma}_T = 0$ can be imposed by choosing the shift appropriately, fixing radial coordinates

$$\beta = 2\alpha K_T \Big(\gamma_{T,r} + \frac{2\gamma_T}{r}\Big)^{-1}. \tag{4.88}$$

**Evolved gauge conditions** Recent progress in the evolution of binary black holes has relied on (amongst other things) the use of so-called evolved gauge conditions, in which the lapse and shift are promoted to the status of evolved variable. Many live gauge conditions have been used, some on a trial and error basis and some conceived through geometric intuition. The symmetry-seeking behavior (tendency to become Killing) and end states associated with the following gauge conditions are discussed in Chap. 8.

The following conditions are (confusingly) all called Bona-Massó slicing conditions [21, 46, 22] (hereafter BM):

$$\alpha\, n^a \nabla_a \alpha \equiv \dot{\alpha} - \beta^i \alpha_{,i} = -\mu_L \alpha^2 K, \tag{4.89}$$

$$\dot{\alpha} = -\mu_L \alpha^2 (K - K_0), \tag{4.90}$$

$$\dot{\alpha} = -\mu_L \alpha \left(\alpha K - D_i \beta^i\right), \tag{4.91}$$

where $\mu_L$ is a given function of $\alpha$ and $K_0(x^i)$ is the initial value of $K$. For clarity, (4.89) will be referred to as "BMn" (the derivative is along the slice normals) and to (4.90) as "BMt" (the derivative is along the time lines). The third condition will be called "BMg", as it can be integrated for any $\mu_L = \mu_L(\alpha)$ to relate $\alpha$ to the 3-metric determinant. For $\mu_L = 2/\alpha$, BMg integrates to $\alpha = f(x) + \ln|\det \gamma_{ij}|$, explaining the name "1+log slicing". BMn and BMt can be integrated only if the shift is zero.

Recent numerical successes have, in particular relied on the BMn lapse condition (4.89).

As $n^a$ is a true vector and $\alpha$ and $K$ are scalars under a change of coordinates $x^i$ on the slice, this slicing condition is independent of the coordinates on the slice and

therefore independent of the shift. The geometric specification of BMt and BMg (but not BMn) slicing depends on the shift.

The most common live shift condition is the so-called gamma driver shift, so called because it was first used with the BSSN system to control the behavior of the evolved auxiliary variable $\bar{\Gamma}^i$. Like the Bona-Massó slicing conditions, gamma-driver shift comes in different types,

$$\dot{\beta}^i = \alpha^2 \mu_S B^i + \beta^j \beta^i_{,j}, \qquad \dot{B}^i = \alpha^2 \mu_S \bar{\Gamma}^i + \beta^j B^i_{,j} - \eta \beta^i, \tag{4.92}$$

$$\dot{\beta}^i = \alpha^2 \mu_S B^i, \qquad \dot{B}^i = \alpha^2 \mu_S \bar{\Gamma}^i - \eta \beta^i, \tag{4.93}$$

where $\mu_S$ is a function of $\alpha$. Other flavors of NOR can be supplemented with $f_i$-driver shift. If $\mu_S = 1/\alpha^2$ is taken then gamma-driver shift can be integrated to give [17],

$$\dot{\beta}^i = \bar{\Gamma}^i - \eta \beta^i + \beta^j \beta^i_{,j}, \tag{4.94}$$

$$\dot{\beta}^i = \bar{\Gamma}^i - \eta \beta^i, \tag{4.95}$$

the form most commonly used in the work that follows, which will be referred to in general as $f_i$-$n$ driver shift and $f_i$-$t$ driver shift respectively.

## 4.6 Spherical reduction

In this thesis several spherical reductions of the Einstein equations will be evolved numerically.

Very generally symmetry can be exploited to reduce the dimensionality of a problem. For numerical simulation the advantages of such an approach are obvious; holding less data in memory means less computation, so results can be harvested quickly. Of course the range of physically interesting spherically symmetric problems is limited, but in the work that follows the focus will be on proof of principle experiments and calculations.

In the next section the spherical ansatz and reduction method is described. Afterwards the spherical reduction of Z4, NOR and BSSN are given.

### 4.6.1 Reduction method

A spherical reduction of Z4 is straightforward because the evolved variables all transform as tensors. BSSN and NOR are trickier. If one were to naively write down the evolution system for BSSN or NOR the resulting equations would of course be a spherical reduction of General Relativity, but would not faithfully represent a spherical reduction of the three dimensional Cartesian systems commonly evolved in modern numerical relativity codes. To compute a faithful spherical reduction of those three dimensional systems additional structure has to be placed on the spacetime. Non-tensorial variables must be redefined covariantly. The method can be outlined in the following way;

**Spherical ansatz** Make the spherical ansatz for the metric and other tensors, so that they may be written like

$$\mathrm{d}s^2 = \gamma_{rr}\mathrm{d}r^2 + \gamma_T r^2(\mathrm{d}\theta^2 + \sin^2\theta\mathrm{d}\phi^2). \tag{4.96}$$

**Auxiliary connection** Define an auxiliary connection [23] which is zero by definition in cartesian coordinates. This connection induces a covariant derivative equal to partial derivatives in cartesian coordinates. Use the new covariant derivative to define any auxiliary variables. Transform the (now tensorially defined) auxiliary variables into spherical coordinates. Interpret all partially differentiated constraint addition terms as constraints acted on by the new covariant derivative. Re-defining the vector auxiliary variable of the NOR and BSSN formulations should have made them easier to use with non-Cartesian coordinates or multiple coordinate patches. (*Optional for conformal decomposition*) Treat the cartesian tensor densities as tensors which are equal to the conformal variables naturally defined in cartesian co-

ordinates. For example the BSSN $\phi$ variable becomes

$$\phi = \frac{1}{12} \ln \left( \frac{\det \gamma}{r^4 \sin^2 \theta} \right) \tag{4.97}$$

rather than (4.70).

**Lie derivatives** (*Optional for conformal decomposition*) Non-tensor variables do not have a well-defined Lie derivative. Take the convention for the cartesian expression and transform to spherical coordinates assuming that the derivatives in the cartesian expression are given by the auxiliary covariant derivative.

**Add enforced constraints to evolution equations** (*Optional for conformal decomposition*) If a given constraint is to be enforced at every time during numerical evolution, it may be added to the evolution equations without affecting the continuum system whatsoever. Such constraints are added to the system so that the equations become as close as possible to those in the literature.

**Regularity conditions** If the origin $r = 0$ is to be included in the domain of evolution regularity conditions must be imposed. Metric coefficients, extrinsic curvature components and the lapse must be even. The shift must be odd. Additionally local flatness requires that the metric satisfies $\gamma_{rr} - \gamma_T = O(r^2)$ (similarly for the extrinsic curvature).

### 4.6.2 Z4

The spherical Z4 evolution equations are given by

$$\dot{\gamma}_{rr} = -2\alpha K_{rr} + \beta\gamma_{rr} + 2\gamma_{rr}\beta_{,r}, \tag{4.98}$$

$$\dot{\gamma}_T = -2\alpha K_T + \beta\Big(\gamma_{T,r} + \frac{2\gamma_T}{r}\Big), \tag{4.99}$$

$$\begin{aligned}\dot{K}_{rr} = {} & \beta K_{rr,r} + K_{rr}\beta_{,r} - \alpha_{,rr} + \frac{\gamma_{rr,r}}{2\gamma_{rr}}\alpha_{,r} \\ & +\alpha\Bigg( - \frac{K_{rr}^2}{\gamma_{rr}} + 2\frac{K_{rr}K_T}{\gamma_T} - 2K_{rr}\Theta - \frac{\gamma_{T,rr}}{\gamma_T} + \frac{\gamma_{rr,r}\gamma_{T,r}}{2\gamma_{rr}\gamma_T} + \frac{\gamma_{T,r}^2}{2\gamma_T^2} \\ & -2Z_{r,r} - \frac{\gamma_{rr,r}}{\gamma_{rr}}Z_r + \frac{1}{r}\Big(\frac{\gamma_{rr,r}}{\gamma_{rr}} - 2\frac{\gamma_{T,r}}{\gamma_T}\Big)\Bigg),\end{aligned} \tag{4.100}$$

$$\begin{aligned}\dot{K}_T = {} & \beta\Big(K_{T,r} + 2\frac{K_T}{r}\Big) - \Big(\gamma_{T,r} + \frac{2\gamma_T}{r}\Big)\frac{\alpha_{,r}}{2\gamma_{rr}} \\ & +\alpha\Bigg(\frac{K_{rr}K_T}{\gamma_{rr}} - 2K_T\Theta - \frac{\gamma_{T,rr}}{2\gamma_{rr}} + \frac{\gamma_{rr,r}\gamma_{T,r}}{4\gamma_{rr}^2} + \Big(\frac{\gamma_{T,r}}{\gamma_T} + 2\frac{\gamma_T}{r\gamma_{rr}}\Big)Z_r \\ & +\frac{1}{r}\Big(\frac{\gamma_T}{2\gamma_{rr}^2}\gamma_{rr,r} - 2\frac{\gamma_{T,r}}{\gamma_{rr}}\Big) + \frac{1}{r^2}\Big(1 - \frac{\gamma_T}{\gamma_{rr}}\Big)\Bigg),\end{aligned} \tag{4.101}$$

$$\begin{aligned}\dot{\Theta} = {} & \beta\Theta_{,r} - \frac{Z_r}{\gamma_{rr}}\alpha_{,r} + \alpha\Bigg(\frac{K_{rr}K_T}{\gamma_{rr}\gamma_T} + \frac{K_T^2}{2\gamma_T^2} - \Big(\frac{K_{rr}}{\gamma_{rr}} + \frac{K_T}{\gamma_T}\Big)\Theta \\ & +\frac{\gamma_{rr,r}\gamma_{T,r}}{4\gamma_{rr}^2\gamma_T} + \frac{\gamma_{T,r}^2}{8\gamma_{rr}\gamma_T^2} - \frac{\gamma_{T,rr}}{2\gamma_{rr}\gamma_T} + \frac{Z_{r,r}}{\gamma_{rr}} + \Big(\frac{\gamma_{T,r}}{\gamma_T} - \frac{\gamma_{rr,r}}{\gamma_{rr}} + \frac{2}{r}\Big)\frac{Z_r}{\gamma_{rr}} \\ & +\frac{1}{2r\gamma_{rr}}\Big(\frac{\gamma_{rr,r}}{\gamma_{rr}} - 3\frac{\gamma_{T,r}}{\gamma_T}\Big) + \frac{1}{2r^2}\Big(\frac{1}{\gamma_T} - \frac{1}{\gamma_{rr}}\Big)\Bigg),\end{aligned} \tag{4.102}$$

$$\begin{aligned}\dot{Z}_r = {} & \beta Z_{r,r} + Z_r\beta_{,r} - \Theta\alpha_{,r} \\ & +\alpha\Bigg(\Big(\frac{K_{rr}}{\gamma_{rr}} + \frac{K_T}{\gamma_T}\Big)\frac{\gamma_{T,r}}{\gamma_T} - 2\frac{K_{T,r}}{\gamma_T} - 2\frac{K_{rr}}{\gamma_{rr}}Z_r + \Theta_{,r} \\ & +\frac{2}{r}\Big(\frac{K_{rr}}{\gamma_{rr}} - \frac{K_T}{\gamma_T}\Big)\Bigg).\end{aligned} \tag{4.103}$$

The system has physical constraints

$$H \equiv -2\frac{\gamma_{T,rr}}{\gamma_{rr}\gamma_T} + 2\frac{K_{rr}K_T}{\gamma_{rr}\gamma_T} + \frac{K_T^2}{\gamma_T^2}\frac{\gamma_{rr,r}\gamma_{T,r}}{2\gamma_{rr}^2\gamma_T} + \frac{\gamma_T^2}{4\gamma_{rr}\gamma_T^2} + \frac{1}{r\gamma_{rr}}\Big(\frac{\gamma_{rr,r}}{\gamma_{rr}} - 3\frac{\gamma_{T,r}}{\gamma_T}\Big) + \frac{1}{r^2}\Big(\frac{1}{\gamma_T} - \frac{1}{\gamma_{rr}}\Big) = 0, \tag{4.104}$$

$$M_r \equiv \Big(\frac{K_{rr}}{\gamma_{rr}\gamma_T} + \frac{K_T}{\gamma_T^2}\Big)\gamma_{T,r} - 2\frac{K_{T,r}}{\gamma_T} + \frac{2}{r}\Big(\frac{K_{rr}}{\gamma_{rr}\gamma_T} + \frac{K_T}{\gamma_T^2}\Big) = 0, \tag{4.105}$$

and definition constraints $\Theta$ and $Z_r$.

### 4.6.3 NOR

Taking $a = b = 1$, $c = d = 0$ (NOR-A in the terminology of [17]) the spherical NOR evolution equations are given by

$$\dot{\gamma}_{rr} = -2\alpha K_{rr} + \beta\gamma_{rr} + 2\gamma_{rr}\beta_{,r}, \tag{4.106}$$

$$\dot{\gamma}_T = -2\alpha K_T + \beta\Big(\gamma_{T,r} + \frac{2\gamma_T}{r}\Big), \tag{4.107}$$

$$\begin{aligned}\dot{K}_{rr} = {} & \beta K_{rr,r} + 2K_{rr}\beta_{,r} - \alpha_{,rr} + \frac{\gamma_{rr,r}}{2\gamma_{rr}}\alpha_{,r} \\ & +\alpha\Bigg(\frac{\rho-2}{2\gamma_{rr}}\gamma_{rr,rr} + \frac{\rho-1}{\gamma_T}\gamma_{T,rr} - \frac{\rho-2}{2\gamma_{rr}^2}\gamma_{rr,r}^2 + \frac{1-2\rho}{\gamma_T^2}\gamma_{T,r}^2 \frac{\gamma_{rr,r}\gamma_{T,r}}{2\gamma_{rr}\gamma_T} \\ & +\frac{2}{r^2}\Big(\frac{\gamma_{rr}}{\gamma_T} - 1\Big) + \frac{1}{r}\Big(\frac{1}{\gamma_{rr}} - \frac{2}{\gamma_T}\Big)\gamma_{rr,r} + \frac{2}{r\gamma_T}\Big(\frac{\gamma_{rr}}{\gamma_T} - 1\Big)\gamma_{T,r} + f_{r,r} \\ & +\frac{2K_{rr}^2}{\gamma_{rr}^2} + 2\frac{K_{rr}K_T}{\gamma_T}\Bigg),\end{aligned} \tag{4.108}$$

$$\begin{aligned}\dot{K}_T = {} & \beta\Big(K_{T,r} + 2\frac{K_T}{r}\Big) - \Big(\frac{\gamma_{T,r}}{2\gamma_{rr}} + \frac{\gamma_T}{r\gamma_{rr}}\Big)\alpha_{,r} \\ & +\alpha\Bigg(-\frac{\gamma_{T,rr}}{2\gamma_{rr}} + \frac{\gamma_{rr,r}\gamma_{T,r}}{4\gamma_{rr}^2} + \frac{1}{2r\gamma_{rr}}\Big(\rho - 2 + \frac{\gamma_T}{\gamma_{rr}}\Big)\gamma_{rr,r} + \frac{1}{r}\Big(\frac{\rho}{\gamma_T} - \\ & \frac{2}{\gamma_{rr}}\Big)\gamma_{T,r} + \frac{1}{r^2}\Big(3 - 2\frac{\gamma_{rr}}{\gamma_T} - \frac{\gamma_T}{\gamma rr}\Big)\frac{f_r}{r} + \frac{K_{rr}K_T}{\gamma_{rr}}\Bigg)\end{aligned} \tag{4.109}$$

$$\begin{aligned}\dot{f}_r = {} & \beta f_{r,r} + \frac{2}{r^2}\beta\Big(\rho - 1 - \frac{\gamma_{rr}}{\gamma_T}\Big) + f_r\beta_{,r} + (\rho-2)\beta_{,rr} - \frac{2}{r}\beta_{,r}\Big(\rho - 1 \\ & -\frac{\gamma_{rr}}{\gamma_T}\Big) + \alpha\Bigg(\frac{\rho-2}{\gamma_{rr}}K_{rr,r} + 2\frac{\rho-2}{\gamma_T}K_{T,r} + \frac{4}{r}\Big(\frac{1}{\gamma_{rr}} - \frac{1}{\gamma_T}\Big)K_{rr} + \frac{4}{r}\Big(\frac{1}{\gamma_T} \\ & -\frac{1}{\gamma_{rr}}\Big)\frac{\gamma_{rr}}{\gamma_T}K_T - (\rho-2)\frac{K_{rr}}{\gamma_{rr}^2}\gamma_{rr,r} + 2\Big(\frac{K_{rr}}{\gamma_{rr}\gamma_T} - (\rho-1)\frac{K_T}{\gamma_T^2}\Big)\gamma_{T,r}\Bigg) + \\ & \Big((\rho-2)\frac{K_{rr}}{\gamma_{rr}} + 2\rho\frac{K_T}{\gamma_T}\Big)\alpha_{,r}.\end{aligned} \tag{4.110}$$

The system has constraints

$$H \equiv -2\frac{\gamma_{T,rr}}{\gamma_{rr}\gamma_T} + 2\frac{K_{rr}K_T}{\gamma_{rr}\gamma_T} + \frac{K_T^2}{\gamma_T^2}\frac{\gamma_{rr,r}\gamma_{T,r}}{2\gamma_{rr}^2\gamma_T} + \frac{\gamma_T^2}{4\gamma_{rr}\gamma_T^2} + \frac{1}{r\gamma_{rr}}\Big(\frac{\gamma_{rr,r}}{\gamma_{rr}} - 3\frac{\gamma_{T,r}}{\gamma_T}\Big) + \frac{1}{r^2}\Big(\frac{1}{\gamma_T} - \frac{1}{\gamma_{rr}}\Big) = 0, \tag{4.111}$$

$$M_r \equiv \Big(\frac{K_{rr}}{\gamma_{rr}\gamma_T} + \frac{K_T}{\gamma_T^2}\Big)\gamma_{T,r} - 2\frac{K_{T,r}}{\gamma_T} + \frac{2}{r}\Big(\frac{K_{rr}}{\gamma_{rr}\gamma_T} + \frac{K_T}{\gamma_T^2}\Big) = 0, \tag{4.112}$$

$$G_r \equiv f_r + (\rho - 2)\frac{\gamma_{rr,r}}{2\gamma_{rr}} + \rho\frac{\gamma_{T,r}}{\gamma_T} + \frac{2}{r}\Big(1 - \frac{\gamma_{rr}}{\gamma_T}\Big) = 0. \tag{4.113}$$

### 4.6.4 BSSN

Assuming that the $D$ and $T$ constraints are to be enforced there is an ambiguity in defining any quantity in the BSSN system. Enforced constraints and their derivatives can be added to any other definition, constraint or evolution equation without altering the continuum system. In particular there are two definitions of the BSSN auxiliary variable $\bar{\Gamma}^i$,

$$\bar{\Gamma}^i = -\bar{\gamma}^{ij}_{,j} = \bar{\gamma}^{jk}\bar{\Gamma}^i_{jk}, \tag{4.114}$$

equivalent only up to additions of derivatives of the $D$ constraint and only in coordinates where $\det\bar{\gamma} = 1$. In spherical coordinates they are not; if the cartesian $D$ constraint is tensorially transformed to spherical coordinates it becomes

$$D = \ln(\bar{\gamma}_{rr}\bar{\gamma}_T^2) = 0 \tag{4.115}$$

and the last of the equalities in (4.114) has to be abandoned. The transformed cartesian BSSN auxiliary variable $\bar{\Gamma}^i$ with $D_{,r}$ constraint addition is

$$\bar{\Gamma}^r = (1 - c_\Gamma)\frac{\bar{\gamma}_{rr,r}}{\bar{\gamma}_{rr}^2} - 2c_\Gamma\frac{\bar{\gamma}_{T,r}}{\bar{\gamma}_T\bar{\gamma}_{rr}} - \frac{2}{r}\Big(\frac{1}{\bar{\gamma}_{rr}} - \frac{1}{\bar{\gamma}_T}\Big) = 0, \tag{4.116}$$

where $c_\Gamma$ is constant. It would be gratifying if one choice of $c_\Gamma$ naturally gave the appropriate reduction, but it is not so. The two definitions of $\bar{\Gamma}^i$ (4.114) are both used in the derivation of the evolution equations, so neither can be taken exclusively. The first definition is used in deriving the evolution equation for the

$\bar{\Gamma}^i$'s and the second in those of the $A_{ij}$'s. For the $\bar{\Gamma}^r$ evolution equation $c_\Gamma = 0$ is the natural choice, whereas for the $\bar{A}_{rr}$ and $\bar{A}_T$ equations $c_\Gamma = 1/2$ can be taken. These values of $c_\Gamma$ correspond to the first and second definitions of $\bar{\Gamma}^i$.

To get around the ambiguity the $D$ and $T$ constraints are used to ensure that the spherical reduction chosen corresponds to the standard BSSN system even when the $D$ and $T$ constraints are not imposed; that is, the following spherical reduction of the BSSN system corresponds term by term to a spherical reduction of the standard three dimensional cartesian BSSN system even without constraint projection.

The spherical BSSN evolution equations are given by

$$\dot{\bar{\gamma}}_{rr} = \beta\bar{\gamma}_{rr,r} + \frac{4}{3}\bar{\gamma}_{rr}\beta_{,r} - \frac{4}{3r}\beta\bar{\gamma}_{rr} - 2\alpha\bar{A}_{rr}, \tag{4.117}$$

$$\dot{\bar{\gamma}}_{T} = \beta\bar{\gamma}_{T,r} - \frac{2}{3}\bar{\gamma}_{T}\beta_{,r} + \frac{2}{3r}\beta\bar{\gamma}_{T} - 2\alpha\bar{A}_{T}, \tag{4.118}$$

$$\dot{\phi} = -\frac{1}{6}\alpha K + \beta\phi_{,r} + \frac{1}{6}\beta_{,r} + \frac{\beta}{3r}, \tag{4.119}$$

$$\begin{aligned}\dot{\bar{A}}_{rr} = {} & \beta\bar{A}_{rr,r} + \frac{4}{3}\bar{A}_{rr}\beta_{,r} - \frac{4}{3r}\beta\bar{A}_{rr} + \alpha\Big(K\bar{A}_{rr} - 2\frac{\bar{A}_{rr}^2}{\bar{\gamma}_{rr}}\Big) \\ & + e^{-4\phi}\Big(-\frac{2}{3}\alpha_{,rr} + \Big(\frac{\bar{\gamma}_{rr,r}}{3\bar{\gamma}_{rr}} + \frac{\bar{\gamma}_{T,r}}{3\bar{\gamma}_{T}} + \frac{8}{3}\phi_{,r} + \frac{2}{3r}\Big)\alpha_{,r}\Big) \\ & + e^{-4\phi}\alpha\Bigg(-\frac{4}{3}\phi_{,rr} - \frac{\bar{\gamma}_{rr,rr}}{3\bar{\gamma}_{rr}} + \frac{\bar{\gamma}_{T,rr}}{3\bar{\gamma}_{T}} + \frac{2}{3}\bar{\gamma}_{rr}\bar{\Gamma}^{r}_{,r} + \frac{2\bar{\gamma}_{rr,r}^2}{3\bar{\gamma}_{rr}^2} \\ & - \frac{\bar{\gamma}_{rr,r}\bar{\gamma}_{T,r}}{2\bar{\gamma}_{rr}\bar{\gamma}_{T}} - \frac{\bar{\gamma}_{T,r}^2}{\bar{\gamma}_{T}^2} + \frac{2\bar{\gamma}_{rr,r}\phi_{,r}}{3\bar{\gamma}_{rr}} + \frac{2\bar{\gamma}_{T,r}\phi_{,r}}{3\bar{\gamma}_{T}} + \frac{8}{3}\phi_{,r}^2 \\ & + \frac{2}{3r}\Big(2\phi_{,r} - \bar{\gamma}_{rr}\bar{\Gamma}^{r} - \frac{\bar{\gamma}_{rr,r}}{\bar{\gamma}_{rr}} + \frac{2\bar{\gamma}_{rr}\gamma_{T,r}}{\gamma_{T}^2} - \frac{\bar{\gamma}_{T,r}}{\bar{\gamma}_{T}}\Big) \\ & + \frac{2}{r^2}\Big(\frac{\bar{\gamma}_{rr}}{\bar{\gamma}_{T}} - 1\Big)\Bigg),\end{aligned} \tag{4.120}$$

$$\begin{aligned}\dot{\bar{A}}_{T} = {} & \beta\bar{A}_{T,r} - \frac{2}{3}\bar{A}_{T}\beta_{,r} + \frac{2}{3r}\beta\bar{A}_{T} + \alpha\Big(K\bar{A}_{T} - 2\frac{\bar{A}_{T}^2}{\bar{\gamma}_{T}}\Big) \\ & + e^{-4\phi}\Big(\frac{\bar{\gamma}_{T}}{3\bar{\gamma}_{rr}}\alpha_{,rr} - \Big(4\bar{\gamma}_{T}\phi_{,r} + \frac{1}{2}\bar{\gamma}_{T,r} + \frac{\bar{\gamma}_{T}}{2\bar{\gamma}_{rr}}\bar{\gamma}_{rr,r} + \frac{1}{r}\bar{\gamma}_{T}\Big)\frac{\alpha_{,r}}{3\bar{\gamma}_{rr}}\Big) \\ & + e^{-4\phi}\alpha\Bigg(\frac{\bar{\gamma}_{T}}{6\bar{\gamma}_{rr}^2}\bar{\gamma}_{rr,rr} - \frac{\bar{\gamma}_{T,rr}}{6\bar{\gamma}_{rr}} + \frac{2\bar{\gamma}_{T}}{3\bar{\gamma}_{rr}}\phi_{,rr} - \frac{1}{3}\bar{\gamma}_{T}\bar{\Gamma}^{r}_{,r} - \frac{\bar{\gamma}_{T}\bar{\gamma}_{rr,r}^2}{3\bar{\gamma}_{rr}^3} \\ & + \frac{\bar{\gamma}_{rr,r}\bar{\gamma}_{T,r}}{4\bar{\gamma}_{rr}^2} + \frac{\bar{\gamma}_{T,r}^2}{6\bar{\gamma}_{rr}\bar{\gamma}_{T}} - \frac{\bar{\gamma}_{T}\bar{\gamma}_{rr,r}\phi_{,r}}{3\bar{\gamma}_{rr}^2} - \frac{\gamma_{T,r}\phi_{,r}}{3\bar{\gamma}_{rr}} - \frac{4\bar{\gamma}_{T}\phi_{,r}^2}{3\bar{\gamma}_{rr}} \\ & + \frac{1}{3r}\Big(\bar{\gamma}_{T}\bar{\Gamma}^{r} + \frac{\bar{\gamma}_{T}}{\bar{\gamma}_{rr}^2}\bar{\gamma}_{rr,r} + \frac{\bar{\gamma}_{T,r}}{\bar{\gamma}_{rr}} - \frac{2\bar{\gamma}_{T,r}}{\bar{\gamma}_{T}} - \frac{2\bar{\gamma}_{T}}{\bar{\gamma}_{rr}}\phi_{,r}\Big) \\ & + \frac{1}{r^2}\Big(\frac{\bar{\gamma}_{T}}{\bar{\gamma}_{rr}} - 1\Big)\Bigg),\end{aligned} \tag{4.121}$$

$$\begin{aligned}\dot{K} = {} & \beta K_{,r} + \alpha\Big(\frac{\bar{A}_{rr}^2}{\bar{\gamma}_{rr}^2} + 2\frac{\bar{A}_{T}^2}{\bar{\gamma}_{T}^2} + \frac{1}{3}K\Big) \\ & + e^{-4\phi}\Big(-\frac{\alpha_{,rr}}{\bar{\gamma}_{rr}} + \Big(\frac{\bar{\gamma}_{rr,r}}{2\bar{\gamma}_{rr}} - \frac{\bar{\gamma}_{T,r}}{\bar{\gamma}_{T}} - \frac{2}{r} - 2\phi_{,r}\Big)\frac{\alpha_{,r}}{\bar{\gamma}_{rr}}\Big)\end{aligned} \tag{4.122}$$

and finally

$$\begin{aligned}
\dot{\bar{\Gamma}}^r &= \frac{4\beta_{,rr}}{3\bar{\gamma}_{rr}} + \frac{2}{r}\Big(\beta_{,r} - \frac{\beta}{r}\Big)\Big(\frac{1}{\bar{\gamma}_T} + \frac{1}{3\bar{\gamma}_{rr}}\Big) \\
&\quad + \beta\bar{\Gamma}^r_{,r} + \frac{1}{3}\Big(\frac{4\beta}{r} - \beta_{,r}\Big)\left(\frac{1-c_\Gamma}{\bar{\gamma}_{rr}^2}\bar{\gamma}_{rr,r} - \frac{2c_\Gamma}{\bar{\gamma}_{rr}\bar{\gamma}_T}\bar{\gamma}_{T,r} + \frac{2}{r}\Big(\frac{1}{\bar{\gamma}_T} - \frac{1}{\bar{\gamma}_{rr}}\Big)\right) \\
&\quad - 2\frac{\bar{A}_{rr}\alpha_{,r}}{\bar{\gamma}_{rr}^2} + 2\alpha\left(\frac{\bar{A}_{rr}}{\bar{\gamma}_{rr}^3}\bar{\gamma}_{rr,r} + \Big(\frac{\bar{A}_{rr}}{\bar{\gamma}_{rr}} - \frac{\bar{A}_T}{\bar{\gamma}_T}\Big)\frac{\bar{\gamma}_{T,r}}{\bar{\gamma}_{rr}\bar{\gamma}_T} - \frac{2K_{,r}}{3\bar{\gamma}_{rr}}\right. \\
&\quad \left. + \frac{6\bar{A}_{rr}}{\bar{\gamma}_{rr}^2}\phi_{,r} + \frac{2}{r}\frac{\bar{A}_T}{\bar{\gamma}_T}\Big(\frac{1}{\bar{\gamma}_T} - \frac{1}{\bar{\gamma}_{rr}}\Big)\right). \qquad (4.123)
\end{aligned}$$

The system has constraints

$$\begin{aligned}
H &\equiv 2\frac{\bar{A}_{rr}\bar{A}_T}{\bar{\gamma}_{rr}\bar{\gamma}_T} + \frac{\bar{A}_T^2}{\bar{\gamma}_T^2} + \frac{1}{3}K^2 \\
&\quad + e^{-4\phi}\left(-\frac{\bar{\gamma}_{T,rr}}{\bar{\gamma}_{rr}\bar{\gamma}_T} - 4\frac{\phi_{,rr}}{\bar{\gamma}_{rr}} + \frac{\bar{\gamma}_{rr,r}\bar{\gamma}_T}{2\bar{\gamma}_{rr}^2\gamma_T}\right. \\
&\quad + \frac{\bar{\gamma}_{T,r}}{4\bar{\gamma}_{rr}\bar{\gamma}_T^2} + 2\frac{\bar{\gamma}_{rr,r}\phi_{,r}}{\bar{\gamma}_{rr}^2} - 4\frac{\bar{\gamma}_T\phi_{,r}}{\bar{\gamma}_{rr}\bar{\gamma}_T} - 4\frac{\phi_{,r}^2}{\bar{\gamma}_{rr}} \\
&\quad \left. + \frac{1}{r\bar{\gamma}_{rr}}\Big(\frac{\bar{\gamma}_{rr,r}}{\bar{\gamma}_{rr}} - 3\frac{\bar{\gamma}_{T,r}}{\bar{\gamma}_T} - 8\phi_{,r}\Big) + \frac{1}{r^2}\Big(\frac{1}{\bar{\gamma}_{rr}} - \frac{1}{\bar{\gamma}_T}\Big)\right) = 0, \qquad (4.124) \\
M_r &\equiv -2\frac{\bar{A}_{T,r}}{\bar{\gamma}_T} - \frac{2}{3}K_{,r} + \frac{2}{r}\Big(\frac{\bar{A}_{rr}}{\bar{\gamma}_{rr}} - \frac{\bar{A}_T}{\bar{\gamma}_T}\Big) + \Big(\frac{\bar{A}_{rr}}{\bar{\gamma}_{rr}} + \frac{\bar{A}_T}{\bar{\gamma}_T}\Big)\frac{\bar{\gamma}_{T,r}}{\bar{\gamma}_T} \\
&\quad + 4\Big(\frac{\bar{A}_{rr}}{\bar{\gamma}_{rr}} - \frac{\bar{A}_T}{\bar{\gamma}_T}\Big)\phi_{,r} = 0, \qquad (4.125) \\
G_r &\equiv \bar{\gamma}_{rr}\bar{\Gamma}^r + (c_{\bar{\Gamma}} - 1)\frac{\bar{\gamma}_{rr,r}}{\bar{\gamma}_{rr}} + 2c_{\bar{\Gamma}}\frac{\bar{\gamma}_{T,r}}{\bar{\gamma}_T} + \frac{2}{r}\Big(1 - \frac{\bar{\gamma}_{rr}}{\bar{\gamma}_T}\Big) = 0, \qquad (4.126) \\
D &\equiv \ln(\bar{\gamma}_{rr}\bar{\gamma}_T^2) = 0, \qquad (4.127) \\
T &\equiv \frac{\bar{A}_{rr}}{\bar{\gamma}_{rr}} + 2\frac{\bar{A}_T}{\bar{\gamma}_T} = 0. \qquad (4.128)
\end{aligned}$$

## 4.7 Constraint damping

In [3] Gundlach et al. consider extensions of the ADM equations (4.41,4.42) in which the constraints are damped (so-called $\lambda$-systems). They consider the Z4 system and alter it in the hope of creating a $\lambda$-system. The constraints of the system

(which is equivalent to the Einstein equations written in harmonic or generalized harmonic form) are found to be damped. The constraint damping scheme was subsequently used by Pretorious [24] in the first successful evolutions of merging binary blackholes. In this section the damping scheme is extended to the BSSN-Θ and NOR-Θ systems and analyzed in a spherical context.

### 4.7.1 Damping terms

The BSSN-Θ and NOR-Θ systems are straightforward expansions. In addition to evolving $\gamma_{ij}$, $K_{ij}$ and $f_i$, a new variable $\Theta$ evolves according to

$$\dot{\Theta} = \mathcal{L}_\beta \Theta + \alpha\Big(\frac{1}{2}H + G^k_{,k} - D_k(\ln\alpha)G^k\Big) \tag{4.129}$$

The new variable is coupled with the rest of the system by

$$\dot{f}_i = \cdots + \alpha(D_i\Theta + D_i(\ln\alpha)\Theta). \tag{4.130}$$

It may be possible to derive the NOR-Θ system by considering the slight generalization to the Z4 vacuum equations

$$G_{ab} + \hat{\nabla}_a Z_b + \hat{\nabla}_b Z_a - g_{ab}\hat{\nabla}^c Z_c = 0, \tag{4.131}$$

where $\hat{\nabla}_a$ is a flat auxiliary covariant derivative with $\Gamma^i{}_{jk} = 0$ in preferred Cartesian coordinates. This geometric approach is not followed here for two reasons. Firstly the beautiful covariant wave equation for the constraints presented in [3]

$$\Box Z_a + R_{ab}Z^b = 0, \tag{4.132}$$

does not follow without $\nabla_a = \hat{\nabla}_a$, so the constraint damping scheme cannot be analyzed in the same way. Secondly the BSSN definition constraint $G_i$ does not evolve with a full Lie derivative along the shift and so cannot be derived geometrically as the $3+1$ decomposition of a 4-dimensional system.

Constraint damping terms can be added to the system

$$\dot{K}_{ij} = \cdots - \alpha\kappa\gamma_{ij}\Theta, \tag{4.133}$$

$$\dot{f}_i = \cdots - \alpha\kappa G_i, \tag{4.134}$$

$$\dot{\Theta} = \cdots - 2\alpha\kappa\Theta. \tag{4.135}$$

The damping terms should be able to control sufficiently small definition constraint violation. The time derivatives of the definition constraints are essentially given by the Hamiltonian and Momentum constraints, so the damping ought to control their growth as well.

### 4.7.2 Mode analysis

If the constraint evolution systems are approximated by their principal part and constraint damping terms, the damped spherical constraint systems for Z4, NOR-$\Theta$ and BSSN-$\Theta$ can be reduced to

$$\partial_0\Theta \simeq \frac{1}{2}H + \frac{1}{\gamma_{rr}}G_{r,r}, \tag{4.136}$$

$$\partial_0 G_r \simeq M_{r,r} + \Theta_{,r}, \tag{4.137}$$

$$\partial_0 H \simeq H_{,r} - \frac{2}{\gamma_{rr}}M_{r,r}, \tag{4.138}$$

$$\partial_0 M_r \simeq M_{r,r} - \frac{1}{2}H_{,r}, \tag{4.139}$$

where the $G_i$ and $Z_i$ constraints have been identified; since the system implicitly contains third spatial derivatives of the metric, second derivatives of the definition constraints are principal in the $H$ and $M_i$ evolution equations. Spherical symmetry suppresses such terms, but in general they are present. Substituting the plane-wave ansatz

$$\begin{pmatrix} \Theta(t,r) & G_r(t,r) & H(t,r) & M_r(t,r) \end{pmatrix}^T = e^{st+i\omega r} \begin{pmatrix} \hat{\Theta} & \hat{G}_r & \hat{H} & \hat{M}_r \end{pmatrix}^T \tag{4.140}$$

where $\hat{\Theta}$, $\hat{G}_r$, $\hat{H}$ and $\hat{M}_r$ are constants, gives rise to the eigenvalue problem

$$\begin{pmatrix} -s-2\kappa & \frac{i\omega}{\gamma_{rr}} & \frac{1}{2} & 0 \\ i\omega & -s-\kappa & 0 & 1 \\ -4\kappa K & 0 & -s & -\frac{2i\omega}{\gamma_{rr}} \\ 2\kappa i\omega + 2\kappa \log(\alpha)_{,r} & 0 & -\frac{i\omega}{2} & -s \end{pmatrix} \begin{pmatrix} \hat{\Theta} \\ \hat{G}_r \\ \hat{H} \\ \hat{M}_r \end{pmatrix} = 0, \qquad (4.141)$$

which around flat-space has solutions

$$s = -\kappa \pm \sqrt{\kappa^2 - \omega^2}, \qquad s = \frac{1}{2}\big(-\kappa \pm \sqrt{\kappa^2 - 4\omega^2}\big), \qquad (4.142)$$

so that the Re $s < 0$ is satisfied for every $\kappa > 0$ and the definition constraints are damped which should control the growth of the Hamiltonian and momentum constraints. This result is not unexpected since the approximations reduce the calculation to the case considered in [3]. This calculation shows that in some approximation the spherical BSSN-$\Theta$ and NOR-$\Theta$ constraint systems can be damped in the same way as the $Z4$ constraint system.

Note that if the condition $\Theta \to 0$ is imposed, repeating the analysis reveals undamped modes. For the BSSN or NOR systems to be fully damped they must be expanded with the $\Theta$-variable.

# Chapter 5

# Mathematical analysis of asymptotically null slices

This chapter was published as part of a paper written in collaboration with G Calabrese and C Gundach [1].

## 5.1 Introduction

Numerical simulations of astrophysical events in general relativity are carried out on a numerical domain that comprises a central strong field zone surrounded by a much larger outer zone which contains no matter, where the fields are weak, and in which gravitational waves are mostly outgoing.

One reason for making the numerical domain large is mathematical. Boundary conditions (BCs) for the continuum initial-boundary value problem which are both compatible with the Einstein constraints and make the problem well-posed have been suggested only recently [25] and are still untested numerically. BCs which are consistent with the constraints (but not proven to be well-posed) [26] have been used successfully in 3D testbed simulations [27, 28]. Large simulations of

astrophysically interesting scenarios have so far been using BCs at finite radius (with the exception of [24], see below) that are incompatible with the constraints, so that finite constraint violations propagate in from the boundary even in the limit of infinite resolution.

A second reason is physical. The central object should be isolated with no incoming gravitational radiation. This cannot be achieved with purely local BCs. For the same reason gravitational radiation cannot be read off reliably close to the source.

The physical problem can be reduced by pushing the outer boundary to larger radius, and the mathematical problem will be alleviated at least by making the domain of dependence of the initial data larger. There is empirical evidence that the dominant error in astrophysics-type GR simulations is from the boundary, and that it can be alleviated for example by using nested boxes mesh refinement to push the outer boundary further out [29, 30, 31].

A radical approach to both the mathematical and the physical problems is to represent a complete asymptotically flat spacetime on the numerical domain. The no ingoing radiation condition can then be imposed exactly at past null infinity $\mathscr{I}^-$, and the outgoing radiation can be read off exactly at future null infinity $\mathscr{I}^+$. Regularising the field equations at infinity requires embedding the Einstein equations into a much larger system called the conformal field equations [8], but this system has not yet been used for astrophysical simulations. Alternatively, the Einstein equations can be regularised at $\mathscr{I}$ using retarded time as a null coordinate [32], but this approach cannot be used in the central strong field region because the null cones form caustics.

Finally, space can be compactified on standard spacelike slices going out to $i^0$. If the initial data are stationary outside a central region one can then get away with a pseudo-regularisation of the field equations in their discretised form at the compactification boundary [33, 34, 24]. In the continuum equations no gravitational waves reach $i^0$ and no evolution takes place there. In the discretised equations

spurious radiation must be suppressed by artificial dissipation (or the implicit dissipation of the discretisation) before reaching the compactification boundary.

One key ingredient of the conformal field equations approach is the use of asymptotically null time slices which terminate at $\mathscr{I}^+$, together with a compactification of the radial coordinate. It has been suggested to use such coordinates in numerical relativity, but to introduce an artificial outer boundary at some very large radius and to use the standard form of the Einstein equations [35, 36]. Fig. 5.1 illustrates this approach. Ingoing (backscattered) waves at large radius are increasingly lost in numerical simulations in this approach because they are not resolved on any finite resolution grid. It is sometimes not appreciated that all approaches that put $\mathscr{I}^+$ at a finite coordinate value, in particular the conformal field equations and the Cauchy-characteristic matching approaches, suffer from the same shortcoming. For example, in Minkowski spacetime with metric $ds^2 = -dUdV + R^2 d\Omega^2$ the conformal approach would introduce a compactification $U = \tan u$, $V = \tan v$ on a grid with constant resolution $\Delta u$ and $\Delta v$. This implies $\Delta V = \sec^2 \Delta v \simeq V^{-2}\Delta v$ (as $V \to \infty$), so that any ingoing waves with period $f$ are no longer resolved for $V \gtrsim (f\Delta v)^{-1/2}$. A similar argument holds for the characteristic approach on outgoing null cones.

In this paper, we shall restrict ourselves to the toy model of the wave equation on Minkowski or Reissner-Nordström spacetime. In Sect. 5.2 we investigate in some detail the relationship between radial stretching or compactification, bending up the slices, the coordinate speeds of light, and the global structure of the slices. We propose a one-parameter family of asymptotically null slices comprising flat slices at one extreme and hyperboloidal slices at the other.

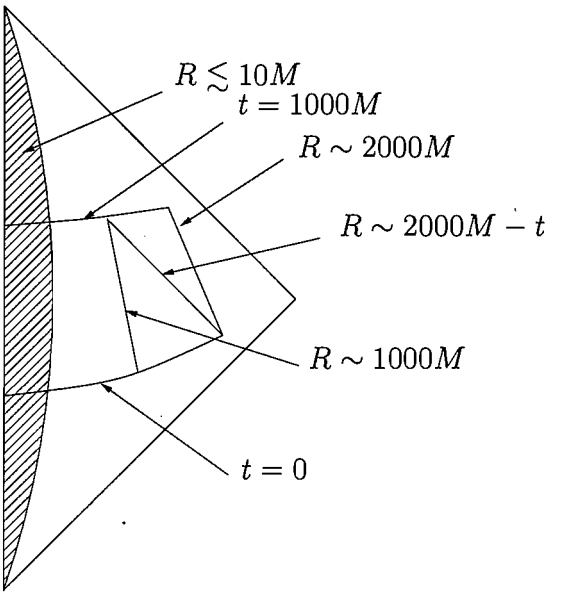


Figure 5.1: A schematic spacetime diagram to illustrate that if the artificial outer boundary is pushed out to sufficiently large radius (here $R = 2000M$) outgoing gravitational radiation can be read off at very large radius (here $R = 1000M$) for a long time (here $t = 1000M$) without being contaminated by unphysical BCs at the artificial outer boundary (assuming that no information travels faster than light).

## 5.2 Mathematical analysis

### 5.2.1 Spherically symmetric slices in Minkowski spacetime

The metric of Minkowski spacetime in standard spherical polar coordinates is

$$\mathrm{d}s^2 = -\mathrm{d}T^2 + \mathrm{d}R^2 + R^2 d\Omega^2, \tag{5.1}$$

where $d\Omega^2 \equiv d\theta^2 + \sin^2\theta\, d\varphi^2$.

Consider the flat space wave equation as a toy model for the linearised Einstein equations. An outgoing wave $\phi$ emanating from a central region can be approximated as

$$\phi(T, R, \theta, \varphi) \simeq \sum_{l=0}^{l_{\max}} \sum_{m=-l}^{l} \phi_{lm}(U) R^{-1} Y_{lm}(\theta, \varphi) \tag{5.2}$$

for some small finite $l_{\max}$, where the $Y_{lm}$ are spherical harmonics and $U = T - R$ is retarded time. To resolve this, constant spatial resolution $\Delta x$, $\Delta y$, $\Delta z$ is not required, but only constant angular resolution $\Delta\theta$, $\Delta\varphi$. Similarly, constant resolution in $R$ and $T$ separately is not required, but only constant resolution in $U$. If the slices of constant coordinate time $t$ "bend up" such that they approximate slices of constant $U$ asymptotically as $R \to \infty$, then the radial grid spacing $\Delta R$ can be allowed to diverge in this limit.

To study this quantitatively, we make the change of coordinates

$$t = T - F(R), \tag{5.3}$$

$$R = R(r), \tag{5.4}$$

where $F(R)$ controls the slicing, and $R(r)$ the spatial coordinates on the slices. The new slicing is static, that is, Lie-dragged by the Killing vector $\partial/\partial T$.

The metric in 3+1 in form in the new coordinates is

$$\mathrm{d}s^2 = -\alpha^2 \mathrm{d}t^2 + \gamma_{rr}(\mathrm{d}r + \beta^r \mathrm{d}t)^2 + \gamma_{\theta\theta}\mathrm{d}\Omega^2, \tag{5.5}$$

with the lapse, shift, 3-metric and extrinsic curvature given by

$$\alpha = \frac{1}{(1-F'^2)^{\frac{1}{2}}}, \tag{5.6}$$

$$\beta^r = -\frac{F'}{R'(1-F'^2)}, \tag{5.7}$$

$$\gamma_{rr} = R'^2(1-F'^2), \tag{5.8}$$

$$\gamma_{\theta\theta} = R^2, \tag{5.9}$$

$$K_{rr} = -\frac{F''R'^2}{(1-F'^2)^{\frac{1}{2}}}, \tag{5.10}$$

$$K_{\theta\theta} = -\frac{F'R}{(1-F'^2)^{\frac{1}{2}}}. \tag{5.11}$$

Note that $\alpha \geq 1$. Here and in the following $F' \equiv dF/dR$ and $R' \equiv dR/dr$. The coordinate light speeds in the radial and tangential directions are

$$c_\pm \equiv \left.\frac{\mathrm{d}r}{\mathrm{d}t}\right|_{\theta,\varphi} = \pm\frac{\alpha}{\sqrt{\gamma_{rr}}} - \beta^r = \pm\frac{1}{R'(1\mp F')}, \tag{5.12}$$

$$c_\theta \equiv \left.\frac{\mathrm{d}\theta}{\mathrm{d}t}\right|_{r,\varphi} = \sqrt{\frac{-g_{tt}}{\gamma_{\theta\theta}}} = \frac{1}{R}. \tag{5.13}$$

We can also express the radial coordinate speeds of light $dr/dt = c_\pm$ directly in terms of $dR/dT = C_\pm$ in the form

$$c_\pm^{-1} = R'(C_\pm^{-1} - F'), \tag{5.14}$$

and this relation holds for any spherically symmetric metric.

### 5.2.2 Stability conditions

We consider a numerical stencil centred at the grid point $x_0^i$ at time $t_0$, and for simplicity of presentation we shift the origin of the coordinates so that $x_0^i = 0$ and $t_0 = 0$. We model the stencil as the square box $-\Delta x^i \leq x^i \leq \Delta x^i$ for $i = 1, 2, 3$. The time step is $\Delta t$, and for simplicity of notation we assume a two-level scheme and a three-point stencil in each spatial direction.

The intersection of the past light cone of the grid point at $x^i = 0$ and $t = \Delta t$ with the time slice $t = 0$ is the ellipsoid

$$\gamma_{ij}(x^i + \beta^i \Delta t)(x^j + \beta^j \Delta t) = \alpha^2 \Delta t^2. \tag{5.15}$$

Note that the origin of this ellipsoid is shifted from $x^i = 0$ if $\beta^i \neq 0$, and its principal axes are not aligned with the coordinate axes if $\gamma_{ij}$ is not diagonal.

The light ellipsoid fits into the stencil box (the Courant-Friedrichs-Levy (CFL) condition) if and only if in each of the three coordinate directions $i$ the maximal value of $x^i$ on the ellipsoid is less than $\Delta x^i$ and the minimal value is greater than $-\Delta x^i$. The solution of the resulting extremisation problem gives

$$\frac{\Delta x^i}{\Delta t} \geq \alpha \sqrt{\gamma^{ii}} + |\beta^i| \tag{5.16}$$

for $i = 1, 2, 3$ (no summation over $i$). This result is valid also for non-diagonal $\gamma_{ij}$.

Restricted to spherical symmetry, these conditions become

$$\frac{\Delta r}{\Delta t} \geq \frac{\alpha}{\sqrt{\gamma_{rr}}} + |\beta^r|, \tag{5.17}$$

$$\frac{\Delta \theta}{\Delta t} \geq \frac{\alpha}{R}, \tag{5.18}$$

$$\frac{\Delta \varphi}{\Delta t} \geq \frac{\alpha}{R|\sin\theta|}. \tag{5.19}$$

The factor $1/\sin\theta$ in the third condition reflects the standard problem with spherical coordinates on the $z$-axis unrelated to our coordinates and which we ignore here.

The CFL condition, which is necessary for stability, can be written as

$$|c_+| \leq k\frac{\Delta r}{\Delta t}, \quad |c_-| \leq k\frac{\Delta r}{\Delta t}, \quad c_T \leq k\frac{\Delta \theta}{\Delta t} \tag{5.20}$$

for $k = 1$, where

$$c_T \equiv \frac{\alpha}{R} = \frac{1}{R(1 - F'^2)^{1/2}}. \tag{5.21}$$

For typical explicit finite differencing methods for linear hyperbolic equations, a sufficient stability condition is then of the same form for some constant $k$ which

depends on the equation and its discretisation (allowing for any number of time levels and size of stencil). This will generalise to any hyperbolic formulation of the Einstein equations. Note that $c_T \neq c_\theta$ unless $\alpha = 1$, and that $c_T$ and not $c_\theta$ is the relevant quantity for stability.

### 5.2.3 Slicing, stretching, compactification, and lightcones

The assumption that the slice is spacelike is equivalent to $F' < 1$, and the assumption that it becomes asymptotically null is equivalent to $F' \to 1$. For simplicity let us consider functions $1 - F'$ that decay as a power of $R$ at large $R$, or

$$1 - F'(R) \sim R^{-n} \tag{5.22}$$

as $R \to \infty$, where $n > 0$. Without loss of generality we assume that the numerical grid is equally spaced in $r$. Then the CFL condition in the radial direction requires that

$$c_+ \sim \frac{R^n}{R'} \tag{5.23}$$

is bounded above as $R \to \infty$. To preserve accuracy, it should also be bounded below. (If $c_+ \to 0$ as $R \to \infty$, an outgoing wave pulse would slow down, become increasingly narrow, and be damped by numerical dissipation.) Therefore we require

$$c_+ \sim \frac{R^n}{R'} \sim \text{const.}, \tag{5.24}$$

which on integration gives us

$$r \sim R^{1-n}. \tag{5.25}$$

This means that for $0 < n < 1$ we have radial stretching

$$R(r) \sim r^{1/(1-n)}, \quad r \to \infty, \tag{5.26}$$

and for $n > 1$ we have radial compactification

$$R(r) \sim (l - r)^{-1/(n-1)}, \quad r \to l_-. \tag{5.27}$$

The special case $n = 1$ gives us

$$R(r) \sim e^r, \quad r \to \infty, \tag{5.28}$$

also a case of stretching.

We see that

$$c_- \simeq -\frac{1}{2R'} \to 0 \tag{5.29}$$

as $R \to \infty$ for either stretching or compactification. This means that ingoing wave pulses move very slowly (in $r$ and $t$) at large radius, and that they become wider (in $r$) as they move in. Although they are insufficiently resolved at large radius, they do not pose a stability problem for the finite differencing scheme (at least from the point of view of the CFL condition). We also see that

$$c_T \sim R^{n/2-1} \tag{5.30}$$

as $R \to \infty$, and so with constant angular resolution the CFL condition in the tangential directions requires $n \leq 2$.

In summary, the ansatz (5.22) for the slicing requires $0 < n \leq 2$ for the coordinate speeds in all directions to be bounded. Keeping $c_+$ bounded below as well as above means that $0 < n \leq 1$ requires radial stretching and $1 < n \leq 2$ requires radial compactification.

As a matter of convention, we always set $F(0) = 0$, $R(0) = 0$ and $R'(0) = 1$, so that $c_+(0) = 1$. For regularity we require $R(r)$ to be odd and $F(R)$ to be even. We introduce a length scale $L$ so that

$$R' \simeq \left(\frac{R}{L}\right)^n \tag{5.31}$$

as $R \to \infty$. We demand that $c_+(\infty) = 1$, which implies

$$F' \simeq 1 - \left(\frac{R}{L}\right)^{-n}. \tag{5.32}$$

Simple closed form expressions for $F(R)$ and $R(r)$ with the required asymptotic behaviour are given in sect. 5.2.7. A typical set of coordinate speeds is plotted in Fig. 5.12.

In summary, compactifying the radius without bending up the slices would mean losing the outgoing radiation. Bending up the slices without radial compactification would increase the radial outgoing characteristic speeds without limit and so violate the CFL condition in the radial direction. Bending up the slices without keeping the angular resolution constant at large radius would violate the CFL condition in the angular directions.

### 5.2.4 Global structure

The exponent $n$ can be given a geometric interpretation as follows. There are two preferred families of observers: those normal to the slicing and those along the Killing field $\partial/\partial T = \partial/\partial t$. The speed of the former relative to the latter is

$$v = -\frac{\beta^r \sqrt{\gamma_{rr}}}{\alpha}, \tag{5.33}$$

and the corresponding Lorentz factor is

$$\Gamma \equiv \frac{1}{\sqrt{1-v^2}} \simeq \frac{1}{\sqrt{2}} \left(\frac{R}{L}\right)^{n/2} \tag{5.34}$$

as $R \to \infty$.

We see that our $n > 0$ slices are asymptotically null in the precise sense that their Lorentz factor diverges as $R \to \infty$, but surprisingly this does not imply that they reach $\mathscr{I}$. Consider the null coordinates $V \equiv T + R = t + F(R) + R$ and $U \equiv T - R = t + F(R) - R$ on Minkowski spacetime. Noting that $F(R) \simeq R$ as $R \to \infty$, we find that $V \simeq 2R \to \infty$ as $R \to \infty$ on a slice of constant $t$. For $U$ on a slice of constant $t$, we find that

$$\left.\frac{dU}{dR}\right|_{t=\text{const.}} = F'(R) - 1 \simeq -\left(\frac{R}{L}\right)^{-n} \tag{5.35}$$

Integrating this relation over $R$, we find that for $n > 1$, $U$ approaches a finite value as $R \to \infty$ (or equivalently, as we have seen, $V \to \infty$) on a slice of constant $t$, and so the slice reaches a point on $\mathscr{I}$. For $n \leq 1$, $U \to -\infty$ as $V \to \infty$ on a slice

of constant $t$, and so the slice reaches $i^0$. If our slices are plotted on the standard conformal diagram, they approach $i^0$ horizontally for $n = 0$, but tangentially to $\mathscr{I}$ for $0 < n \leq 1$. For $1 < n \leq 2$ they intersect $\mathscr{I}$.

For comparison we determine the asymptotic behaviour of the standard conformal compactification of Minkowski [6]. With $U$ and $V$ as above, and $u \equiv (t-r)/2$ and $v \equiv (t+r)/2$, this is given by $U = \tan u$ and $V = \tan v$. (For consistency with the rest of this paper $u$ and $v$ have finite range and $U$ and $V$ infinite range). Clearly this is is not of the restricted form we have considered here and which gives a static slicing. But we can show that as $R \to \infty$ on a slice of constant $t$,

$$\left.\frac{dT}{dR}\right|_{t=\text{const.}} \simeq 1 - \left(\frac{R}{L(t)}\right)^{-2} \tag{5.36}$$

which we can interpret as $n = 2$ but where $L(t)$ now depends explicitly on the slice. In this compactification $c_\pm = \pm 1$ exactly, and so both ingoing and outgoing waves are represented accurately. The lines of constant $(r, \theta, \varphi)$ are no longer Killing trajectories, and so we cannot implement this gauge choice with "symmetry-seeking" coordinate conditions [37], which include almost all popular coordinate conditions.

### 5.2.5 Reissner-Nordström spacetime

To obtain asymptotically null slices in Reissner-Nordström spacetime, we start from its metric in (for example) Kerr-Schild coordinates $(T, R)$,

$$\begin{aligned} ds^2 &= -(1-f)\,dT^2 + 2f\,dT\,dR + (1+f)\,dR^2 \\ &\quad + R^2\,d\Omega^2 \quad \text{where } f(R) \equiv \frac{2m}{R} - \frac{q^2}{R^2}, \end{aligned} \tag{5.37}$$

and make a coordinate transformation of the form (5.3,5.4) to new coordinates $(t, r)$. We choose $R(r)$ to have the asymptotic behaviour (5.31) with $0 < n \leq 2$. From (5.14) we find that in order to obtain $c_+(\infty) = 1$, the asymptotic behaviour of $F(R)$ as $R \to 0$ must now be

$$F' = 1 + \frac{4m}{R} + \frac{8m^2 - 2q^2}{R^2} - \left(\frac{R}{L}\right)^{-n} + o(R^{-n}), \tag{5.38}$$

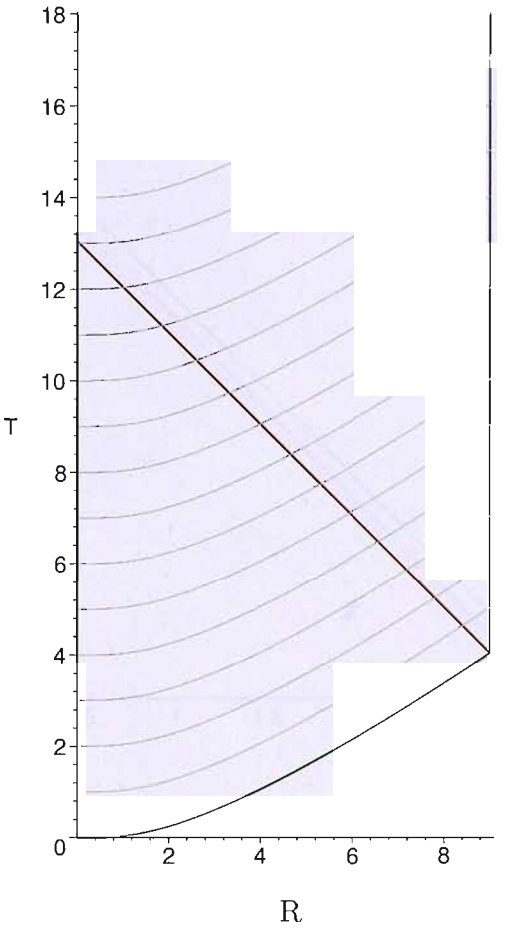


Figure 5.2: $n = \frac{1}{2}$ slices plotted with $L = 1$ up to $R = 9$. The diagonal line is the boundary of the domain of dependence of the initial data. Slices with other $n$ look similar.

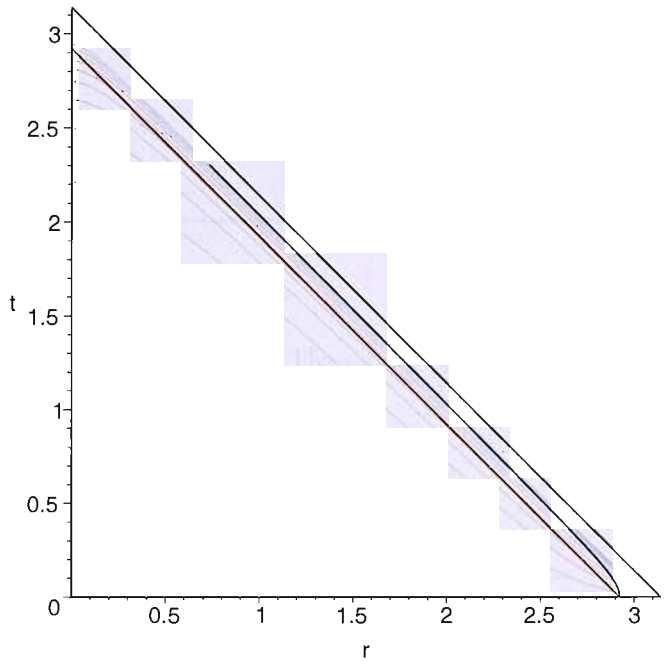


Figure 5.3: Flat ($n = 0$) slices plotted in the standard conformal diagram. The outer boundary radius and the domain of dependence of the initial data have been indicated, but the slices have been extended beyond $R_{\max}$ to infinite radius to demonstrate that they reach spacelike infinity.

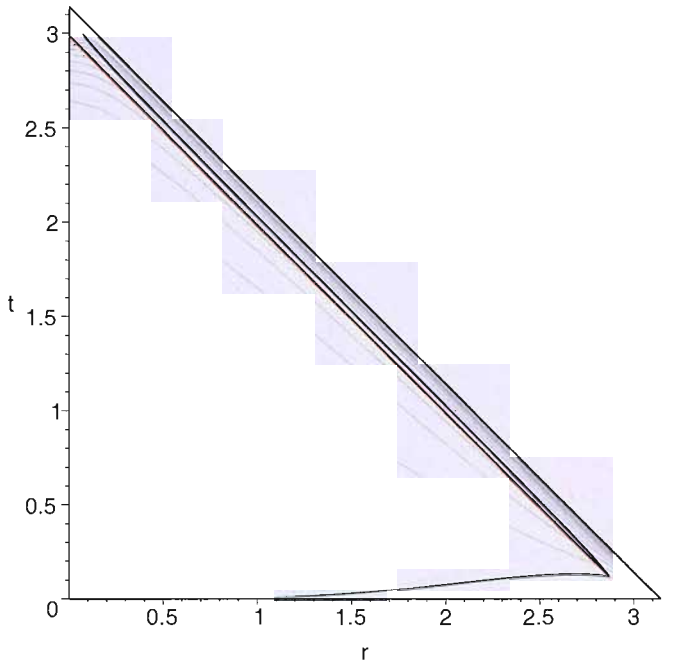


Figure 5.4: $n = \frac{1}{2}$ slices. The slices end at spacelike infinity.

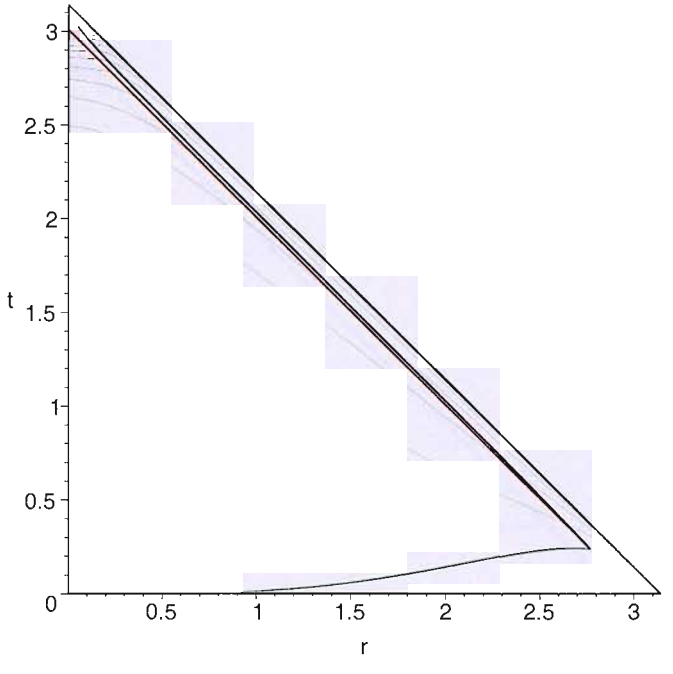


Figure 5.5: $n = 1$ slices embedded in the standard conformal diagram of Minkowski. They approach spacelike infinity tangential to future null infinity.

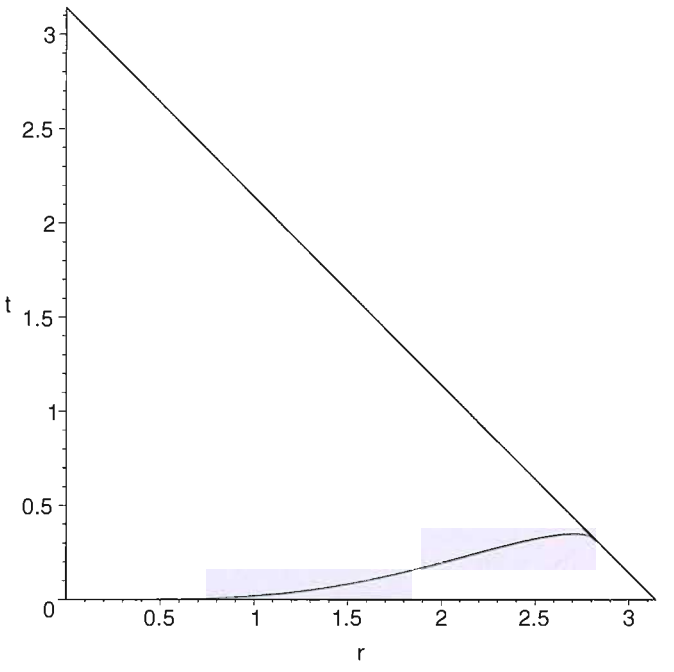


Figure 5.6: $n = \frac{3}{2}$ slices intersect future null infinity at finite retarded time.

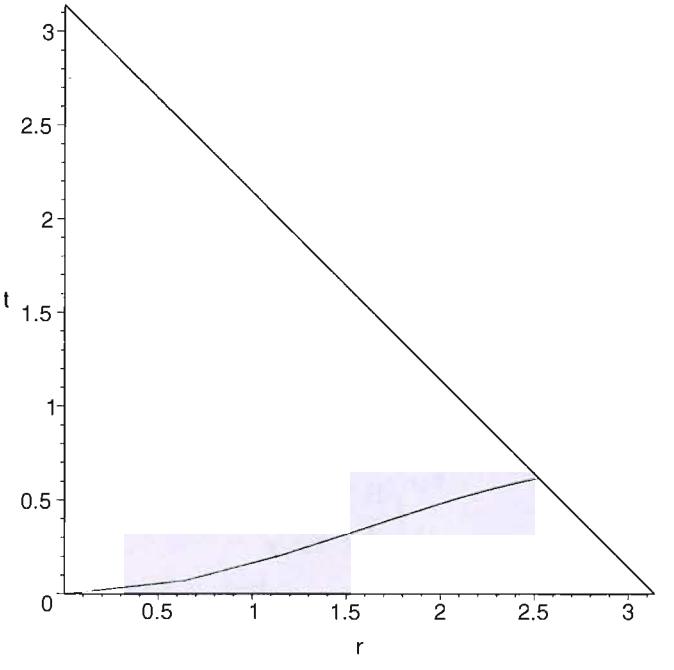


Figure 5.7: $n = 2$ slices also intersect future null infinity at finite retarded time.

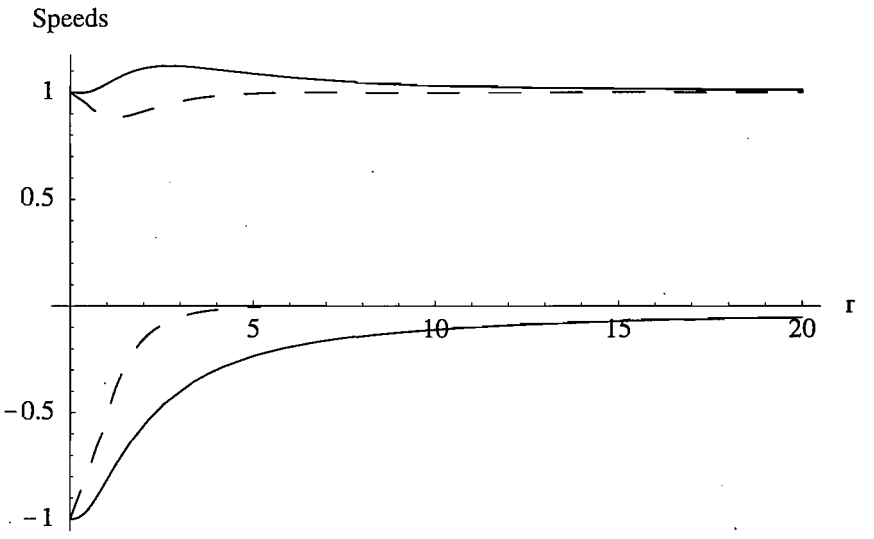


Figure 5.8: Coordinate speeds $c_+$ and $c_-$ in our examples with with $L = 1$, and $n = 1/2$ and $n = 1$ (dashed). Here $R = \infty$ corresponds to $r = \infty$.

for $0 < n \leq 2$. For $n < 2$ the $R^{-2}$ term in this expression can be omitted, and for $n < 1$ the $R^{-1}$ term can also be omitted, as they give only $o(1)$ contributions to $c_+$. Conversely, we see that for $n \geq 1$ the slicing must be corrected for the total mass of the isolated central object. In a dynamic 3D spacetime this mass would presumably be the ADM mass for $n = 1$ and the Bondi mass for $n > 1$. Although our calculations are limited to spherical symmetry, the analogy between charge and angular momentum suggests that with $n = 2$ in 3D the slicing would have to be corrected for the Bondi angular momentum as well.

Finally we note that (5.30) holds also in Reissner-Nordström spacetime. More precisely,

$$c_T \simeq \frac{1}{\sqrt{2}R}\left(\frac{R}{L}\right)^{n/2} \tag{5.39}$$

for $0 < n < 2$ with any $m$ and $q$, and

$$c_T \simeq \frac{1}{\sqrt{2}\tilde{L}}, \quad \tilde{L}^2 \equiv L^2 + 24m^2 - 4q^2 \tag{5.40}$$

for $n = 2$ as $R \to \infty$.

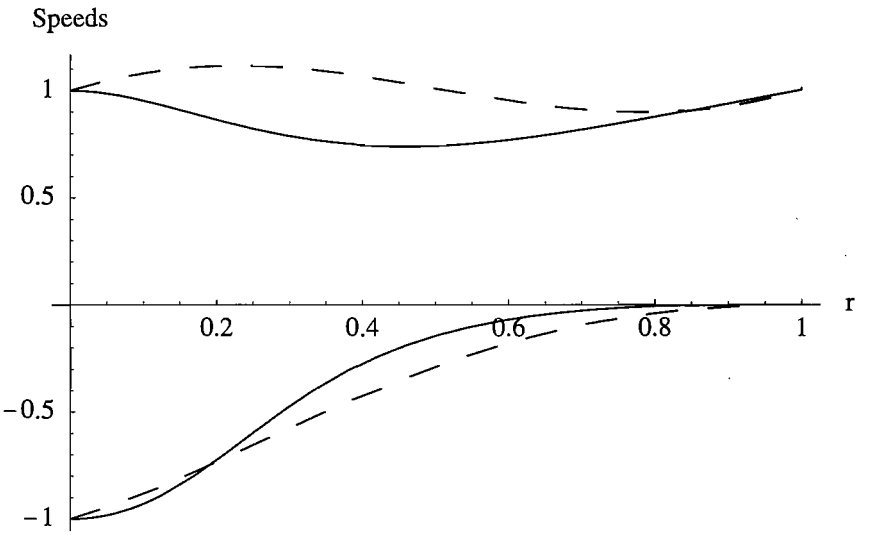


Figure 5.9: Coordinate speeds $c_+$ and $c_-$ in our examples with $l = 1$ and $n = 3/2$ and $n = 2$ (dashed), so that $R = \infty$ corresponds to $r = 1$.

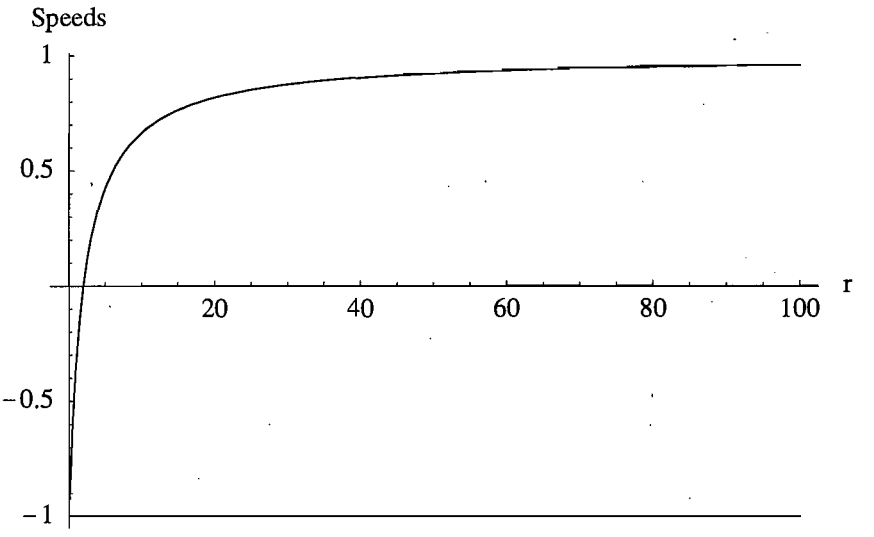


Figure 5.10: Coordinate speeds $c_+$ and $c_-$ in Kerr-Schild slicing. Here and in the following the black hole mass is $m = 1$.

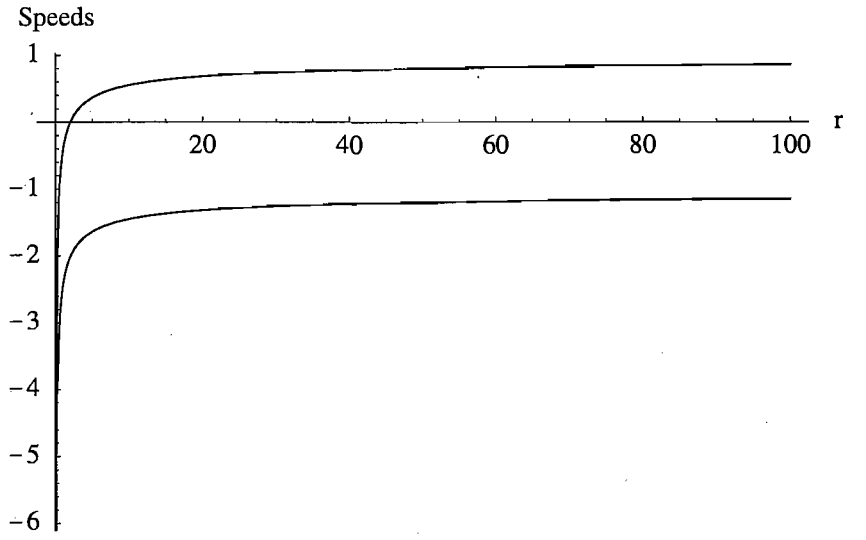


Figure 5.11: Coordinate speeds $c_+$ and $c_-$ in modified Painlevé-Güllstrand slicing.

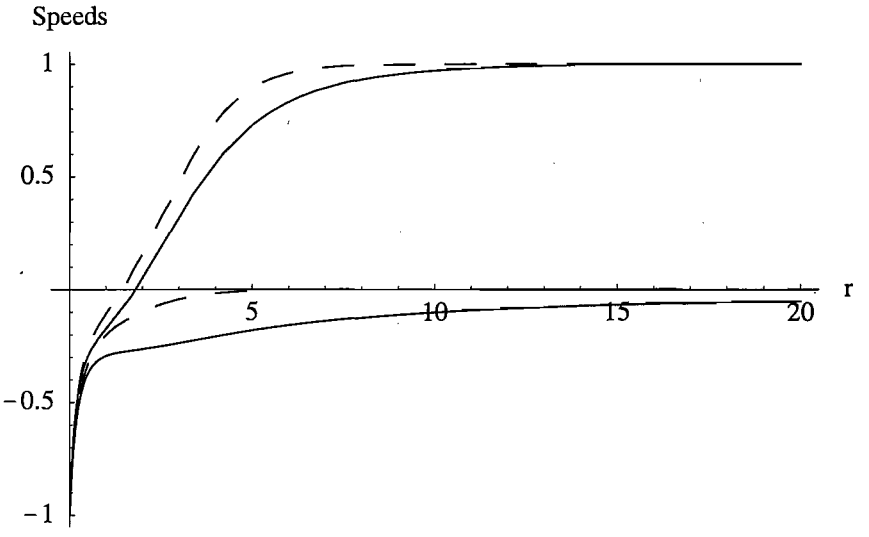


Figure 5.12: Coordinate speeds $c_+$ and $c_-$ in modified Kerr-Schild slicing, made asymptotically null with $n = \frac{1}{2}$ and $n = 1$ (dashed). $L = 1$ in both cases.

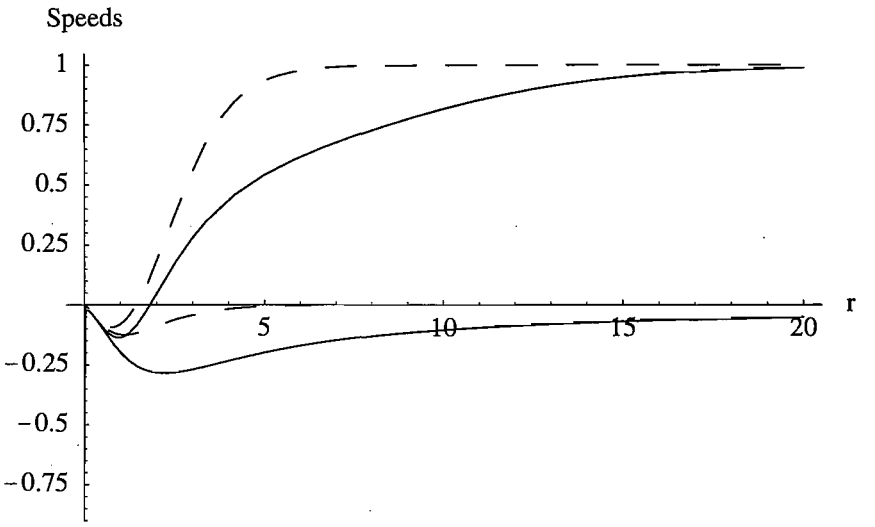


Figure 5.13: Coordinate speeds $c_+$ and $c_-$ in modified Painlevé-Güllstrand and $n = \frac{1}{2}$ and $n = 1$ (dashed). Again $L = 1$.

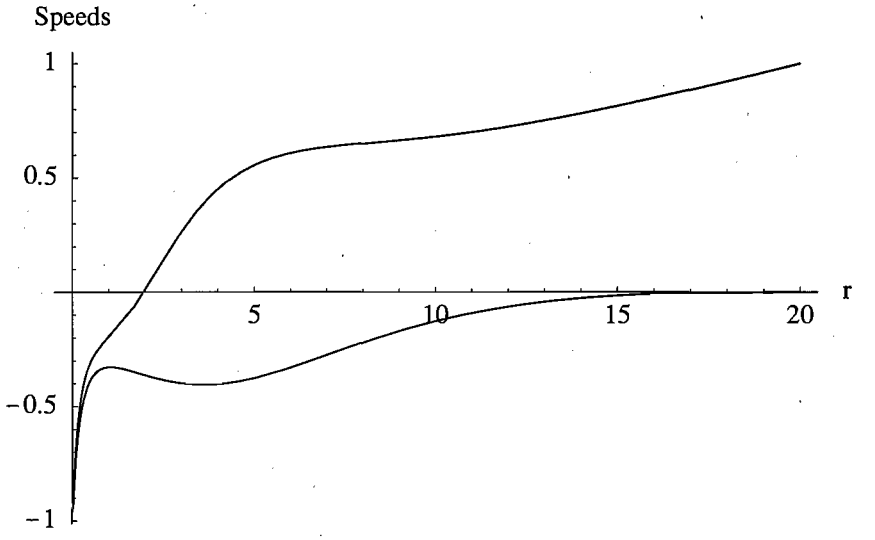


Figure 5.14: Coordinate speeds $c_+$ and $c_-$ in modified Kerr-Schild and $n = \frac{3}{2}$, with $l = 20$.

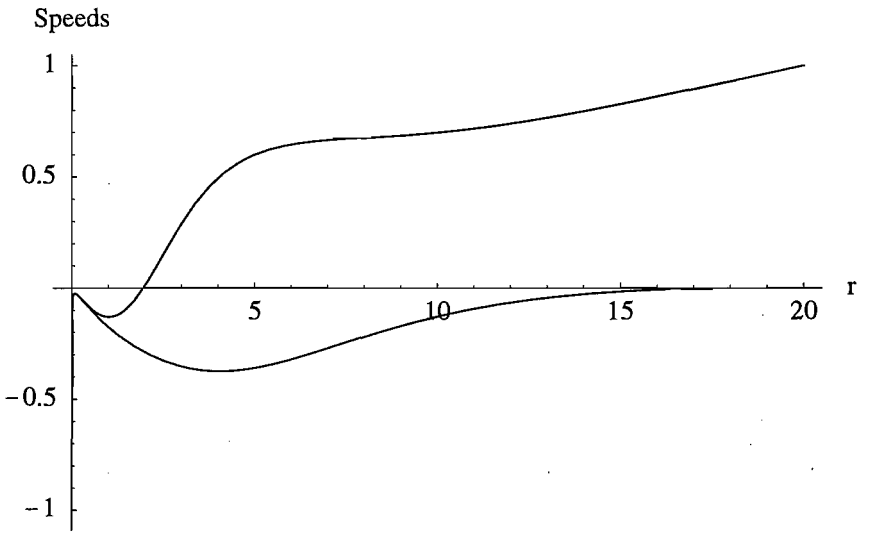


Figure 5.15: Coordinate speeds $c_+$ and $c_-$ in modified Painlevé-Güllstrand and $n = \frac{3}{2}$. Again $l = 20$.

### 5.2.6 Characterisation of $n$ in terms of 3+1 variables

We have already characterised the slicing geometrically in terms of its Lorentz factor. Another geometric characterisation is in terms of the metric and intrinsic curvature of the slices. Applying the coordinate transformation (5.3,5.4) with the asymptotic behaviour (5.31,5.38) to the metric (5.37), we find that for Minkowski with $0 < n \leq 2$ and Reissner-Nordström with $0 < n < 2$,

$$\alpha \simeq \frac{1}{\sqrt{2}}\left(\frac{R}{L}\right)^{\frac{n}{2}}, \qquad \beta^r \simeq -\frac{1}{2}, \tag{5.41}$$

$$\gamma_{rr} \simeq 2\left(\frac{R}{L}\right)^{n}, \qquad \gamma_{\theta\theta} \equiv R^2, \tag{5.42}$$

$$K_{rr} \simeq -\frac{n}{\sqrt{2}L}\left(\frac{R}{L}\right)^{\frac{3n}{2}-1}, \tag{5.43}$$

$$K_{\theta\theta} \simeq -\frac{L}{\sqrt{2}}\left(\frac{R}{L}\right)^{\frac{n}{2}+1}, \tag{5.44}$$

$$K \simeq -\frac{n}{2\sqrt{2}L}\left(\frac{R}{L}\right)^{\frac{n}{2}-1}, \tag{5.45}$$

in the limit $R \to \infty$. (For $n = 2$ with $m, q \neq 0$, the leading order coefficients change from the ones given here). $R$ is defined geometrically as the area radius. To leading order in $R$, there is no effect from the mass $m$. As $R \to \infty$, $K = K^r{}_r + 2K^\theta{}_\theta$ is dominated by $K^r{}_r$ for all $n$. For $n = 0$, $K$ vanishes identically, for $0 < n < 2$ it goes to zero as $R \to \infty$, while for $n = 2$ it approaches a constant.

### 5.2.7 Closed form coordinate transformations

We give closed-form functions $R(r)$ and $F(R)$ which have the required asymptotic behaviour (5.31) and (5.38). For the radial stretch we choose

$$R(r) = r\left(1 + \frac{r^2}{l^2}\right)^{\frac{n}{2(1-n)}}, \qquad l = \left(\frac{1}{1-n}\right)^{1/n} L \tag{5.46}$$

for the generic case $0 < n < 1$, and

$$R(r) = L \sinh \frac{r}{L} \tag{5.47}$$

for $n = 1$. The range of $r$ is $0 \leq r < \infty$. For the compactification we choose

$$R(r) = r\left(1 - \frac{r^2}{l^2}\right)^{\frac{1}{1-n}}, \qquad l = \left(\frac{2}{n-1}\right)^{1/n} L \tag{5.48}$$

for $1 < n \leq 2$. The range of $r$ is now $0 \leq r < l$.

The expression for $F(R)$ can be assembled from the functions

$$G_n(R, L) = \frac{L^n}{1-n}\left(R^2 + L^2\right)^{\frac{1-n}{2}} - \frac{L}{1-n} \tag{5.49}$$

for $0 \leq n \leq 2$ with $n \neq 1$ and

$$G_1(R, L) = \frac{L}{2} \ln\left(1 + \frac{R^2}{L^2}\right) \tag{5.50}$$

for the special value $n = 1$. They obey

$$G'_n(R, L) = \left(\frac{R}{L}\right)^{-n} + O(R^{-n-2}). \tag{5.51}$$

for all $n$ including $n = 1$. In particular,

$$G_0'(R, L) = 1 - \frac{L^2}{2R^2} + O(R^{-4}), \tag{5.52}$$

and the $R^{-2}$ term in $G_0'$ has to be taken into account in the $n = 2$ slicing. It is straightforward to construct $F(R)$ from these blocks. We only give an example here. For $0 < n < 2$ with $m = q = 0$, we can use

$$F(R) = G_0(R, L_0) - \left(\frac{L_n}{L}\right)^n G_n(R, L_n). \tag{5.53}$$

Note that $L_0$ and $L_n$ can differ from each other and from $L$ (the constant introduced in $R(r)$) as long as the corresponding amplitude is adjusted. For $n \geq 1$ with $m > 0$ and again for $n = 2$, additional terms have to be added. Similarly, to achieve a switchover from $n$ to $n_\infty < n$ at a given large $R$ we only need to add $G_{n_\infty}$ with suitable amplitude and scale.

# Chapter 6

# Scalar field evolutions on asymptotically null slices

This chapter was published as part of a paper written in collaboration with G Calabrese and C Gundach [1]. The numerical results section has been expanded with new results.

## 6.1 Method

### 6.1.1 Grid and algorithm

We solve the wave equation restricted to spherical symmetry on Minkowski and Schwarzschild spacetime. The problem has an overall scale-invariance, which we fix by evolving a Gaussian pulse of width $\sim 1$.

To investigate a problem that is roughly similar to the binary black hole problem discussed in the introduction, we use a lowest resolution of $\Delta r = 0.1$, which corresponds to $\Delta R \simeq 0.1$ in the central region, or $\sim 10$ grid points over the width of the pulse. In a realistic simulation we need to maintain a fairly constant reso-

lution in a finite inner region where the dynamics take place. We therefore choose $L$ (or equivalently $l$) so that $R'(r) \simeq 2$ at $R = 10$, which means that resolution at that radius is still half of that at the center. For $n \leq 1$ we choose $r_{\rm max}$ so that $R_{\rm max} \gtrsim 1000$, and for $n > 1$ we go all the way to $R = \infty$, with $r_{\rm max} = l$.

We solve the wave equation in the form presented in Sect. 6.2.1, using centered 2nd-order or 4th-order accurate differences in space and and 4th-order Runge-Kutta integration in time, with a Courant factor of $\Delta t/\Delta r = 0.4$. A regular origin is dealt with by imposing regularity, and taking appropriate limits in the right hand sides. For black hole excision we use extrapolation boundary conditions.

### 6.1.2 Outer boundary treatment

If the outer boundary is at finite physical radius, we impose maximally dissipative boundary conditions on $\phi$ and $\Pi$. These boundary conditions give rise to a small continuum reflection at the outer boundary. The standard MDBC takes into account only the local characteristic speeds. If the local outgoing characteristic speed is $c$, it tries to impose the form $\phi(r,t) = f(r-ct)$ on the solution. A better boundary condition would be to impose $\phi(r,t) = f(r-ct)/R$ on the solution, by adding lower-order terms to the MDBC. This would still leave unphysical reflections for non-spherical waves, and any waves in curved spacetime.

Independently of the continuum reflections, the finite differencing implementation of the boundary condition also gives rise to additional reflections which converge away with increasing resolution. These numerical reflections are much larger for all $n > 0$ slicings than with the flat $n = 0$ slicing.

However, with $n > 0$ the outer boundary condition is "almost" an outflow boundary. With $n > 0$ we have therefore tried simply extrapolating all fields at the outer boundary *as if* it was an outflow boundary. This dramatically reduces spurious reflections. The resulting problem is ill-posed already in the continuum, but we

find that blow-up only occurs at very late times, not affecting our results. A small increase in the magnitude of the (radial) shift, leaving the other metric coefficients unchanged, will turn the outer boundary into a genuine outflow boundary, although the background spacetime is then no longer Minkowski (see the Conclusions). We can then impose extrapolation boundary conditions in a way that is stable numerically. This also reduces spurious reflections.

If, for $n > 1$, the outer boundary is set at $R = \infty$, we can impose the trivial exact boundary conditions $\phi = \Pi = 0$ there. For a 2nd-order accurate finite-differencing scheme, with a 3-point stencil, this is sufficient. In order to use a 4th-order accurate centered 5-point stencil, we have, in Minkowski spacetime, set the value of $\phi$ and $\Pi$ at the grid point $N - 1$ just inside the outer boundary point from the exact solution as well. (We can of course do this only if an exact solution is known, that is in flat spacetime in spherical symmetry).

In the results presented here, we have used either MDBCs or exact BCs on Minkowski spacetime, but we have also stopped those evolutions at the time when the outgoing wave reaches the outer boundary, so that the choice of outer BC has little effect on the result. By contrast, in the Schwarzschild tests we have evolved for much longer. There we have used MDBCs, extrapolation BCs (mathematically inconsistent) and outflow boundary conditions (with a modified shift, physically inconsistent).

### 6.1.3 Initial data, error and convergence

The general exact solution of the spherical wave equation on Minkowski spacetime is

$$\phi = -\frac{f(T+R) - f(T-R)}{R}. \tag{6.1}$$

We choose $f(R) = e^{-R^2}$, which means that the wave packet we evolve has a width of $\sim 1$. This fixes an arbitrary overall scale in the problem. We obtain initial data at $t = 0$ from the exact solution, and evolve for $t > 0$ until the wave has left the

numerical grid. In our convention $t = 0$ is the slice that passes through $T = R = 0$, so that the exact solution is mainly outgoing for $t > 0$.

We measure the error $e(r,t) \equiv \phi_{\text{numerical}} - \phi_{\text{exact}}$ for $t > 0$. Results $e(r,t)$ for different slicings cannot be compared directly. We could interpolate to obtain $e(R,T)$, but instead we shall plot and compare $e(r,t_*)$ where the constant $t_* \equiv t(R = R_*, T = R_*)$ is the value of $t$ in a given slicing when the maximum of the Gaussian pulse is at physical radius $R = R_*$. The absolute values of the errors can then be meaningfully compared between slices. The plots also give us an idea of how the error is distributed over $r$. We shall use $R_* = 10, 100, 1000$, and for the compactifications $n > 1$ also $R_* = \infty$.

We check convergence by plotting $e$ at resolution $\Delta r = 0.1$ together with $4e$ ($16e$) at resolution $\Delta r = 0.05$. With 2nd-order (4th-order) convergence the two plots should coincide at high enough resolution, and the plot allows us to see where and when this indicator of convergence breaks down.

On Schwarzschild spacetime we do not have an exact solution, and so we use self-convergence at the three resolutions $\Delta r = 0.1$, 0.05 and 0.025 to establish convergence and estimate the error. We obtain initial data using the same expression as for the exact solution on Minkowski spacetime, at a time when the wave pulse is just outside the black hole and mostly outgoing. As this expression is not an exact solution on Schwarzschild, we are not simulating the same solution of the wave equation for different values of $n$, but these solutions are roughly similar, in that they represent a mostly outgoing Gaussian wave of width $\Delta R \sim 1$. We set the black hole mass to $m = 1$, so that the Schwarzschild radius and width of the outgoing pulse are similar. Their ratio should not matter since we are interested in the interaction of the outgoing pulse with the curvature at large radius, not with the black hole itself.

## 6.2 Spherical wave equation on Minkowski spacetime

We evolve an outgoing scalar field pulse on flat spacetime with different slicings with the aim of quantifying the error and establishing what fraction of grid points can be saved by using asymptotically null coordinate slices, and what effect they have on the error as the wave goes out to very large $R$. We present results for the slicing and compactification introduced above with $n = \frac{1}{2}, 1, \frac{3}{2}, 2$.

### 6.2.1 Wave equation and boundary conditions

We write the massless wave equation

$$\nabla_a \nabla^a \phi = 0$$

in a $3+1$ form similar to the ADM form of the Einstein equations by defining

$$\Pi \equiv -\mathcal{L}_n \phi = -n^a \nabla_n \phi, \tag{6.2}$$

where $n_a$ is the future-pointing unit normal on the slices of constant $t$. With $t^a \equiv (\partial/\partial t)^a \equiv \alpha n^a + \beta^a$ this gives

$$\mathcal{L}_t \phi = \mathcal{L}_\beta \phi - \alpha \Pi, \tag{6.3}$$

$$\mathcal{L}_t \Pi = \mathcal{L}_\beta \Pi - \alpha D_a D^a \phi - \alpha a^b D_b \phi + \alpha K \Pi. \tag{6.4}$$

Here $D_a$ is the covariant derivative associated with the three-metric $\gamma_{ab}$ on each slice, and $a^b = D^b \ln \alpha$ is the acceleration of the $n^a$ observers.

At the outer boundary we impose maximally dissipative boundary conditions corresponding to no incoming radiation [4],

$$\Pi - m^a D_a \phi = 0, \tag{6.5}$$

where $m^a$ is the outward-pointing unit vector normal to the boundary within each constant $t$ slice. Following [40], we discretise this to 2nd-order accuracy as

$$\Pi_N - \sqrt{g^{rr}} D_0 \phi_N = 0, \tag{6.6}$$

$$h^3 D_-^3 \Pi_{N+1} = 0, \tag{6.7}$$

where $N$ is the grid point at $r = r_{\max}$ and $N+1$ is a ghost point. For 4-th order accuracy we use

$$\Pi_N - \sqrt{g^{rr}} D^{(1)} \phi_N = 0 \tag{6.8}$$

$$h^5 D_+^5 \phi_{N+2} = 0 \tag{6.9}$$

$$h^4 D_+^4 \Pi_{N+1} = 0 \tag{6.10}$$

$$h^4 D_+^4 \Pi_{N+2} = 0 \tag{6.11}$$

where $D^{(1)}$ is defined by

$$D^{(1)} \equiv D_0 \left( 1 - \frac{h^2}{6} D_+ D_- \right). \tag{6.12}$$

At the black hole-excision boundary, or where the outer boundary is null or space-like, no boundary conditions are required for the continuum equations. As numerical boundary conditions we then use extrapolation for all ghost points including $\phi_{N+1}$, that is

$$h^5 D_+^5 \phi_{N+1} = 0 \tag{6.13}$$

in the 4-th order accurate case, and $D_+^3$ in the 2nd-order accurate case.

Our artificial dissipation operators are $-\sigma h^3 (D_+ D_-)^2$ at 2nd-order accuracy and $\sigma h^5 (D_+ D_-)^3$ at 4-th order. We use extrapolation to populate the additional ghost points required at boundaries.

### 6.2.2 Numerical boundary reflections

**2nd-order accurate code** With MDBC's (Sect. 6.2.1) high-frequency reflections occur as the wave profile leaves the grid, and these break pointwise convergence near the boundary as soon as the outgoing pulse has reached the boundary.

Since the incoming coordinate speeds are close to zero near the boundary these reflections propagate over the grid very slowly. For $n \leq 1$ and using artificial dissipation, convergence in $L^2$ is maintained even when pointwise convergence is lost near the boundary. For $n > 1$ on the other hand, the error near the boundary can become very large. As we have mentioned already, the spurious reflections converge away with resolution, leaving a continuum reflection.

For $n > 1$ slicing, we can take the outer boundary to $\mathscr{I}^+$. Although this is an outflow boundary, we cannot implement outflow boundary conditions because the coefficients of the wave equation become singular at the boundary point. However, we can impose $\phi = \Pi = 0$ at $\mathscr{I}$, and for the 2nd-order accurate code no further boundary treatment is required. This approach does not solve the problem with reflections but does prevent the extreme growth of error we see at low resolution with MDBC. In this case artificial dissipation prevents reflections on $1 < n \lesssim 1.3$ and $n = 2$ slices. It is unclear why it does not help for other values of $n$.

**4th-order accurate code** Using MDBCs at finite $R$ with a 4th-order accurate code, we also lose convergence after the outgoing wave reaches the boundary.

When taking $n > 1$ slices to $\mathscr{I}$, we have tried three ways of dealing with the grid point just inside the boundary, where we cannot use a standard 4th-order stencil. In flat spacetime, we can impose the exact solution at that point (but in general, there is no exact solution). Alternatively, we can use a 2nd-order accurate centered stencil at that point. Finally, we can use an off-center 2nd-order accurate stencil. With all three methods, convergence is lost soon after the outgoing wave reaches the boundary, even with numerical dissipation.

### 6.2.3 Accuracy results

In the following we shall *avoid* the problem of numerical reflection at the outer boundary by considering results only up to the point where the outgoing wave

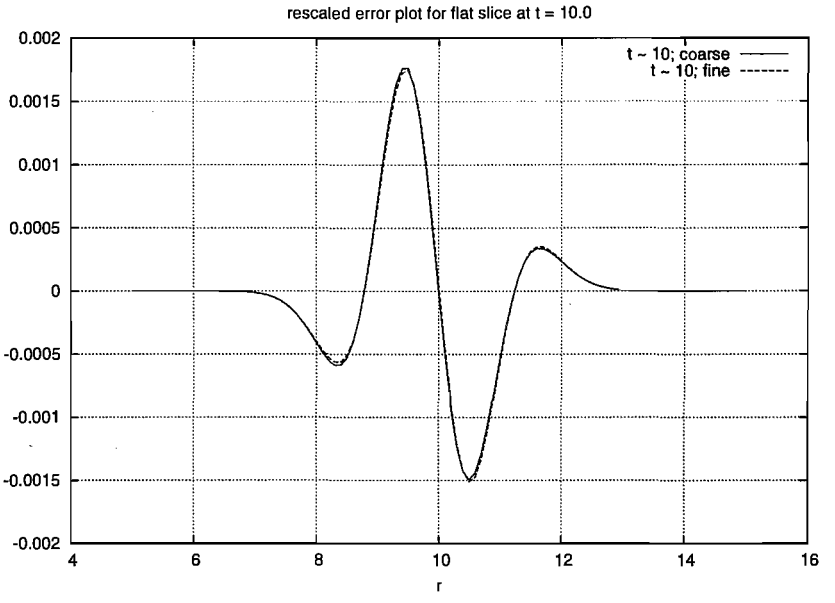


Figure 6.1: The error in $\phi$ for flat slicing at $R_* = 10$. $e(t, r_*)$ at $\Delta r = 0.1$ and $4e(r, t_*)$ at $\Delta r = 0.05$ are both plotted, but are indistinguishable here.

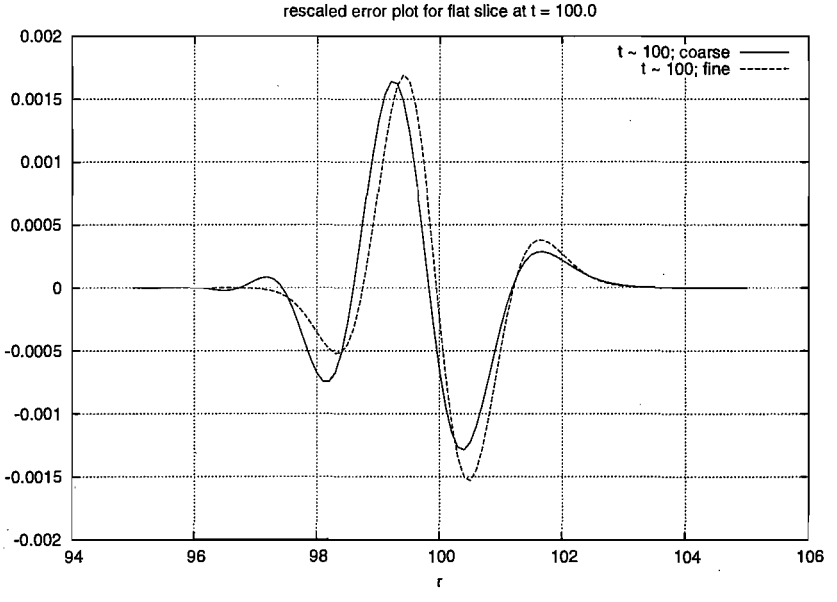


Figure 6.2: Error in $\phi$ for flat slicing at $R_* = 100$.

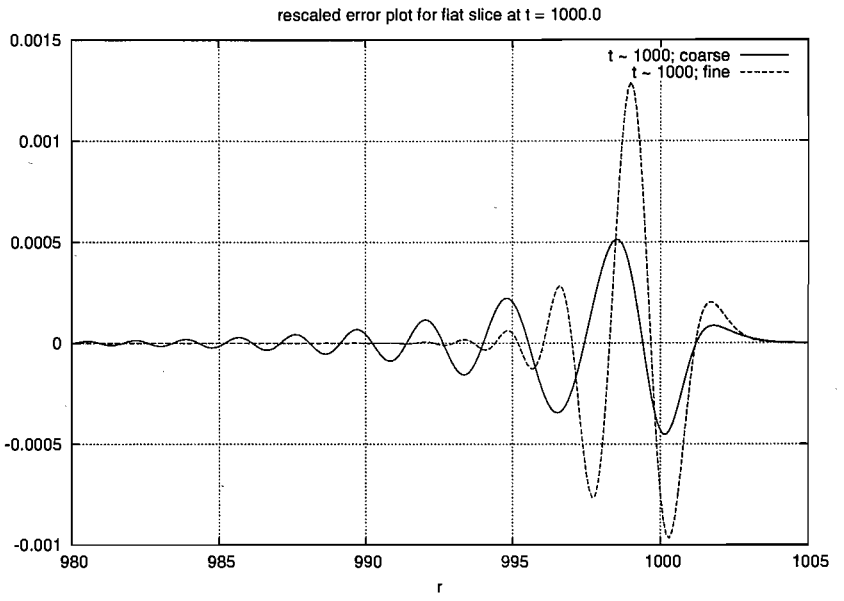


Figure 6.3: Error in $\phi$ for flat slicing at $R_* = 1000$.

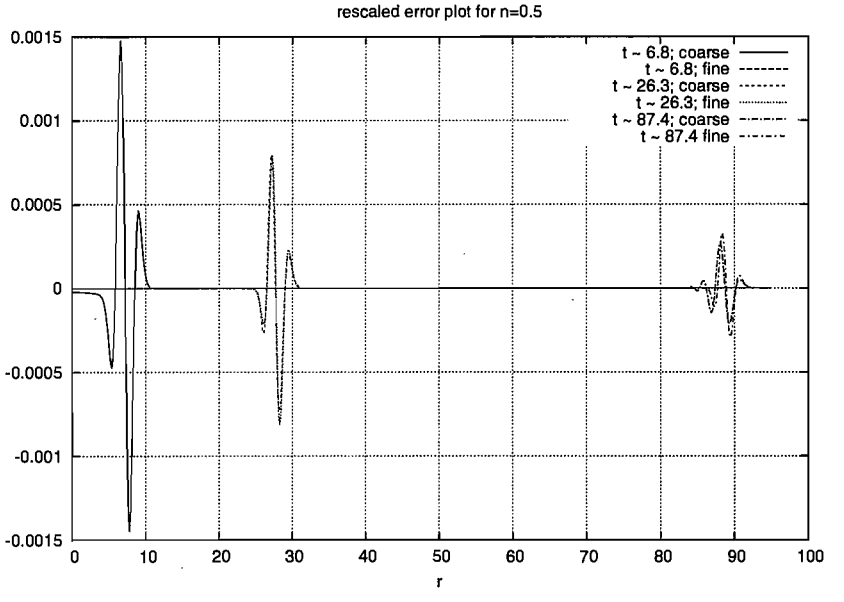


Figure 6.4: Error in $\phi$ with $n = \frac{1}{2}$ and $L = 2.0$. The three coordinate times correspond to $R_* = 10, 100, 1000$ here and in the following plots.

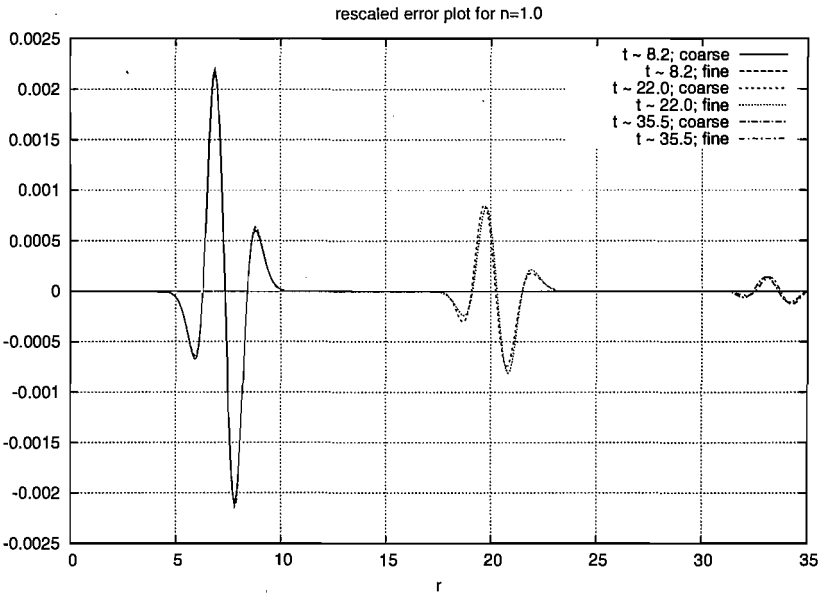


Figure 6.5: Error in $\phi$ with $n = 1$ and $L = 5.77$.

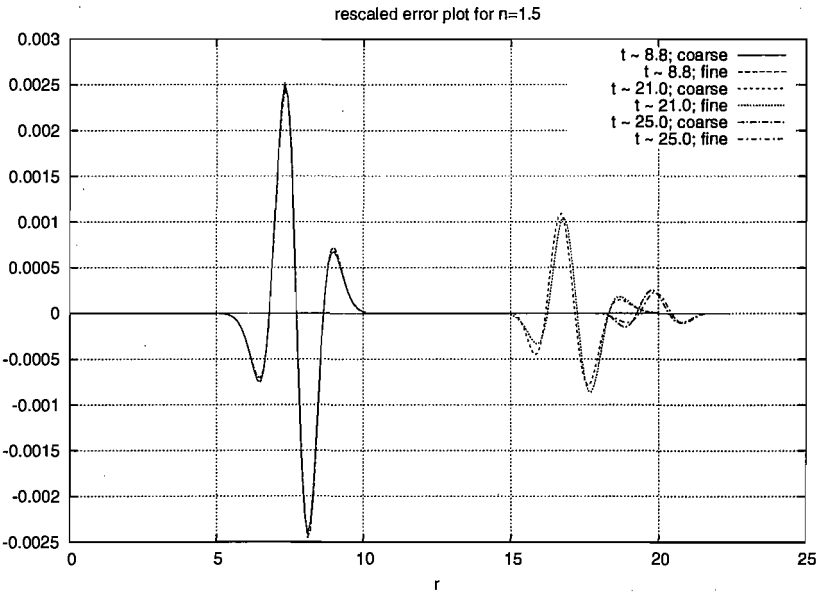


Figure 6.6: Error in $\phi$ with $n = \frac{3}{2}$ and $L = 8.9$.

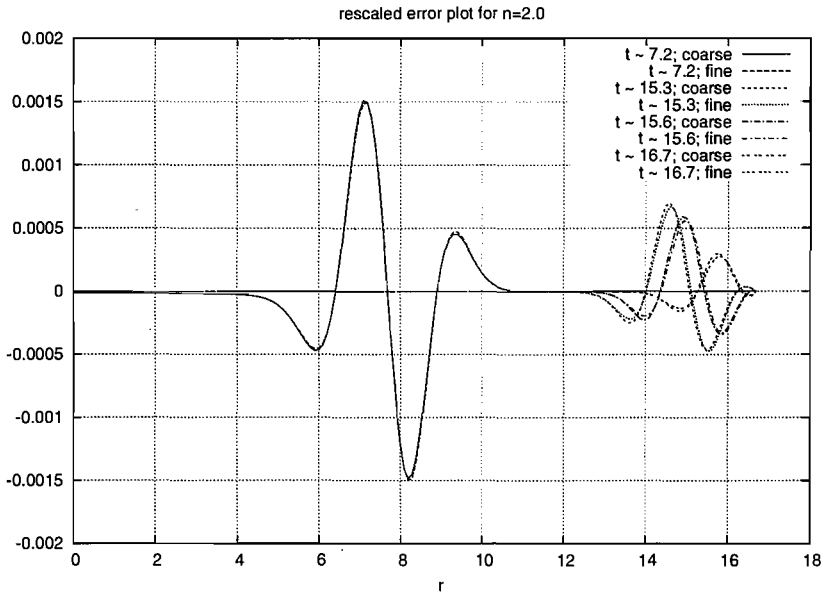


Figure 6.7: Error in $\phi$ with $n = 2$ and $L = 11.8$. The final coordinate time corresponds to $R_* = \infty$, at which the solution is still 2nd order accurate and remains so until late times, when error induced at the boundary directly after $R_* = \infty$ propagates to the central region.

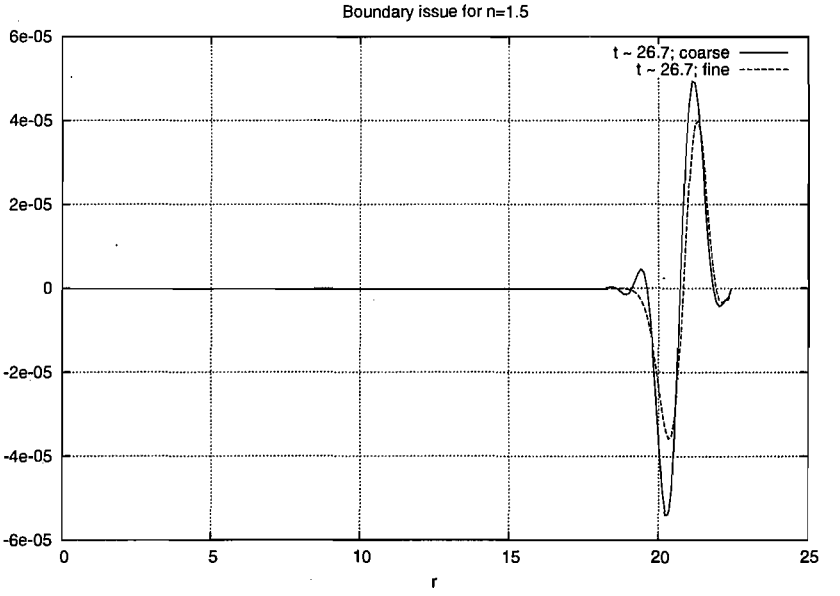


Figure 6.8: Rescaled error plot in $\phi$ with $n = \frac{3}{2}$ and $L = 8.9$ at $R_* = \infty$.

reaches the outer boundary. Then solutions for all $n$ are 2nd or 4th order accurate for appropriate schemes. Therefore the slicings should be judged by the relative number of grid points required to get out to a large physical radius and the size of relative or exact error induced on the slice. These results are summarized in Table 6.1. The results for the $n \leq 1$ slices have been obtained with MDBCs at $R \gtrsim 1000$, and the results for the $n > 1$ slices have been obtained by imposing $\phi = \Pi = 0$ at $\mathscr{I}$ and, in 4th-order accuracy, the exact solution at the grid point just inside the boundary. We plot $e(r, t_*)$ for the 2nd order accurate schemes, and tabulate the $L^2$ norm of $e(r, t_*)$ for both 2nd and 4th order accurate schemes.

On $n = 0$ slices, the error becomes large enough for the rescaled errors no longer to coincide. This appears to be due mostly to phase error (Figs. 6.1-6.3). 4th-order accurate runs do not suffer severely from this problem, but by $R_* = 1000$ it is apparent.

For the $n = \frac{1}{2}$ slicing with 2nd order accuracy the phase velocity problem we saw for the flat slice is beginning to appear as the wave reaches $R_* = 1000$ (Fig. 6.4) but it is not nearly as prominent as with $n = 0$, and with 4th-order accuracy is not apparent.

In terms of grid points compactified ($n > 1$) slices clearly have a major advantage, whilst higher values of $n \leq 1$ are to be preferred. For large $R_{\max}$ the fraction of grid points required compared to a flat slice with the same resolution near the origin is approximately $1/(1-n)(R_{\max}/L)^{-n}$ for $n < 1$ and $L/R_{\max} \ln(R_{\max})$ for $n = 1$. For $n = 1$ slices, adding a fixed number of grid points to the end of the original domain extends the physical radius R by a fixed factor without losing accuracy in the original domain.

When it comes to considering relative error we see a different picture. Because of the $R^{-1}$ dependence in the exact solution, for a constant relative error over the run we would like to see a factor of 10 in the sizes of error between $R_* = 10$, and $R_* = 100$ plots, and another factor of 10 between those for $R_* = 100$ and

$R_* = 1000$. Considering Figs. 6.4, 6.5, 6.6 and 6.7, we observe that although the absolute error on each of the slices decreases as the pulse travels outwards, the relative error increases. However, the ratio of the errors at $R_* = 1000$ and $R_* = 10$ is smallest for $n = 1$, indicating that for this slicing the error increases least rapidly as the wave goes out.

To summarize, on flat slices phase error builds up over the large $t$ interval the wave takes to reach the outer boundary whereas evolutions on asymptotically null slices typically do not have this problem. It is not clear which value of $n > 0$ one should use, and it may not matter very much for this type of situation. All values $n > 0$ allow us to use many fewer grid points to obtain a given accuracy in a typical setting than $n = 0$ requires. On $n = 1$ slices the relative error increases most slowly with $R$ as the wave goes out, but higher values of $n$ have the advantage that they require even fewer grid points.

| Slice | Grid points $R_{\max} = 1000$ | Grid points $R_{\max} = \mathscr{I}^+$ | time steps $R_* = 1000$ | time steps $R_* = \infty$ | e 2nd $R_* = 10$ | e 2nd $R_* = 100$ | e 2nd $R_* = 1000$ | e 4th $R_* = 10$ | e 4th $R_* = 100$ | e 4th $R_* = 1000$ |
|---|---|---|---|---|---|---|---|---|---|---|
| $n = 0$ | 10000 | $\infty$ | 25000 | $\infty$ | $1.8\text{x}10^{-3}$ | $1.7\text{x}10^{-3}$ | $5.0\text{x}10^{-4}$ | $2.0\text{x}10^{-5}$ | $1.9\text{x}10^{-5}$ | $1.9\text{x}10^{-5}$ |
| $n = \frac{1}{2}$ | 893 | $\infty$ | 2300 | $\infty$ | $1.5\text{x}10^{-3}$ | $7.5\text{x}10^{-4}$ | $2.5\text{x}10^{-4}$ | $1.7\text{x}10^{-5}$ | $1.2\text{x}10^{-5}$ | $4.5\text{x}10^{-6}$ |
| $n = 1$ | 338 | $\infty$ | 1000 | $\infty$ | $2.3\text{x}10^{-3}$ | $8.0\text{x}10^{-4}$ | $1.5\text{x}10^{-4}$ | $3.2\text{x}10^{-5}$ | $1.3\text{x}10^{-5}$ | $2.0\text{x}10^{-6}$ |
| $n = \frac{3}{2}$ | 207 | 224 | 624 | 667 | $2.5\text{x}10^{-3}$ | $1.1\text{x}10^{-3}$ | $2.5\text{x}10^{-4}$ | $2.3\text{x}10^{-5}$ | $2.4\text{x}10^{-5}$ | $4.8\text{x}10^{-6}$ |
| $n = 2$ | 165 | 167 | 390 | 418 | $1.5\text{x}10^{-3}$ | $6.0\text{x}10^{-4}$ | $5.0\text{x}10^{-4}$ | $1.8\text{x}10^{-5}$ | $1.0\text{x}10^{-5}$ | $4.0\text{x}10^{-6}$ |

Table 6.1: Computational costs and errors for different slicings.

## 6.3 Spherical wave equation on Schwarzschild spacetime

Fields in a curved asymptotically flat spacetime generically decay with power law tails because of backscatter [38]. In order to see how well our coordinates can cope with such small physical effects at large physical radii, we evolve the spherical wave equation on the Schwarzschild background with horizon penetrating asymptotically null slices as described in Sect. 5.2.5. A priori it is not clear if tails will be represented correctly or not: on the one hand they are caused by backscattered ingoing waves, on the other hand their frequency in advanced time $V$ is low. We set $m = 1$, that is, the wavelength of the wave we evolve is similar to the Schwarzschild radius.

### 6.3.1 Algorithm

The numerical algorithm is the same as for our Minkowski experiments, except for the boundaries. The regular origin is replaced by an outflow (excision) boundary inside the black hole. We do not see large errors or any sign of instability associated with the excision boundary. On all slices we place the outer boundary at $R_{max} \gtrsim 1000m$, which has been turned into an outflow boundary by slightly increasing the magnitude of the shift near the boundary. We also use outflow boundary conditions without adjusting the shift, and MDBCs. We plot results obtained with MDBCs, and tabulate results with all three BCs.

### 6.3.2 Tail results

Pointwise convergence properties on Kerr-Schild asymptotically null slices are comparable to Minkowski space, and the values for computational costs are similar to those given in Table 6.1. Therefore we concentrate on power law tails. To check

for tails, we plot $\phi(t)$ for "observers" at $R = 10m$ and $R = 500m$, on Kerr-Schild asymptotically null slices, using the 4th-order accurate scheme, and the artificial dissipation parameter $\sigma = 0.007$.

Figs. 6.9-6.16 show that we see power-law tails clearly until they are affected by numerical error from the boundary. From a continuum point of view, we expect an inconsistent or physically wrong boundary condition to contaminate the solution for a given observer at the earliest when the observer leaves the domain of dependence of the initial data ($t_d$), and at the latest when the outgoing wave has reached the boundary and the unphysical continuum reflection has reached the observer ($t_r$). With a given finite differencing scheme, the contamination can arrive much sooner as numerical error can propagate faster than light. Given that the power-law tail decreases rapidly with time, the time at which it is dominated by *numerical* error from the boundary depends on the amplitude of that error, and this in turn depends on the resolution, the boundary and interior finite differencing scheme, and in particular artificial dissipation. In practice, however, little time is gained by increasing resolution, and so the results below which use typical resolutions are significant.

We define $t_l$, the time when the power-law tail is lost (for a given finite differencing scheme and resolution), as the time when the fields differ from the expected power-law tail by 5%. Table 6.2 shows the three times $t_d$, $t_r$ and $t_l$ for different slicings, the two observer positions, and different outer boundary treatments. Note that on flat slices $t_r \simeq 2t_d$, that is the time for the wave to go out to the boundary is approximately the same it takes to come back to the observer, but on asymptotically null slices $t_r \gtrsim t_d$, as the wave takes only a short coordinate time to go out.

We find that tails are observed for the longest time on $n = 0$ slices: they are clearly visible until the time $t_r$ when the *continuum* reflection from the outer boundary has come back to the observer (see the Table). Our main result is that the use of

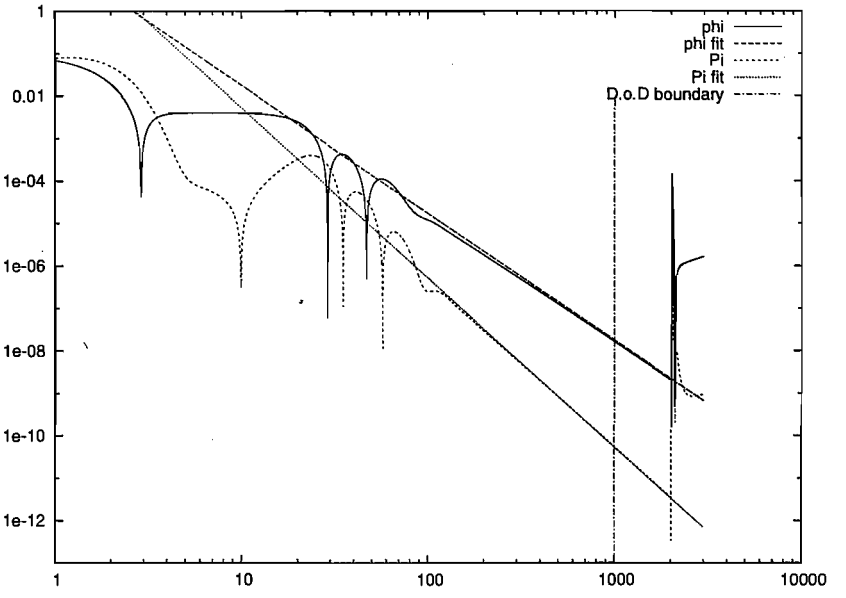


Figure 6.9: Log-log plots of $\phi(t)$ and $\Pi(t)$ at $R = 10$ on Schwarzschild spacetime with $m = 1$, using standard Kerr-Schild slices (that is $n = 0$). The straight lines are $t^{-3}$ and $t^{-4}$, the expected power-law fall-off for the tails in $\phi$ and $\pi$, with an overall constant fixed to match the numerical data. The power-law tails are clearly visible at late times, after the outgoing wave has passed the observer. They are overwhelmed by spurious continuum reflections from the boundary.

asymptotically null slices alone does not suppress power-law tails. Rather, the tails are resolved until continuum reflections from the boundary reach the observer and become larger than the physical tail field.

For $n = 1/2$ slices the results are almost as good, in particular when we take into account that for an $R = 500$ observer $T \simeq t + 500$ for $n > 0$ because the slice curves up. With $n = 1/2$, the tails are observed until they are overwhelmed by *numerical* reflections from the boundary, which travel faster than light. The $n = 1$ and $n = 3/2$ show tails at $R = 10$ for much shorter times because the spurious numerical reflection travels faster, and no tails are seen at $R = 500$. From our small sample, $n = 1/2$ seems to be the best compromise between minimizing phase error in the outgoing wave and resolving tails.

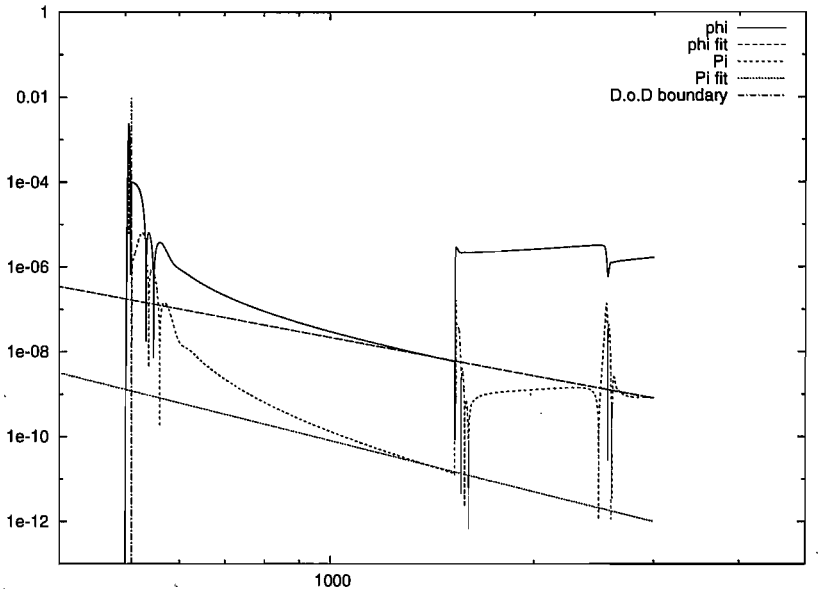


Figure 6.10: As in the previous plot, but at $R = 500$.

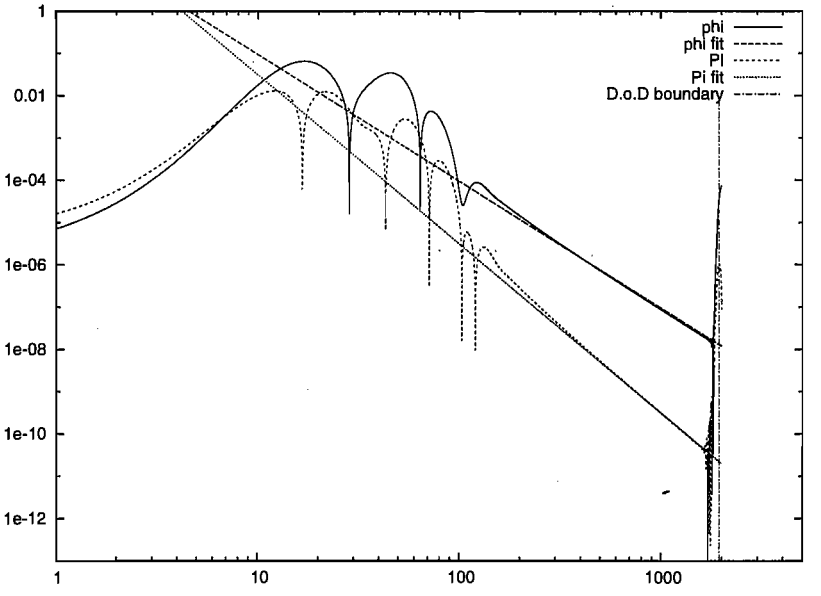


Figure 6.11: As in the previous plots, but with $n = 1/2$ slices, at $R = 10$. Here, and in all following $n > 0$ plots, the tails are overwhelmed by spurious numerical reflections from the boundary which propagate in faster than light.

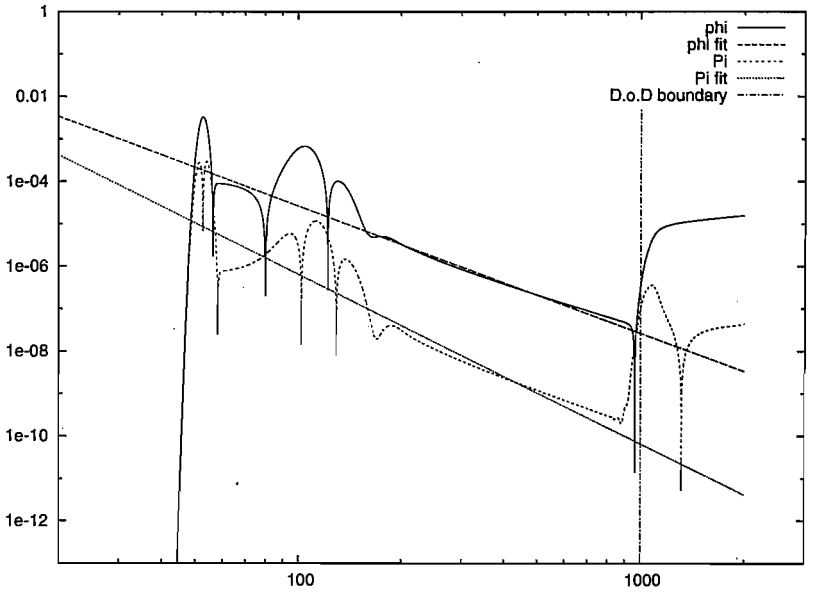


Figure 6.12: As in the previous plots, but with $n = 1/2$ slices, at $R = 500$.

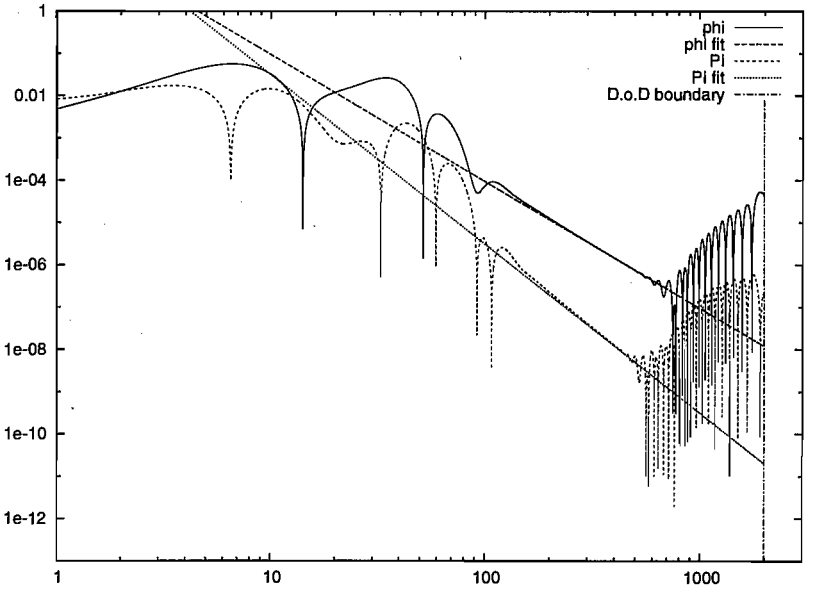


Figure 6.13: As in the previous plots, but with $n = 1$ slices, at $R = 10$.

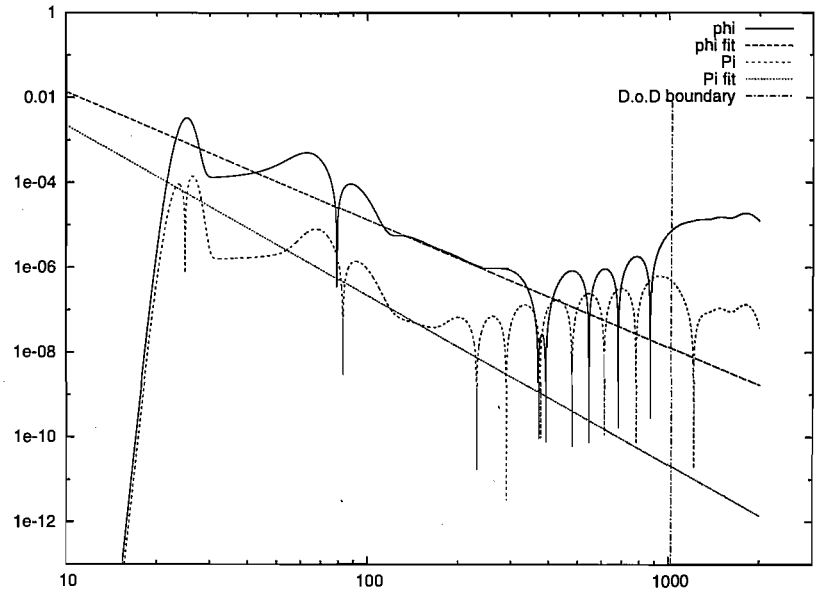


Figure 6.14: As in the previous plots, but with $n = 1$ slices, at $R = 500$.

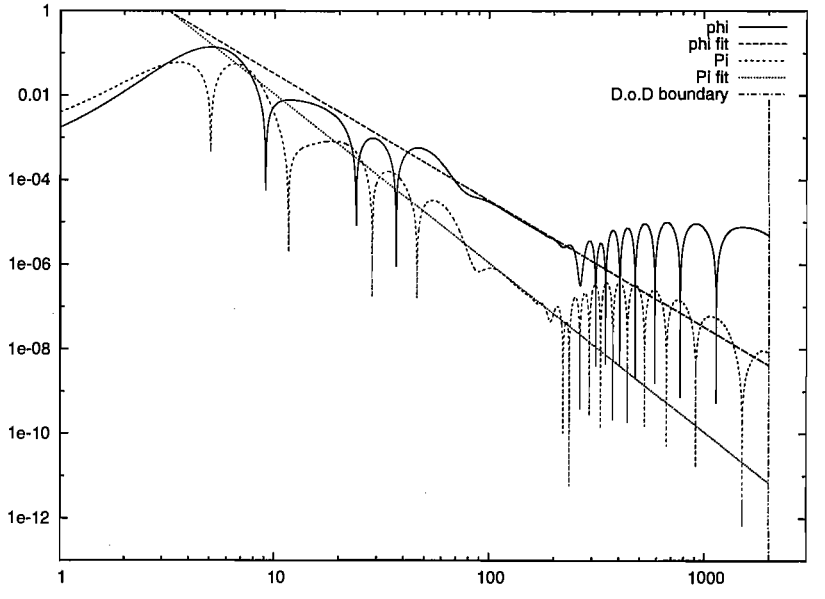


Figure 6.15: As in the previous plots, but with $n = 3/2$ slices, at $R = 10$.

| Slice | Observer $R$ | $t_d$ | $t_r$ | MDBC $t_l$ | Extrap. BC $t_l$ | Outflow BC $t_l$ |
|---|---|---|---|---|---|---|
| $n = 0$ | 10 | 1000 | 2020 | **2020** | – | – |
| | 500 | 511 | 1530 | **1530** | – | – |
| $n = \frac{1}{2}$ | 10 | 1940 | 2017 | 1340 | 1850 | **1700** |
| | 500 | 999 | 1080 | 626 | 1090 | **889** |
| $n = 1$ | 10 | 1990 | 2020 | 459 | 1960 | **561** |
| | 500 | 1020 | 1050 | * | 513 | **181** |
| $n = \frac{3}{2}$ | 10 | 2000 | 2030 | 180 | 925 | **221** |
| | 500 | 1030 | 1050 | * | 181 | * |

Table 6.2: $t_d$ (time when the observer leaves the domain of dependence), $t_r$ (time when the reflection of the outgoing wave from the boundary reaches the observer) and $t_l$ (time when the tails are lost) for different slicings and two observer locations. Note that $T = t + \text{const}$ for these observers at fixed $R$, where the constant depends on $R$ and the slicing. "–" means this BC was not implemented. "*" means with this BC tails were not seen. The figures in boldface correspond to the figures.

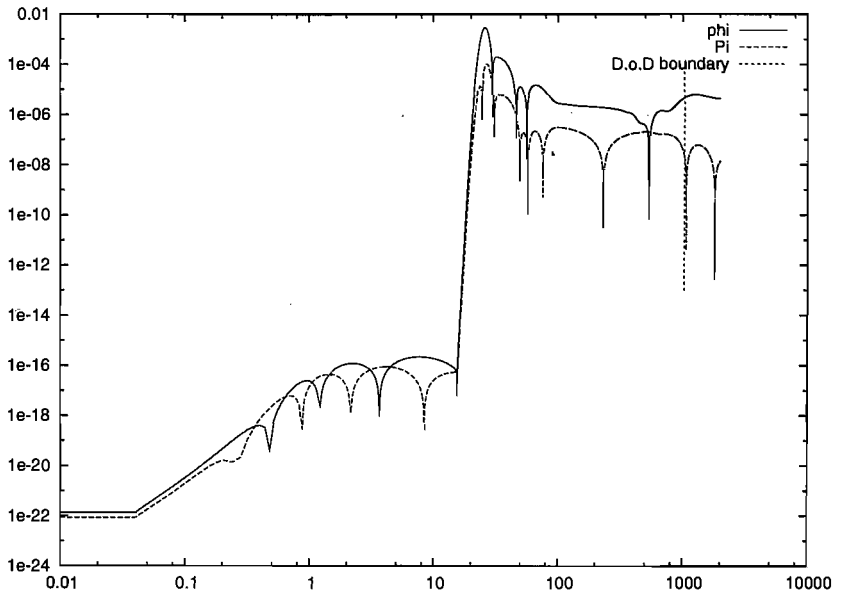


Figure 6.16: As in the previous plots, but with $n = 3/2$ slices, at $R = 500$.

## 6.4 Conclusions

The use of asymptotically null slices in numerical relativity is not a new idea. It is already well-established as an essential ingredient of the conformal field equations approach. The essential motivation for using either the conformal field equations or null coordinates is their ability to simulate an asymptotically spacetime out to future null infinity on a finite numerical grid. However, this can be done with any accuracy only if ingoing radiation (including backscattered waves) can be progressively neglected at large radius.

Conversely, in any physical situation where these approaches do work accurately, one should be able to simulate the spacetime almost up to future null infinity by using asymptotically null slices without going to the trouble of regularizing the field equations at infinity itself [35, 39] (this idea has probably been discovered independently more than once, but we are not aware of other publications).

The main advantage of our approach compared with Cauchy-characteristic match-

ing or the conformal field equations is its relative simplicity: in principle only the initial data and the gauge conditions need to be modified, not the evolution code or its boundary conditions. The main disadvantage is that boundary conditions are still required in principle. One may however be able to work on the domain of dependence and use outflow boundary conditions.

Restricting to the spherical wave equation on Minkowski and Schwarzschild, we have re-examined these ideas carefully. From the requirements that the outgoing coordinate speed of light should neither go to zero (the code becomes inefficient and too dissipative) nor to infinity (explicit schemes become unstable, and implicit schemes are likely to produce large errors), we have established a quantitative relationship between the rate at which the slices become null at large radius and the rate at which the radial coordinate is compactified.

This rate can be parametrized by a parameter $n$, where on the one hand, the physical radius (area radius) $R$ and coordinate radius $r$ are asymptotically related by $r \sim R^{1-n}$, and on the other hand the Lorentz factor of the slices asymptotically diverges as $\Gamma \sim R^{n/2}$ and the extrinsic curvature of the slices scales as $K \sim R^{n/2-1}$. The CFL condition in the tangential direction gives $n \leq 2$.

The value $n = 0$ corresponds to the standard slices, while $n = 2$ corresponds to the hyperboloidal slices which have traditionally been used both in drawing the standard conformal diagram of Minkowski or Schwarzschild spacetime, and in numerical evolutions in null coordinates or using the conformal field equations.

As our first new result, we have shown that milder compactifications with $0 < n < 2$ are also possible. We find two different regimes: For $0 < n \leq 1$ the range of the coordinate $r$ is infinite (we prefer to speak of stretching rather than of compactification) and surprisingly the slices end at spacelike infinity. For $1 < n \leq 2$ the range of $r$ is finite and the slices intersect future null infinity as expected. To our knowledge, only the case $n = 2$ has been considered before.

Our numerical simulations of the spherical wave equation on Minkowski and Schwarzschild

spacetimes have confirmed our expectations based on the asymptotic analysis. For a given (very large) radius of the outer boundary and a given required accuracy as the outgoing wave reaches that boundary, simulations in our $n > 0$ coordinates require dramatically fewer grid points and fewer time steps.

To compare two extreme examples, in order to evolve an outgoing wave with wavelength $\Delta R \sim 1$ out to $R = 10000$ with a relative error of 20% (mostly phase error), 10000 gridpoints and 25000 time steps are required in standard coordinates using 4th-order finite differencing, while only 165 grid points and 390 times steps with our $n = 2$ coordinates give a relative error of only 4%. (The saving in time steps is significant only in this somewhat artificial situation where the spacetime region of interest is a thickened light cone. The saving in grid points, however, would be significant in any simulation.)

Another important result was not necessarily expected: although $n > 0$ coordinates do not represent ingoing waves, for example backscattered waves, accurately, power-law tails of waves on Schwarzschild are correctly represented. This may be because they are effectively low frequency. We note, however, that lower values of $n$ represent the tails correctly for longer time because numerical error from the boundary propagates in less rapidly. This suggests that in applications to numerical relativity all values of $n > 0$, not just $n = 2$, should be considered. The computational cost is similar. To return to the example above, the numerical cost with $n = 1$ is 338 grid points and 1000 time steps for an error 2%.

A second unexpected result of the numerical experiments is that simulations are numerically much more accurate if outflow boundary conditions rather than maximally dissipative boundary conditions can be imposed. Here, we have made this possible by slightly increasing the shift near the boundary, which means that the resulting spacetime no longer obeys the vacuum Einstein equations. A more physically consistent approach in full GR would be adding a small cosmological constant to the Einstein equations [61], and placing the outer boundary just outside the re-

sulting de Sitter cosmological horizon. Alternatively, one could modify the slicing and/or the spatial coordinates so that the outer boundary becomes truly spacelike or null, at the price that the coordinates are no longer compatible with the Killing vector $\partial/\partial T$.

# Chapter 7

# Pure gauge evolutions on asymptotically null slices

The work that follows is that of the author, except for parts of Sect. 7.1.1, which were written by C Gundlach.

In this Chapter the pure gauge evolution system is introduced and the hyperbolicity of several gauges in spherical symmetry are analyzed. Finally asymptotically null coordinates are evolved numerically.

## 7.1 The pure gauge system

### 7.1.1 Equations

Naive numerical evolutions of asymptotically null initial data with the full Einstein equations suffer from large errors; the code crashes. The aim of the work in this chapter is to discover why. It is difficult to study the behavior of different gauge conditions when evolving the full Einstein equations. The presence of constraints makes it hard to discern which effects are caused purely by gauge and which

are caused by constraint violation. One way around this is to evolve coordinates $(t, x^i)$ on a spacetime given in coordinates $X^\mu$ with metric $g_{\mu\nu}$ according to gauge conditions of interest. In terms of the lapse and shift,

$$\dot{X}^\mu = \alpha n^\mu + \beta^i X^\mu_{,i}, \tag{7.1}$$

where $n^\mu$ are the $X^\mu$ components of the unit normal to the $t$-slices. The 3-metric is given by

$$\gamma_{ij} = g_{\mu\nu} X^\mu_{,i} X^\nu_{,j}, \tag{7.2}$$

and $\dot{\gamma}_{ij} = \mathcal{L}_\beta \gamma_{ij} - 2\alpha K_{ij}$ gives

$$\begin{aligned} K_{ij} &= X^\mu{}_{,ij} n^\nu g_{\mu\nu} + \frac{1}{2}\Big( X^\mu{}_{,i} X^\lambda{}_{,j} n^\nu \\ &\quad + X^\lambda{}_{,i} X^\nu{}_{,j} n^\mu - X^\mu{}_{,i} X^\nu{}_{,j} n^\lambda \Big) g_{\mu\nu,\lambda}, \end{aligned} \tag{7.3}$$

where the unit normal $n^\mu$ is given, up to normalization, by

$$n^\mu \propto g^{\mu\nu} \epsilon_{\nu\alpha\beta\gamma} X^\alpha{}_{,1} X^\beta{}_{,2} X^\gamma{}_{,3}. \tag{7.4}$$

In spherical symmetry $n_a$ is defined by $(\partial/\partial r)^a n_a = 0$, and in preferred coordinates $(T, R)$

$$n_T = -\frac{R'}{\sqrt{\gamma_{rr}}}, \quad n_R = \frac{T'}{\sqrt{\gamma_{rr}}}. \tag{7.5}$$

The full evolution equations for $R$ and $T$ in this context are (with the background coordinate $R$ the areal radius)

$$\dot{R} = \beta^r R' - \frac{\alpha}{\sqrt{\gamma_{rr}}}\Big( g_{TR} R' + g_{TT} T' \Big), \tag{7.6}$$

$$\dot{T} = \beta^r T' + \frac{\alpha}{\sqrt{\gamma_{rr}}}\Big( g_{RR} R' + g_{TR} T' \Big). \tag{7.7}$$

### 7.1.2 Hyperbolicity of the pure gauge system

The spherical gauge evolution system is not quasilinear, because the equations for $\dot{R}$ and $\dot{T}$ are nonlinear in $R'$ and $T'$. Hence in order to analyze the hyperbolicity of the system one must explicitly linearize and apply weights to equations and

variables (see Chap. 2). The principal part of the evolution of the coordinates is then

$$\begin{aligned}
\dot{\delta T} &\simeq \left(\beta + \frac{\alpha}{\sqrt{\gamma}}\left(g_{TR} + n^R n^T\right)\right)\delta T' \\
&\quad + \frac{\alpha}{\sqrt{\gamma}}\left(g_{RR} - (n^T)^2\right)\delta R' + n^T\delta\alpha + T'\delta\beta, \qquad (7.8)\\
\dot{\delta R} &\simeq \frac{\alpha}{\sqrt{\gamma}}\left(g_{TT} + (n^R)^2\right)\delta T' \\
&\quad + \left(\beta + \frac{\alpha}{\sqrt{\gamma}}\left(g_{TR} + n^R n^T\right)\right)\delta R' \\
&\quad + n^R\delta\alpha + T'\delta\beta. \qquad (7.9)
\end{aligned}$$

For BMn (4.89) slicing with ft shift driver (4.95), this is completed by

$$\dot{\delta\alpha} \simeq \frac{\alpha^2\mu_L}{\gamma}(n_R\delta T'' + n_T\delta R'') + \beta\delta\alpha', \qquad (7.10)$$

$$\dot{\delta\beta} \simeq -\frac{\alpha^2(2-\rho)\mu_S}{\gamma^{3/2}}(n^R\delta T'' + n^T\delta R''). \qquad (7.11)$$

The system is diagonalizable with real characteristic speeds $dr/dt$

$$-\beta \pm \tfrac{\sqrt{\mu_L}}{\sqrt{\gamma}}\alpha, \qquad (7.12)$$

$$\tfrac{1}{2}\left(\beta \pm \sqrt{\beta^2 + \tfrac{4\mu_S\alpha^2(2-\rho)}{\gamma}}\right), \qquad (7.13)$$

and so is strongly hyperbolic.

The principal part of BMn with the fn shift driver (4.94) is the same except that $\dot{\delta\beta} = \cdots + \beta\delta\beta'$. This system is also strongly hyperbolic with characteristic speeds

$$-\beta \pm \tfrac{\sqrt{\mu_L}}{\sqrt{\gamma}}\alpha, \qquad (7.14)$$

$$-\beta \pm \tfrac{\sqrt{\mu_S}\sqrt{2-\rho}}{\sqrt{\gamma}}\alpha. \qquad (7.15)$$

For BMn with area locking shift (4.88) the principal part becomes

$$\dot{\delta T} \simeq \beta\delta T' - \frac{1}{n_T}\delta\alpha, \qquad (7.16)$$

$$\dot{\alpha} \simeq -\frac{\alpha^2\mu_L n_T}{\gamma}\delta T'' + \beta\delta\alpha'. \qquad (7.17)$$

In this case the system is also strongly hyperbolic and has characteristic speeds (7.12).

The BMt slicing condition (4.90) gives rise to strongly hyperbolic pure gauge systems with speeds

$$\frac{1}{2}\left(\beta \pm \sqrt{\beta^2 + \frac{4\mu_L \alpha^2}{\gamma}}\right), \tag{7.18}$$

with either area locking shift, ft shift driver [adds speeds (7.13)] or fn shift driver [adds speeds (7.15)].

A simple analysis of BMg (4.91) as a pure gauge system on Minkowski spacetime shows that it is well-posed with a fixed shift (see also [41]), but is ill-posed with the fn or ft drivers. It is not considered further.

The preceding analysis shows that BMt slicing in combination with any shift condition always has both positive and negative gauge coordinate speeds. This means that on any excision surface of constant radial coordinate $r$ there will always be a gauge mode traveling towards increasing $r$, and so excision is not possible with this slicing condition unless a boundary condition is imposed on the gauge at the excision boundary. A similar result holds for the ft-driver shift condition. We will mainly use either an algebraic Killing shift (area freezing shift) or the fn driver shift.

Constructing boundary conditions for a system which is not quasilinear is a difficult task which will not be discussed here. Numerically the fields have simply been frozen at the outer boundary.

## 7.2 Evolutions on asymptotically null slices

The aim of this section is to find gauge conditions which in the absence of the constraints freeze at a desired solution, in particular on asymptotically null slices.

As discussed in Chap. 4, a family of live gauge conditions

$$\dot{\alpha} = \beta^i \alpha_{,i} - \alpha^2 \mu_L K, \tag{7.19}$$

$$\dot{\beta}^i = \alpha^2 \mu_S f^i + \beta^j \beta^i_{,j} - \eta \beta^i, \tag{7.20}$$

which include the 1+log lapse ($\mu_L = 2/\alpha$) condition and the so-called gamma-driver shift condition ($\mu_S = 1/\alpha^2$) have become standard for astrophysical simulations in numerical relativity. These conditions have proven capable of dealing with highly complicated physical scenarios.

These conditions must be modified for use with asymptotically null slices, which clearly will not freeze the gauge condition (7.19,7.20). It is desirable to find well-behaved gauge conditions which freeze at a desired solution without introducing artificial source terms, but in practice this is a very difficult task. Instead the approach here is to modify (7.19,7.20) so that they freeze appropriately. The advantage of this approach is that the modified gauge condition should inherit many of the desirable properties of the original condition. In particular, if source terms are picked so that the principal part is unaltered, the new system will inherit known well-posedness properties [17] from the unaltered system. With these considerations in mind, the gauge condition

$$\dot{\alpha} = -2\alpha(K - K_0) + \beta^j(\alpha_{,j} - (\alpha_0)_{,j}) \tag{7.21}$$

$$\dot{\beta}^i = (f^i - f^i_0) + \beta^j(\beta^i_{,j} - (\beta_0)^i_{,j}) - \eta(\beta^i - \beta^i_0) \tag{7.22}$$

is examined. As stated above we are not concerned with the outer boundary. Instead the focus is on the broad behavior of the gauge condition: does the slice kink or suffer from any undesirable growth?

The results of Chap. 6 suggest focusing on the case $n = 1$, so that initially (5.50, 5.47)

$$F(R) = \sqrt{L^2 + R^2} - L - \frac{L}{2} \ln\left(1 + \frac{R^2}{L^2}\right) + 2M \ln\left(1 + \frac{R^2}{L^2}\right), \tag{7.23}$$

$$R(r) = L \sinh \frac{r}{L}, \tag{7.24}$$

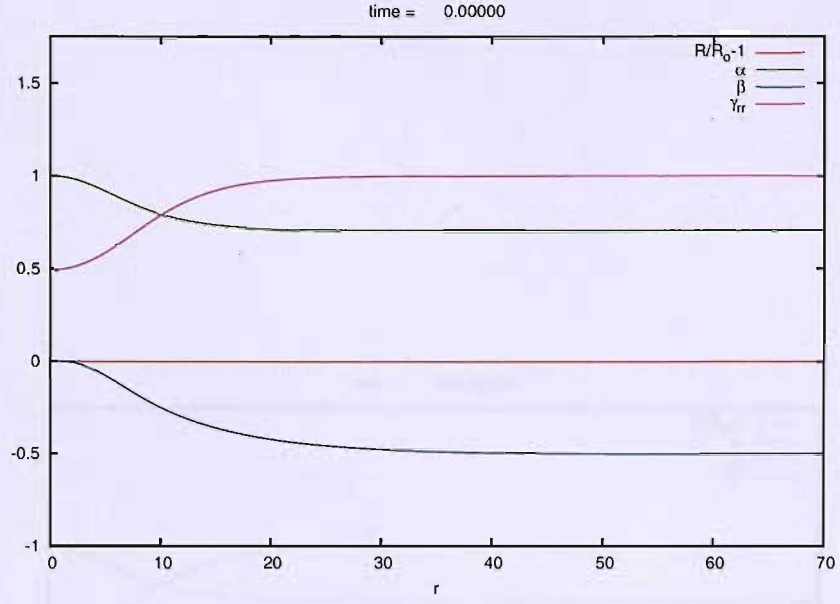


Figure 7.1: The Minkowski spacetime asymptotically null initial data (appropriately rescaled). $\gamma_{rr}$ is not an evolved variable but a derived quantity. The evolved $T$ field is not shown.

in the Schwarzschild spacetime with Kerr-Schild slices near the blackhole. Flat space is the special case $M = 0$.

**Minkowski spacetime** It is easily verified numerically that without source terms, evolving asymptotically null slices under the "1+log" gauge induces large numerical error and code crashes. Fig. 7.2 demonstrates that in the Minkowski spacetime with asymptotically null initial data, the modified lapse condition combined with area locking shift (4.88) is well-behaved, despite the slowly growing feature at the outer boundary. The following diagram (Fig. 7.3) shows similar behavior with the evolved shift condition (7.22). These simulations were carried out with a spatial resolution $h = 0.1$, second order differences in space, and an $n = 1$ slice (5.31,5.32) with an outer boundary at $R_{\max} \simeq 25000$. Convergence tests demonstrate second order pointwise accuracy away from the outer boundary. The snapshots are made at $t = 1000$ before the outer boundary causes the evolution to fail.

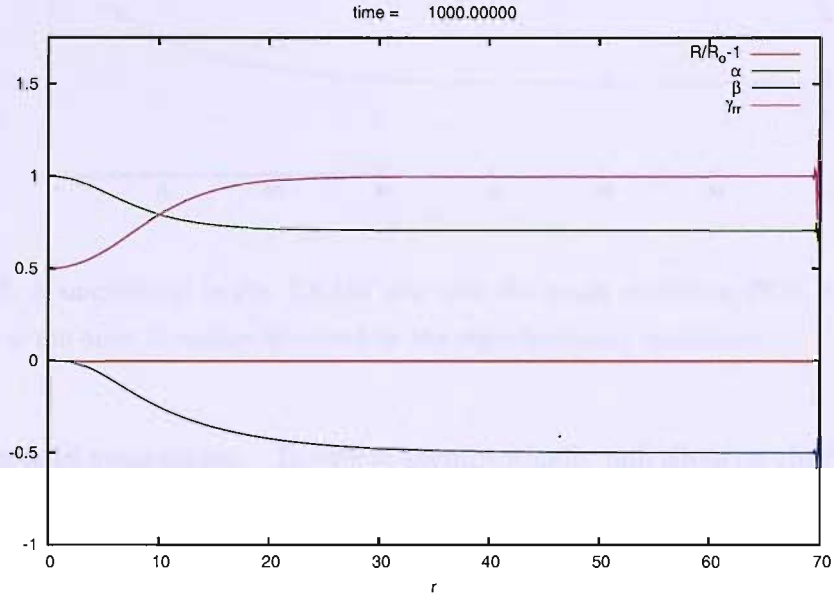


Figure 7.2: A snapshot of the evolution of asymptotically null coordinates on Minkowski spacetime at $t = 1000$. The evolution was made using the gauge condition (7.21) for the lapse and the area locking shift condition (4.88) for the shift. The feature at the outer boundary is caused by the numerical outer boundary conditions in which the evolved variables are overwritten by data from the exact solution. Eventually the feature grows large enough to prevent further evolution.

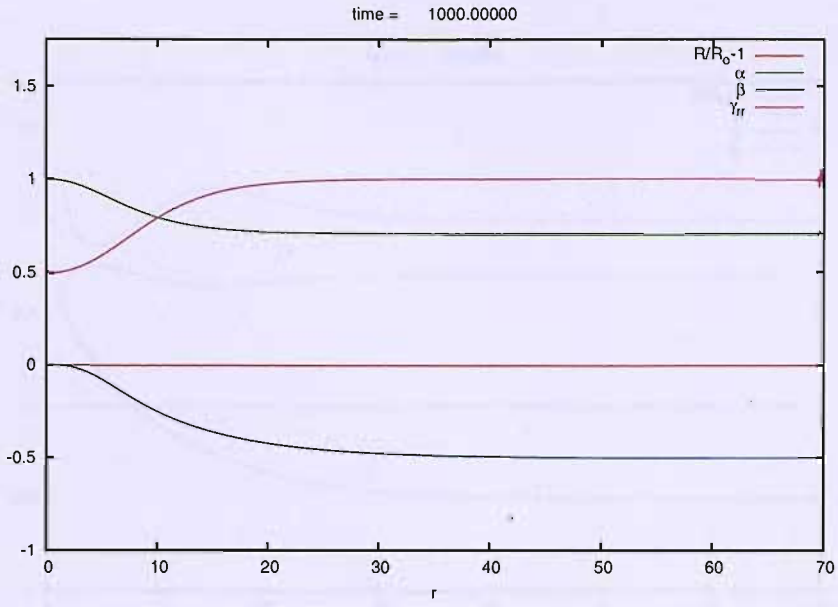


Figure 7.3: A snapshot as in Fig. 7.2 but now with the gauge conditions (7.21, 7.22). Again the feature at the outer boundary is caused by the outer boundary conditions.

**Schwarzschild spacetime** To evolve asymptotically null slices on the Schwarzschild background, coordinates are taken which go to the Kerr-Schild system near the blackhole. Again the simulation was carried out with a spatial resolution $h = 0.1$, second order differences in space, and an $n = 1$ slice with an outer boundary at $R_{\max} \simeq 25000M$. The blackhole boundary is excised at $R = 1.4M$. All fields are extrapolated to third order. Convergence tests again demonstrate second order pointwise accuracy away from the outer boundary. Figs. 7.4-7.6 Demonstrate similar behavior to the evolutions in flat space. Again the numerical outer boundary condition creates a slowly growing feature. The black hole excision boundary causes no numerical problems.

**Summary** The numerical evolutions presented in this chapter demonstrate that the modified BMn and fn-driver conditions (7.21,7.22) can be used to evolve asymptotically null initial coordinates on a fixed background.

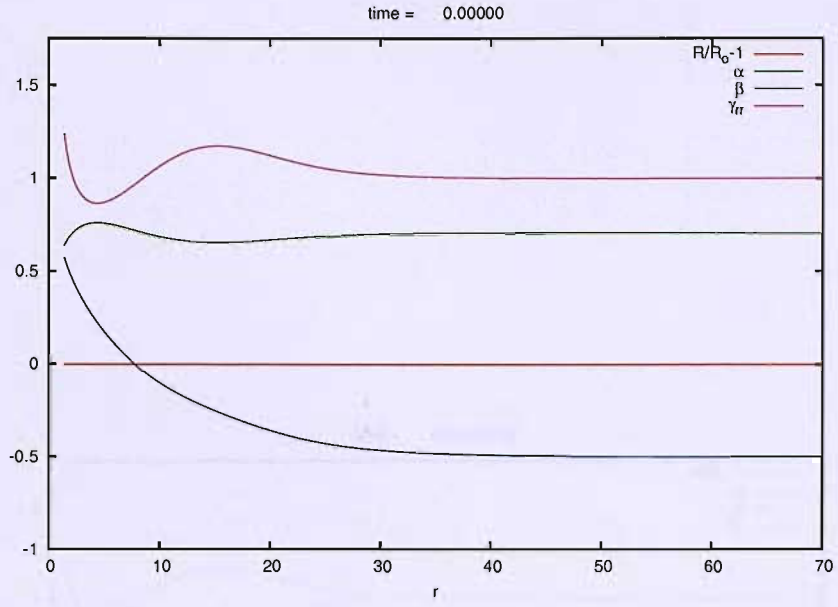


Figure 7.4: The Kerr-Schild asymptotically null slice (rescaled as in fig 7.1).

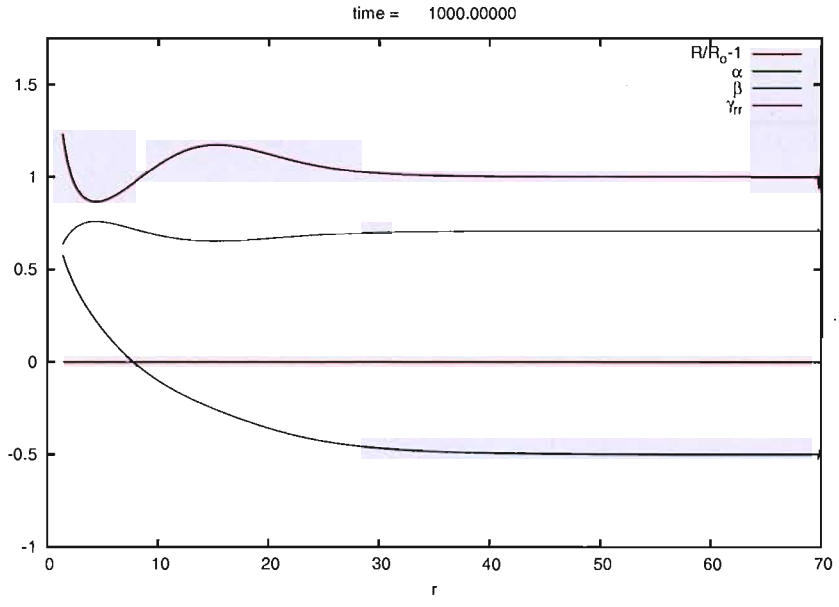


Figure 7.5: A snapshot of the evolution of the data shown in Fig. 7.4 at $t = 1000$ with (4.88,7.21).

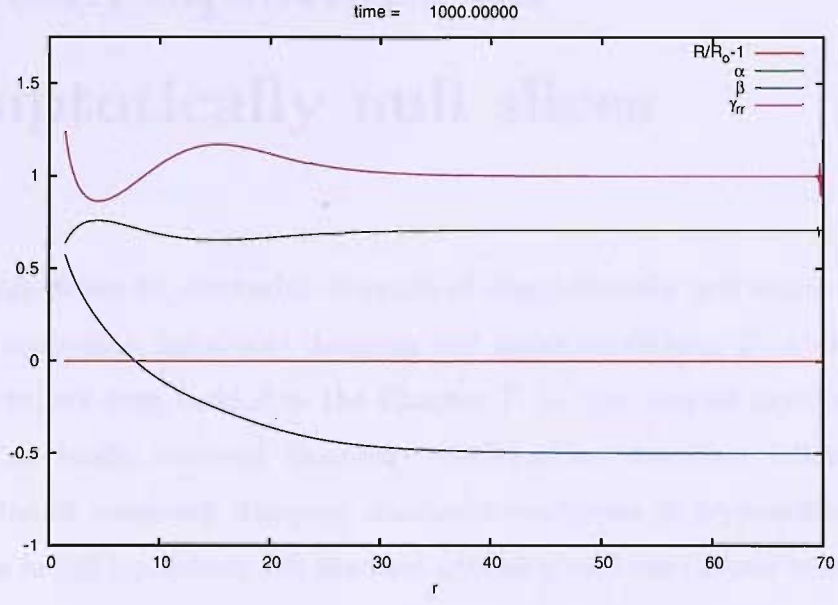


Figure 7.6: As in Fig. 7.5 with (7.21,7.22).

# Chapter 8

# Einstein equations on asymptotically null slices

The key ingredients for successful evolution of asymptotically null initial data are boundary conditions, constraint damping and gauge conditions. To some extent gauge conditions were tackled in the Chapter 7. In this chapter asymptotically null slices are briefly reviewed. Boundary conditions are described, followed by a consideration of constraint damping. Successful evolutions of asymptotically null initial data in full (spherical) GR are then presented and the chapter concludes.

## 8.1 Asymptotically null initial data

For astrophysical simulations in numerical relativity to be considered reliable the largest possible portion of spacetime ought to be evolved. For one thing, extracted wave-forms are more reliable if they are extracted far from the strong field region. In addition spurious radiation caused by imperfect boundary conditions will not swamp outgoing gravitational waves or affect physics occurring in the central region if the boundaries are far out. The problem here is one of economy: there is a trade off between resolution in the dynamically active region and how far out the outer

boundary can be pushed. There are several approaches to the problem, which may be split into two categories, the continuum [8] and the numerical. These categories can be considered complementary since many of the numerical approaches (for example mesh refinement) may be used with a given continuum system.

In Chap. 5 asymptotically null slices were constructed in the Minkowski and Reissner-Nordström spacetimes in spherical coordinates by applying the change of coordinates (5.3,5.4)

$$t = T - F(R), \tag{8.1}$$

$$R = R(r). \tag{8.2}$$

That analysis is trivially extended to spherically symmetric asymptotically flat spacetimes by applying the same change of coordinates to a line element

$$\mathrm{d}s^2 = g_{TT}\mathrm{d}T^2 + 2g_{TR}\mathrm{d}T\mathrm{d}R + g_{RR}\mathrm{d}R^2 + R^2 d\Omega^2, \tag{8.3}$$

where $d\Omega^2 \equiv d\theta^2 + \sin^2\theta\, d\varphi^2$, adapted to asymtotic flatness so that at large area radius $g_{TT} \to 1$, $g_{TR} \to 0$ and $g_{RR} \to 1$. The metric is then rewritten in the standard way as

$$\mathrm{d}s^2 = -\alpha^2\mathrm{d}t^2 + \gamma_{rr}(\mathrm{d}r + \beta^r\mathrm{d}t)^2 + \gamma_{\theta\theta}\mathrm{d}\Omega^2 \tag{8.4}$$

The ingoing and outgoing *coordinate* light speeds $C_\pm, c_\pm$ of the coordinate systems $T, R$ and $t, r$ are related by (5.14),

$$c_\pm^{-1} = R'(C_\pm^{-1} - F'). \tag{8.5}$$

$F(R)$ and $R(r)$ can be chosen so that $R' \simeq (R/L)^n$ and $c_+(\infty) = 1$ where $0 \leq n \leq 2$. For $0 \leq n \leq 1$ the slices $F(R)$ of constant $t$ terminate at space-like infinity $i_0$ and for $1 < n \leq 2$ they terminate at future null infinity $\mathscr{I}$. The parameter $n$ determines how quickly the slices become null. At the extremes, $n = 0$ makes the slices asymptotically Minkowskian and $n = 2$ corresponds to the hyperboloidal slices considered commonly in relation to the conformal field equations

[8]. Asymptotically null slices can be constructed in any asymptotically flat spacetime (because near infinity the spacetime has the same causal structure as that given by the spherical line element (8.3)). In general (for spacetimes with matter or without symmetry) it will be necessary to solve the Hamiltonian and momentum constraints numerically such that the following requirements are satisfied. For $0 < n < 1$

$$4\alpha^2 \simeq \gamma_{rr} \sim r^{n/(1-n)}, \qquad \gamma_{\theta\theta} \sim r^{2/(1-n)} \tag{8.6}$$

$$\beta^r \simeq -1/2, \qquad K_{rr} \sim r^{(3n/2-1)/(1-n)}, \tag{8.7}$$

$$K_{\theta\theta} \sim r^{(n/2+1)/(1-n)}, \qquad K \sim r^{(n/2-1)/(1-n)}. \tag{8.8}$$

For $n > 1$ the radial coordinate compactifies the spacetime so that $\mathscr{I}$ occurs at finite $r = l$. The asymptotic growth of the $3+1$ variables is the same as that with $n < 1$, but with $r$ in (8.6-8.8) replaced with $r - l$. Finally with $n = 1$

$$4\alpha^2 \simeq \gamma_{rr} \sim e^r, \qquad \gamma_{\theta\theta} \sim e^{2r} \tag{8.9}$$

$$\beta^r \simeq -1/2, \qquad K_{rr} \sim e^{r/2}, \tag{8.10}$$

$$K_{\theta\theta} \sim e^{3r/2}, \qquad K \sim e^{-r/2}. \tag{8.11}$$

In Chap. 6 it was found that $n = 1$ induces the smallest errors at a fixed resolution when evolving the wave equation on a fixed background. Henceforth we focus exclusively on the $n = 1$ case.

## 8.2 Boundary conditions

Part of the motivation for modifying the BMn 1+log gauge by adding source terms like (7.21, 7.22) was that it left the principal part of the system unchanged. This allows the construction of similar boundary conditions on both flat and asymptotically null slices, which ought to work equally well for the original 1+log gauge and therefore have a broad application.

The prescriptions we describe here are all based on those of [40] and therefore related to those of [42].

### 8.2.1 Construction method

In the following sections two types of boundary conditions are constructed, maximally dissipative (Sect. 8.2.2) and constraint preserving (Sect. 8.2.3). In this section the basic construction method is outlined.

**Construct characteristic variables** Characteristic variables can be constructed for strongly hyperbolic systems according to the method given in Chap. 2. The subtletly here is deciding which system to build characteristic variables *for*. For example it may be desirable to construct maximally dissipative boundary conditions on the constraint subsystem of a set of equations. To do this the constraint subsystem is extracted and analyzed in addition to the full system. The principal part is thus rewritten as a set of uncoupled advection equations. At a spatial boundary each advection equation will transport data into or out of the domain of the solution.

**Construct continuum boundary conditions** A boundary condition is required for each incoming mode; incoming data must be specified. The speeds of incoming modes for the constraint system will coincide with a subset of those for the full system. To impose boundary conditions on the constraint system the boundary condition from the full system is replaced with that from the constraint system. In the case of the Einstein equations this is roughly the same as replacing an advection equation with its derivative in space. Some assumption must be made about the characteristic speeds throughout an evolution at the boundary. For example at the outer boundary, one may expect the gravitational fields to remain weak, so it makes sense to construct boundary conditions assuming that certain

modes will be ingoing, outgoing or have zero speed.

**Rewrite boundary conditions** The basic principle of the numerical recipe is that where possible the continuum boundary conditions ought to be specified through spatial derivatives of evolved variables. Other fields should be extrapolated to an appropriate order. To do this one starts by taking the continuum boundary conditions for the system, a set of equations which state that certain characteristic variables take specific values at the boundary. The characteristic variables are built from some primitive variables, and the first spatial derivative of others (the second spatial derivative in the constraint preserving case). If the number of boundary conditions is the same as the number primitive variables that appear differentiated in space, the set of equations can simply be solved for those quantities. Otherwise (as is often the case) certain variables must be chosen and solved for, either on the basis of mathematical elegance or by trial and error. Another frequently occuring problem is that one of the characteristic variables may have a small speed, liable to change sign over the course of an evolution. These slow-speed characteristic variables are treated individually; the boundary condition is solved for one of the undifferentiated primitive variables in the characteristic variable.

**Construct numerical boundary conditions** Where the boundary conditions require primitive variables be given, those fields are overwritten. Otherwise the boundary condition specifies a spatial derivative of an evolved variable at the boundary. The numerical prescription is to have enough ghostzones for the standard finite differencing stencil and populate them with data so that the boundary condition is satisfied. Other ghostzones are populated by extrapolating fields to an appropriate order.

The following examples should make the recipe clear.

### 8.2.2 Maximally dissipative boundary conditions

#### Spherical NOR

The principal part of the spherical NOR system with the gauge condition (7.19,7.20) with or without sources with $a = b = 1$ and $c = d = 0$,

$$\begin{pmatrix} \beta & 0 & -2\alpha & 0 & 0 & 0 & 2\gamma_{rr} \\ 0 & \beta & 0 & -2\alpha & 0 & 0 & 0 \\ \frac{\alpha(\rho-2)}{2\gamma_{rr}} & \frac{\alpha(\rho-1)}{\gamma_T} & \beta & 0 & \alpha & -1 & 0 \\ 0 & -\frac{\alpha}{2\gamma_{rr}} & 0 & \beta & 0 & 0 & 0 \\ 0 & 0 & \frac{\alpha(\rho-2)}{\gamma_{rr}} & \frac{2\alpha(\rho-2)}{\gamma_T} & \beta & 0 & 2-\rho \\ 0 & 0 & -\frac{\alpha^2\mu_L}{\gamma_{rr}} & -\frac{2\alpha^2\mu_L}{\gamma_T} & 0 & \beta & 0 \\ 0 & 0 & 0 & 0 & \frac{\alpha^2\mu_S}{\gamma_{rr}} & 0 & \beta \end{pmatrix} \begin{pmatrix} \gamma'_{rr} \\ \gamma'_T \\ K_{rr} \\ K_T \\ f_r \\ \alpha' \\ \beta' \end{pmatrix}, \tag{8.12}$$

which has characteristic variables $U_i$ $(i = 1, \ldots, 7)$

$$f + \tfrac{\rho-2}{2\gamma_{rr}}\gamma'_{rr} + \tfrac{\rho-2}{\gamma_T}\gamma'_T, \tag{8.13}$$

$$K_T \pm \tfrac{\gamma'_T}{2\sqrt{\gamma_{rr}}}, \tag{8.14}$$

$$-\alpha f - \tfrac{\alpha(\rho-2)}{2\gamma_{rr}}\gamma'_{rr} - \tfrac{\alpha(\rho-2)}{\gamma_T}\gamma'_T + \alpha' \pm \alpha\sqrt{\gamma_{rr}\mu_L}\left(\tfrac{K_{rr}}{\gamma_{rr}} + 2\tfrac{K_T}{\gamma_T}\right), \tag{8.15}$$

$$\beta' + \tfrac{\alpha\mu_S(\rho-2)}{\mu_L+\mu_S(\rho-2)}\left(\tfrac{K_{rr}}{\gamma_{rr}} + 2\tfrac{K_T}{\gamma_T}\right)$$

$$\pm\tfrac{\sqrt{\mu_S(2-\rho)\alpha}}{(\mu_L+\mu_S(\rho-2))\sqrt{\gamma_{rr}}}\left(\tfrac{\mu_L+(\mu_S-1)(2-\rho)}{2-\rho}f_r + \tfrac{2-\rho}{2\gamma_{rr}}\gamma'_{rr} + \tfrac{2-\rho}{\gamma_T}\gamma'_T - \log(\alpha)'\right) \tag{8.16}$$

with respective characteristic speeds

$$-\beta, \tag{8.17}$$

$$-\beta \pm \tfrac{\alpha}{\sqrt{\gamma_{rr}}}, \tag{8.18}$$

$$-\beta \pm \alpha\sqrt{\tfrac{\mu_L}{\gamma_{rr}}}, \tag{8.19}$$

$$-\beta \pm \alpha\sqrt{\tfrac{\mu_S(2-\rho)}{\gamma_{rr}}}. \tag{8.20}$$

Maximally dissipative and constraint preserving boundary conditions for a bespoke spherical reduction of NOR with densitized lapse and fixed shift were presented in

[40] with the NOR parameter $\rho = 2$ fixed. The principal part and characteristic variables for the spherical NOR system (4.106-4.113) with $\rho = 2$ closed with a densitized lapse and fixed shift are identical to those of the bespoke reduction [40]. Generalizing to $\rho \neq 2$ is straightforward. Those boundary conditions are not presented here.

Flat slices and asymptotically null slices are now considered separately.

**Flat slices** On asymptotically flat slices one expects the shift to be much smaller than the other variables at the outer boundary, so assume that

$$\frac{\alpha}{\sqrt{\gamma_{rr}}} \gg |\beta| \geq 0, \qquad \alpha \simeq \gamma_{rr} \simeq 1, \tag{8.21}$$

then the incoming speeds ($< 0$) of the system (at the outer boundary) become

$$-\beta, \quad -\beta - \frac{\alpha}{\sqrt{\gamma_{rr}}}, \quad -\beta - \alpha\sqrt{\frac{\mu_L}{\gamma_{rr}}}, -\beta - \alpha\sqrt{\frac{\mu_S(2-\rho)}{\gamma_{rr}}} \tag{8.22}$$

Data must be given to the characteristic variables with these speeds to render the initial boundary value problem well-posed,

$$f + \tfrac{\rho-2}{2\gamma_{rr}}\gamma'_{rr} + \tfrac{\rho-2}{\gamma_T}\gamma'_T = g_\beta, \tag{8.23}$$

$$K_T - \tfrac{\gamma'_T}{2\sqrt{\gamma_{rr}}} = g_{\text{physical}}, \tag{8.24}$$

$$-\alpha f - \tfrac{\alpha(\rho-2)}{2\gamma_{rr}}\gamma'_{rr} - \tfrac{\alpha(\rho-2)}{\gamma_T}\gamma'_T + \alpha' - \alpha\sqrt{\gamma_{rr}\mu_L}\left(\tfrac{K_{rr}}{\gamma_{rr}} + 2\tfrac{K_T}{\gamma_T}\right) = g_{\mu_L}, \tag{8.25}$$

$$\begin{aligned}\beta' + \tfrac{\alpha\mu_S(\rho-2)}{\mu_L+\mu_S(\rho-2)}\left(\tfrac{K_{rr}}{\gamma_{rr}} + 2\tfrac{K_T}{\gamma_T}\right) - \tfrac{\sqrt{\mu_S(2-\rho)}\alpha}{(\mu_L+\mu_S(\rho-2))\sqrt{\gamma_{rr}}}\Big(\tfrac{\mu_L+(\mu_S-1)(2-\rho)}{2-\rho}f_r \\ + \tfrac{2-\rho}{2\gamma_{rr}}\gamma'_{rr} + \tfrac{(2-\rho)}{\gamma_T}\gamma'_T - \log(\alpha)'\Big) = g_{\mu_S}\end{aligned} \tag{8.26}$$

With these boundary conditions the system may be shown to have a non-increasing energy [43]. Our preferred numerical prescription would be to solve the system (8.23,8.24, 8.25,8.26) for first derivatives of evolved variables. It is possible to solve this system of equations because the characteristic variables contain the derivatives of 4 evolved variables and there are 4 incoming modes giving equations. If $\beta$ becomes negative (or zero) at the boundary, which may happen because it is small

there, one of these incoming modes will become outgoing and the system may not be solved. This is unsatisfactory, since it will not be possible to evolve many spacetimes of interest, including even Minkowski (in trivial coordinates) since the shift is zero everywhere.

The problem is really caused by the existence of the $\beta$-speed mode in the NOR system. When the definition constraint $G_r$ is introduced there is freedom in deciding how it is to evolve. It is perfectly easy to choose an evolution equation which does not produce the troublesome $\beta$-speed mode. It would be interesting to look at how the NOR system (and by proxy any other BSSN-like system) could be modified to eliminate the $\beta$-speed mode. For now the focus is on finding boundary conditions for the NOR system as given.

Unsatisfactory as it is, the $\beta$-speed mode must be treated individually. Our treatment is directly analogous to that of [40]. Equations (8.24-8.26) are solved for $\gamma'_T, \alpha', \beta'$. Equation (8.23) is solved for $f$, and is imposed if $\beta > 0$. To implement this boundary condition numerically, ghost points are populated to satisfy the boundary conditions and ghost points for the other variables are populated by extrapolating the field inside the boundary (including $\gamma'_{rr}$ which appears in the characteristic variables).

**Asymptotically null slices** Surprisingly, boundary conditions for asymptotically null slices are much easier to construct than those for flat slices. Assuming

$$\beta \simeq -\frac{1}{2}, \qquad \alpha \simeq \frac{1}{2}\sqrt{\gamma_{rr}}, \tag{8.27}$$

at the outer boundary (implied by the growth the the $3+1$ variables on asymptotically null slices (8.6-8.11), the only incoming characteristic variable (assuming reasonable behavior of $\mu_L$ and $\mu_S$) is

$$K_T - \frac{\gamma'_T}{2\sqrt{\gamma_{rr}}} = g_{\text{physical}}, \tag{8.28}$$

(with speed $-\beta - \frac{\alpha}{\sqrt{\gamma_{rr}}}$) which is trivially solved for $\gamma'_T$. The asymptotically null boundary condition may be more robust than the flat case since the condition is

simpler. Data is only required for one variable and extrapolation may be used to populate the other ghost points. In addition, if the incoming mode becomes outgoing (which may occur since on asymptotically null slices the incoming coordinate light speed is small at large radius), it will be possible to use extrapolation at the outer boundary, whereas on flat slices the slow ($\beta$-speed) mode had to be treated seperately.

### Spherical BSSN

**BMn lapse, fn-driver shift** The principal part of the spherical BSSN system with the gauge condition (7.19,7.20) with or without source terms (before the change to conformal variables) is

$$\begin{pmatrix} \beta & 0 & -2\alpha & 0 & 0 & 0 & 2\gamma_{rr} \\ 0 & \beta & 0 & -2\alpha & 0 & 0 & 0 \\ -\frac{4\alpha}{9\gamma_{rr}} & \frac{\alpha}{9\gamma_T} & \beta & 0 & \frac{2}{3}\alpha & -1 & 0 \\ \frac{2\alpha\gamma_T}{9\gamma_{rr}^2} & -\frac{\alpha}{18\gamma_{rr}} & 0 & \beta & -\frac{\alpha\gamma_T}{3\gamma_{rr}} & 0 & 0 \\ 0 & 0 & -\frac{4\alpha}{3\gamma_{rr}} & -\frac{8\alpha}{3\gamma_T} & \beta & 0 & -\frac{4}{3} \\ 0 & 0 & -\frac{\alpha^2\mu_L}{\gamma_{rr}} & -\frac{2\alpha^2\mu_L}{\gamma_T} & 0 & \beta & 0 \\ 0 & 0 & 0 & 0 & \frac{\alpha^2(\gamma_{rr}\gamma_T^2)^{1/3}\mu_S}{\gamma_{rr}} & 0 & \beta \end{pmatrix} \begin{pmatrix} \gamma'_{rr} \\ \gamma'_T \\ K_{rr} \\ K_T \\ f_r \\ \alpha' \\ \beta' \end{pmatrix}, \quad (8.29)$$

which has characteristic variables $U_i$ $(i = 1, \ldots, 7)$

$$f_r - \tfrac{2\gamma'_{rr}}{3\gamma_{rr}} - \tfrac{4\gamma'_T}{3\gamma_T}, \quad (8.30)$$

$$f_r - \tfrac{2\gamma'_{rr}}{3\gamma_{rr}} + \tfrac{\gamma'_T}{6\gamma_T} \pm \tfrac{3\sqrt{\gamma_{rr}}}{\gamma_T} K_T, \quad (8.31)$$

$$\alpha' \pm \alpha\sqrt{\mu_L}\left(\tfrac{K_{rr}}{\gamma_{rr}} + 2\tfrac{K_T}{\gamma_T}\right), \quad (8.32)$$

$$\beta' + \tfrac{4\alpha\gamma_{rr}}{3\gamma_{rr}^{2/3}/\gamma_T^{2/3} - 4\gamma_{rr}}\left(\tfrac{K_{rr}}{\gamma_{rr}} + 2\tfrac{K_T}{\gamma_T}\right) \pm \tfrac{\sqrt{3}\gamma_{rr}^{1/3}}{\gamma_T^{1/3}\sqrt{\mu_L}}\left(\tfrac{2\alpha'}{3\gamma_{rr}^{2/3}/\gamma_T^{2/3} - 4\gamma_{rr}} - \tfrac{\gamma_T^{2/3}\mu_L}{2\gamma_{rr}^{2/3}} f_r\right), \quad (8.33)$$

with respective characteristic speeds

$$-\beta, \tag{8.34}$$

$$-\beta \pm \tfrac{\alpha}{\sqrt{\bar{\gamma}_{rr}}}, \tag{8.35}$$

$$-\beta \pm \alpha\sqrt{\tfrac{\mu_L}{\bar{\gamma}_{rr}}}, \tag{8.36}$$

$$-\beta \pm \alpha\sqrt{\mu_S}\tfrac{2\bar{\gamma}_T^{1/3}}{\sqrt{3}\bar{\gamma}_{rr}^{1/3}}. \tag{8.37}$$

After the conformal decomposition the characteristic variables can be rewritten

$$\bar{\gamma}_{rr}\bar{\Gamma}^r - 8\phi', \tag{8.38}$$

$$-\tfrac{2\bar{\gamma}'_{rr}}{3\bar{\gamma}_{rr}} + \tfrac{\bar{\gamma}'_T}{6\bar{\gamma}_T} - 2\phi' + \bar{\gamma}_{rr}\bar{\Gamma}^r \pm e^{2\phi}\sqrt{\bar{\gamma}_{rr}}\Big(K + \tfrac{3\bar{A}_T}{\bar{\gamma}_T}\Big), \tag{8.39}$$

$$\alpha' \pm \sqrt{\bar{\gamma}_{rr}\mu_L}\alpha e^{2\phi}K, \tag{8.40}$$

$$\tfrac{2\alpha\sqrt{\mu_S}}{\sqrt{\bar{\gamma}_{rr}}(3\mu_L - 4e^{4\phi}\mu_S)}\Big(2e^{4\phi}\sqrt{\mu_S}K \pm \sqrt{3}\log(\alpha)'\Big) + \beta' \mp \tfrac{1}{2}\sqrt{3\bar{\gamma}_{rr}\mu_S}\alpha\bar{\Gamma}^r. \tag{8.41}$$

The characteristic speeds (8.37) can be written as

$$-\beta \pm \alpha\sqrt{\frac{\mu_S}{\bar{\gamma}_{rr}}}. \tag{8.42}$$

**Densitized lapse, fixed shift** The principal part of the spherical BSSN system with the densitized lapse and fixed shift is

$$\begin{pmatrix} \beta & 0 & -2\alpha & 0 & 0 \\ 0 & \beta & 0 & -2\alpha & 0 \\ -\frac{17\alpha}{18\bar{\gamma}_{rr}} & -\frac{8\alpha}{9\bar{\gamma}_T} & \beta & 0 & 0 \\ \frac{2\alpha\bar{\gamma}_T}{9\bar{\gamma}_{rr}^2} & -\frac{\alpha}{18\bar{\gamma}_{rr}} & 0 & \beta & -\frac{\alpha\bar{\gamma}_T}{3\bar{\gamma}_{rr}} \\ 0 & 0 & -\frac{4\alpha}{3\bar{\gamma}_{rr}} & -\frac{8\alpha}{3\bar{\gamma}_T} & \beta \end{pmatrix} \begin{pmatrix} \bar{\gamma}'_{rr} \\ \bar{\gamma}'_T \\ K_{rr} \\ K_T \\ f_r \end{pmatrix}, \tag{8.43}$$

which has characteristic variables after the conformal decomposition $U_i$ $(i = 1, \ldots, 5)$

$$\bar{\gamma}_{rr}\bar{\Gamma}^r - 8\phi', \tag{8.44}$$

$$-\tfrac{17\bar{\gamma}'_{rr}}{12\bar{\gamma}_{rr}} - \tfrac{4\bar{\gamma}'_T}{3\bar{\gamma}_T} - 11\phi' + \bar{\gamma}_{rr}\bar{\Gamma}^r \pm \tfrac{1}{2}\sqrt{\bar{\gamma}_{rr}}e^{2\phi}\Big(K + 3\tfrac{\bar{A}_{rr}}{\bar{\gamma}_{rr}}\Big), \tag{8.45}$$

$$\tfrac{K}{2} \pm \tfrac{3e^{-2\phi}}{\sqrt{\bar{\gamma}_{rr}}}\phi', \tag{8.46}$$

with respective characteristic speeds

$$-\beta, \tag{8.47}$$

$$-\beta \pm \tfrac{\alpha}{\sqrt{\gamma_{rr}}}, \tag{8.48}$$

$$-\beta \pm \alpha\sqrt{\tfrac{\mu_L}{\gamma_{rr}}}, \tag{8.49}$$

Flat slices and asymptotically null slices are again considered separately.

**Flat slices** Under the assumptions (8.22), the incoming speeds ($< 0$) of the BSSN system (at the outer boundary) with BMn lapse and fn-driver shift become

$$-\beta, \quad -\beta - \frac{\alpha}{\sqrt{\gamma_{rr}}}, \quad -\beta - \alpha\frac{\sqrt{\mu_L}}{\sqrt{\gamma_{rr}}}, \quad -\beta - \alpha\frac{\sqrt{\mu_S}}{\sqrt{\bar{\gamma}_{rr}}} \tag{8.50}$$

Data must be given to the characteristic variables with these speeds,

$$\bar{\gamma}_{rr}\bar{\Gamma}^r - 8\phi' = g_\beta, \tag{8.51}$$

$$-\tfrac{2\bar{\gamma}'_{rr}}{3\bar{\gamma}_{rr}} + \tfrac{\bar{\gamma}'_T}{6\bar{\gamma}_T} - 2\phi' + \bar{\gamma}_{rr}\bar{\Gamma}^r - e^{2\phi}\sqrt{\bar{\gamma}_{rr}}\Big(K + \tfrac{3\bar{A}_T}{\bar{\gamma}_T}\Big) = g_{\text{physical}}, \tag{8.52}$$

$$\alpha' - \sqrt{\bar{\gamma}_{rr}\mu_L}\alpha e^{2\phi}K = g_{\mu_L}, \tag{8.53}$$

$$\begin{aligned}\tfrac{2\alpha\sqrt{\mu_S}}{\sqrt{\bar{\gamma}_{rr}}(3\mu_L - 4e^{4\phi}\mu_S)}\Big(2e^{4\phi}\sqrt{\mu_S}K - \sqrt{3}\log(\alpha)'\Big)\\ +\beta' + \tfrac{1}{2}\sqrt{3\bar{\gamma}_{rr}\mu_S}\alpha\bar{\Gamma}^r = g_{\mu_S}.\end{aligned} \tag{8.54}$$

The enforced $D$ constraint can be added to these conditions

$$\frac{\bar{\gamma}'_{rr}}{\bar{\gamma}_{rr}} + 2\frac{\bar{\gamma}'_T}{\gamma_T} \equiv 0. \tag{8.55}$$

The resulting set of equations (8.52-8.55) can be solved for $\bar{\gamma}'_{rr}$, $\bar{\gamma}'_T$, $\alpha'$ and $\beta'$. If $\beta > 0$, (8.51) can be solved for $\bar{\Gamma}^r$.

With densitized lapse and fixed shift the incoming characteristic fields are

$$\bar{\gamma}_{rr}\bar{\Gamma}^r - 8\phi' = g_\beta, \tag{8.56}$$

$$-\tfrac{17\bar{\gamma}'_{rr}}{12\bar{\gamma}_{rr}} - \tfrac{4\bar{\gamma}'_T}{3\bar{\gamma}_T} - 11\phi' + \bar{\gamma}_{rr}\bar{\Gamma}^r + \tfrac{1}{2}\sqrt{\bar{\gamma}_{rr}}e^{2\phi}\Big(K + 3\tfrac{\bar{A}_{rr}}{\bar{\gamma}_{rr}}\Big) = g_{\text{physical}} \tag{8.57}$$

$$\tfrac{K}{2} - \tfrac{3e^{-2\phi}}{\sqrt{\bar{\gamma}_{rr}}}\phi' = g_{\text{densitized}}, \tag{8.58}$$

The enforced $D$ constraint can be added to these conditions

$$\frac{\bar{\gamma}'_{rr}}{\bar{\gamma}_{rr}} + 2\frac{\bar{\gamma}'_T}{\gamma_T} \equiv 0. \tag{8.59}$$

The resulting set of equations (8.57-8.59) can be solved for $\bar{\gamma}'_{rr}$, $\bar{\gamma}'_T$ and $\phi'$. If $\beta > 0$, (8.51) can be solved for $\bar{\Gamma}^r$.

**Asymptotically null slices** Assuming the slicing is asymptotically null towards the boundary (8.27) the only incoming characteristic variable with BMn lapse and fn-driver shift at the outer boundary is the physical

$$-\frac{2\bar{\gamma}'_{rr}}{3\bar{\gamma}_{rr}} + \frac{\bar{\gamma}'_T}{6\bar{\gamma}_T} - 2\phi' + \bar{\gamma}_{rr}\bar{\Gamma}^r - e^{2\phi}\sqrt{\bar{\gamma}_{rr}}\left(K + \frac{3\bar{A}_T}{\bar{\gamma}_T}\right) = g_{\text{physical}}, \tag{8.60}$$

with speed $-\beta - \frac{\alpha}{\sqrt{\bar{\gamma}_{rr}}}$. As on flat slices the enforced $D$ constraint can be added to these conditions

$$\frac{\bar{\gamma}'_{rr}}{\bar{\gamma}_{rr}} + 2\frac{\bar{\gamma}'_T}{\gamma_T} \equiv 0. \tag{8.61}$$

Combined, the boundary condition and enforced constraint can be solved for $\bar{\gamma}'_{rr}$ and $\bar{\gamma}'_T$.

Since the characteristic surfaces of the system with densitized lapse and fixed shift are just null surfaces, maximally dissipative boundary conditions with densitized lapse and fixed shift are the same as those on flat slices.

### 8.2.3 Constraint preserving boundary conditions

Analyzing the constraint subsystem is not completely straightforward. The constraint evolution system in generic coordinates constains second spatial derivatives of the auxiliary $G_i$ constraint, whilst the Hamiltonian and momentum constraints appear with at most one spatial derivative suggesting the canonical structure

$$\dot{u} \simeq u' + v \tag{8.62}$$

$$\dot{v} \simeq u'' + v' \tag{8.63}$$

for the principal part of the system.

In spherical symmetry the second spatial derivatives of $G_r$ disappear, so naively one would think that the constraint system can be analyzed as a fully first order system. The constraint subsystem should not be thought of as an auxiliary system but as an evolution system implied by the full evolution. Analyzing the constraint evolution system as a fully first order system is inconsistent with the principal part analysis for the full system. In other words, since the first derivative of the Hamiltonian and momentum constraints implicitly contain third spatial derivatives of the metric, whilst first derivatives of $G_r$ contain only second derivatives of the metric, $G_r'$ terms can not be considered principal in the presence of $H'$ and $M_r'$ terms.

Surprisingly a naive analysis of the spherical NOR constraint system with $\rho = 2$ finds that the system is strongly hyperbolic [40] although the characteristic variables constructed differ from those with a consistent treatment.

### Spherical NOR

The principal part of the constraint system for the spherical NOR system is the matrix.

$$\begin{pmatrix} \beta & -\frac{\alpha}{\gamma_{rr}} & 0 \\ -\alpha & \beta & 0 \\ 0 & 2\alpha & \beta \end{pmatrix} \begin{pmatrix} H \\ M_r \\ G_r' \end{pmatrix}, \tag{8.64}$$

which has characteristic variables

$$G_r' + 2\gamma_{rr} H, \tag{8.65}$$

$$M_r \pm \sqrt{\gamma_{rr}} H, \tag{8.66}$$

with characteristic speeds

$$-\beta, \tag{8.67}$$

$$-\beta \pm \frac{\alpha}{\sqrt{\gamma_{rr}}}. \tag{8.68}$$

Again flat and asymptotically null slices are considered separately.

**Flat slices** On asymptotically flat slices the constraint system will have 1 or 2 incoming variables, whereas the full system has 3 or 4 incoming characteristic variables (8.23-8.26). The maximally dissipative incoming physical and $\beta$-speed boundary conditions are replaced with those of the same speeds from the constraint system. The resulting continuum boundary condition is then

$$G_r' + 2\gamma_{rr} H = 0 \tag{8.69}$$

$$M_r - \sqrt{\gamma_{rr}} H = 0, \tag{8.70}$$

$$-\alpha f - \tfrac{\alpha(\rho-2)}{2\gamma_{rr}}\gamma_{rr}' - \tfrac{\alpha(\rho-2)}{\gamma_T}\gamma_T' + \alpha' - \alpha\sqrt{\gamma_{rr}\mu_L}\left(\tfrac{K_{rr}}{\gamma_{rr}} + 2\tfrac{K_T}{\gamma_T}\right) = g_{\text{lapse}}, \tag{8.71}$$

$$\begin{aligned}\beta' + \tfrac{\alpha\mu_S(\rho-2)}{\mu_L+\mu_S(\rho-2)}\left(\tfrac{K_{rr}}{\gamma_{rr}} + 2\tfrac{K_T}{\gamma_T}\right) - \tfrac{\sqrt{\mu_S(2-\rho)\alpha}}{(\mu_L+\mu_S(\rho-2))\sqrt{\gamma_{rr}}}\Big(\tfrac{\mu_L+(\mu_S-1)(2-\rho)}{2-\rho} f_r \\ + \tfrac{2-\rho}{2\gamma_{rr}}\gamma_{rr}' + \tfrac{(2-\rho)}{\gamma_T}\gamma_T' - \log(\alpha)'\Big) = g_{\text{shift}}\end{aligned} \tag{8.72}$$

Equations (8.69,8.70) are rewritten in terms of the evolved variables and solved for $f_r$ and $\gamma_T''$ respectively. As in the MDBC case if $\beta > 0$ then $f$ is overwritten to satisfy the incoming $\beta$-speed mode (now given by (8.70)). $\alpha'$ and $\beta'$ are given by (8.71,8.72) and ghost points are populated to satisfy these conditions. Finally ghost points are populated to give the other derivatives.

**Asymptotically null slices** Again boundary conditions for asymptotically null slices are much create than those for flat slices. Assuming (8.27) at the outer boundary, the remaining incoming mode is

$$M_r - \sqrt{\gamma_{rr}} H = 0. \tag{8.73}$$

The incoming data for this characteristic is set to zero. The constraint system characteristic variable is rewritten in terms of the primitive variables. The resulting equation contains the second derivative of only $\gamma_T$ and can be solved for it. Since the main system and the constraint system both only have one incoming mode, only this condition need be imposed.

Numerically the boundary condition is imposed by extrapolating all variables to compute first derivatives. Eqn. (8.73) is then imposed by populating ghostzones for $\gamma_T$.

### Spherical BSSN

The principal part of the constraint system for the spherical BSSN system is the matrix.

$$\begin{pmatrix} \beta & -\frac{\alpha}{\gamma_{rr}} & 0 \\ \frac{\alpha}{3} & \beta & \frac{2\alpha}{3\gamma_{rr}} \\ 0 & 2\alpha & \beta \end{pmatrix} \begin{pmatrix} H \\ M_r \\ G'_r \end{pmatrix}, \tag{8.74}$$

which has characteristic variables

$$G'_r + 2\gamma_{rr}H, \tag{8.75}$$

$$G'_r + \tfrac{1}{2}\gamma_{rr}H \pm \tfrac{3}{2}\sqrt{\gamma_{rr}}M_r, \tag{8.76}$$

with characteristic speeds

$$-\beta, \tag{8.77}$$

$$-\beta \pm \tfrac{\alpha}{\sqrt{\gamma_{rr}}}. \tag{8.78}$$

Again flat and asymptotically null slices are considered separately.

## 8.2.4 Numerical tests of boundary conditions on flat slices

In this section simple convergence results for the boundary conditions presented in the previous sections are presented. The focus is on both norm convergence to an exact solution, and pointwise convergence, in particular at the outer boundary.

Numerical tests of the boundary conditions for the NOR-$\Theta$ and BSSN-$\Theta$ systems are left for future work.

### Initial data and numerical method

Kerr-Schild slices through the Schwarchzschild spacetime

$$ds^2 = -\left(1 - \frac{2M}{R}\right) dT^2 + \frac{4M}{R}\, dT\, dR + \left(1 + \frac{2M}{R}\right) dR^2 + R^2\, d\Omega^2, \qquad (8.79)$$

are evolved, with either the densitized lapse and fixed shift, or the evolved gauge (7.21, 7.22). With densitized lapse the blackhole excision boundary is set initially at $1.4M$. With the evolved gauge the excision boundary is set initially at $1.2M$. In either case the maximally dissipative boundary conditions described in the last section are imposed at the outer boundary, which is placed around $70M$. The results presented in this section were performed with a low spatial resolution of $h = 0.1M$, fourth order Runge-Kutta time integration and second order accurate finite differences in space. As in the wave equation tests in Chap. 6.2.1, the blackhole boundary all fields are extrapolated according to

$$h^5 D_+^5 U_{N+1} = 0, \qquad (8.80)$$

for the fourth order scheme and

$$h^3 D_+^3 U_{N+1} = 0, \qquad (8.81)$$

for the second order scheme. A touch of artificial dissipation $-\sigma h^3 (D_+ D_-)^2$ (second order) and $-\sigma h^5 (D_+ D_-)^3$ (fourth order) is used over the grid. Extrapolation is used to populate the additional ghostzones required by the dissipation stencil. The numerical results presented in [40] are in some sense more robust than those presented here because the outer boundary has now been pushed further into the weak-field region away from the blackhole. This problem is mitigated by looking closely at pointwise convergence near the boundary as well as norm convergence.

### NOR

Both the second and fourth order maximally dissipative and constraint preserving conditions display perfect norm convergence with densitized lapse, fixed shift and

various values of the $\rho$ parameter.

With BMn 1+log lapse (with source terms) and fn-driver $\rho = 2$ does not give a strongly hyperbolic system, so the $\beta$-speed characteristic variable couples to derivatives of other primitive fields. The structure of the characteristic fields is such that the resulting boundary conditions require an "unimposed numerical derivative" (either $\gamma'_{rr}$ or $\beta'$) to be used when imposing the numerical boundary condition; this complication is too much for the numerical maximally dissipative boundary condition to deal with and the neat convergence properties are lost. Large $G_r$ constraint violations enter through the boundary from the first time-step. The numerical recipe for maximally dissipative and constraint preserving boundary conditions with evolved gauge conditions on flat slices is completely unsuccessful. Interestingly, if the slow $\beta$-speed boundary condition is replaced with

$$f = g_\beta, \tag{8.82}$$

the correct boundary condition for $\rho = 2$, (densitized lapse and fixed shift) perfect convergence can be recovered, despite the fact that this is not the natural continuum boundary condition for the system. Robust tests could be used to test the condition further and perhaps give some clue to the well-posedness of the initial boundary value problem. Such tests are not performed here.

Fig. 8.1 demonstrates pointwise second order convergence properties of the solution at the outer boundary with densitized lapse and fixed shift (*left*) and the evolved BMn 1+log lapse (with source terms) and fn-driver (*right*). The plot shows rescaled errors at two resolutions. For perfect pointwise convergence the rescaled (higher resolution) errors should overlay those from the lower resolution. Fig. 8.2) corroborates the convergence of the constraint preserving boundary condition with densitized lapse and fixed shift. The right hand plot compares incoming constraint violation with and without the constraint preserving condition.

Fig. 8.3:*left* shows that the modified boundary condition (8.82) on the slow-speed mode converges. As resolution is increased the rescaled errors coincide. The plot

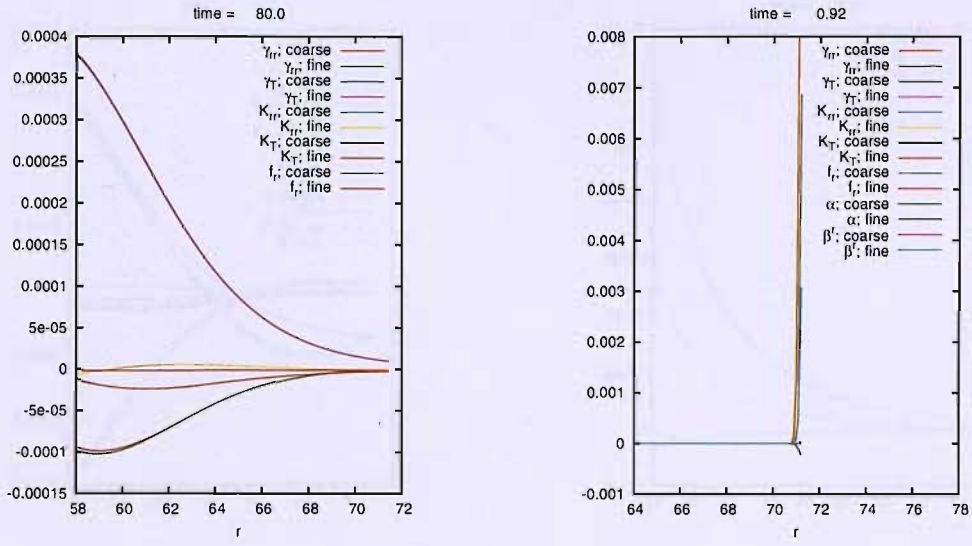


Figure 8.1: *left:* Second order pointwise convergence of spherical NOR with $\rho = 2$, densitized lapse, fixed shift and maximally dissipative boundary conditions. *right:* Pointwise convergence of spherical NOR with $\rho = 1$, BMn lapse, fn-driver shift and maximally dissipative boundary conditions. Similar results are found with a densitized lapse, fixed shift and $\rho \neq 2$.

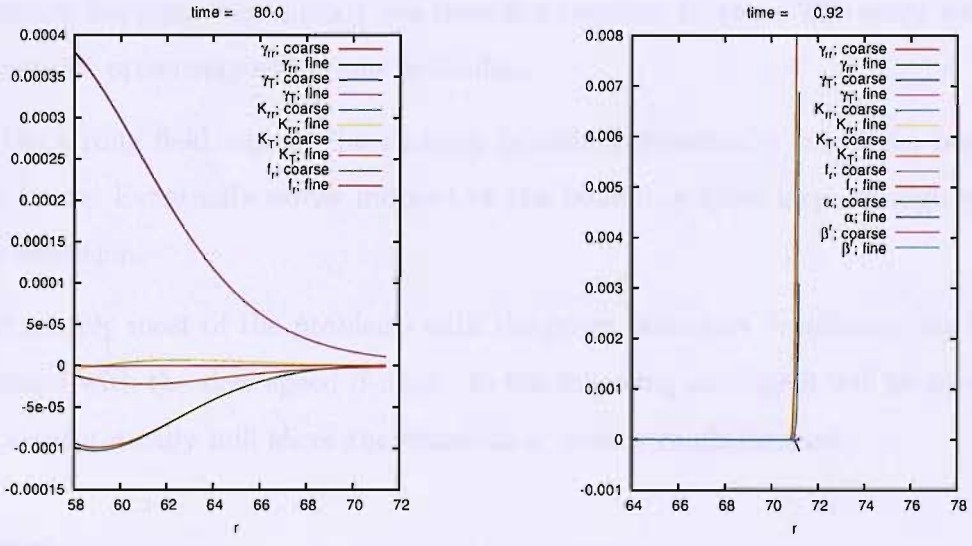


Figure 8.2: *left:* Second order pointwise convergence of spherical NOR with $\rho = 1$, densitized lapse, fixed shift and constraint preserving boundary conditions. *right:* Incoming constraint violation with maximally dissipative and constraint preserving boundary conditions.

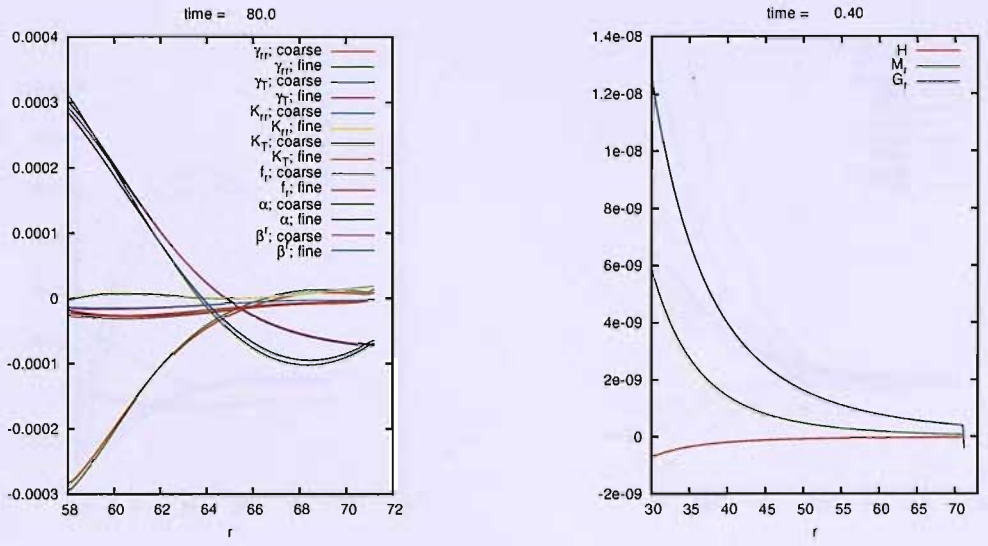


Figure 8.3: *left:* As in Fig. 8.1:(*right*) with the modified condition (8.82). *right:* Incoming constraint violation with the modified maximally dissipative condition.

on the right hand side of Fig. 8.3 shows the behavior of the constraints at the outer boundary with the modified condition. The (relatively) large $G_r$ constraint violation happens very quickly but does not continue to grow. The story with the constraint preserving conditions is similar.

In the strong field region, the excision boundary generically converges but does not freeze. Eventually errors induced at the boundary grow large enough to halt the evolution.

Fortunately most of the problems with the outer boundary conditions can be associated with the slow speed $\beta$-mode. In the following sections it will be seen that on asymptotically null slices the situation is more straightforward.

### BSSN

The simplicity of the BSSN characteristic variables appears to alleviate the issues associated with the $\beta$-speed mode with the NOR formulation. The slow speed

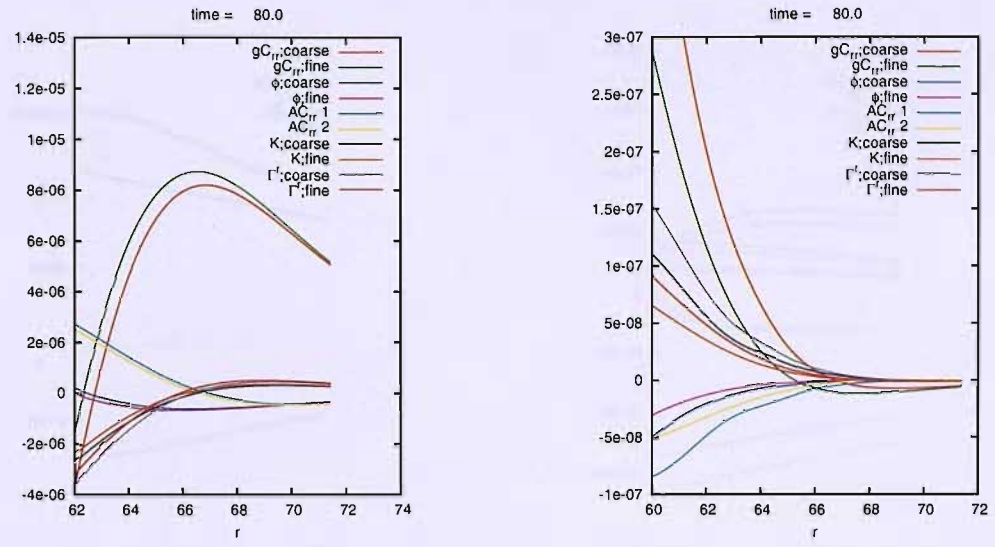


Figure 8.4: As in Fig. 8.1:*left* but with the BSSN system, densitized lapse and fixed shift. (*left:*) second order scheme. (*right:*) fourth order scheme.

mode couples to only the $\phi$ variable. Numerical convergence tests display second and fourth order convergence with either densitized lapse and fixed shift (Fig. 8.4) or BMn 1+log and gamma-driver shift. Fig. 8.5 plots the pointwise convergence of the second (*left*) and fourth (*right*) order accurate finite difference schemes. In each case some variables are omitted for clarity.

The excision boundary is far better behaved than in the NOR case. Although the largest errors appear at the blackhole boundary, they converge (as in the NOR case) and do not oscillate and grow indefinitely. The boundary effectively freezes after around $10M$ of evolution, allowing the evolution to run essentially forever ($> 1000M$) even at the resolutions considered here.

## 8.3 Numerical constraint damping tests

Before attempting to evolve asymptotically null initial data we compare the damped and undamped constraints on simple initial data described in the previous sec-

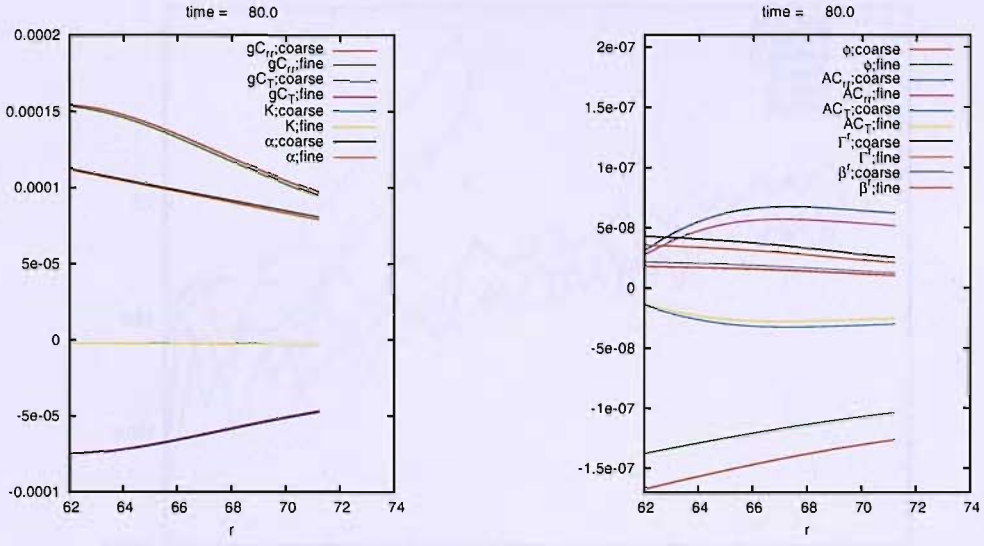


Figure 8.5: As in Fig. 8.1:*left* but with the BSSN system, BMn lapse and gamma-driver shift. (*left:*) second order scheme. (*right:*) fourth order scheme.

tion 8.2.4.

Again numerical evolutions of NOR-Θ and BSSN-Θ are left for future work.

**NOR** First the numerical results for NOR with densitized lapse and fixed shift; the results of constraint damping are disastrous (Fig. 8.6) the excision boundary blows up. Whilst it appears that the damping is successful in the $G_r$ constraint until $t \sim 45M$, the Hamiltonian and momentum constraints are better off without it.

Tests with the evolved gauge are more promising. Fig. 8.7 demonstrates the clear effectiveness of the constraint damping scheme in this case. The majority of the constraint violation in each case appears at the excision boundary. With constraint damping the violation is instantly reduced and soon decays.

Without damping the excision boundary blows up as reflections from the outer boundary return. This problem may be mitigated by choosing better numerical or continuum boundary conditions, but at least with our conditions constraint

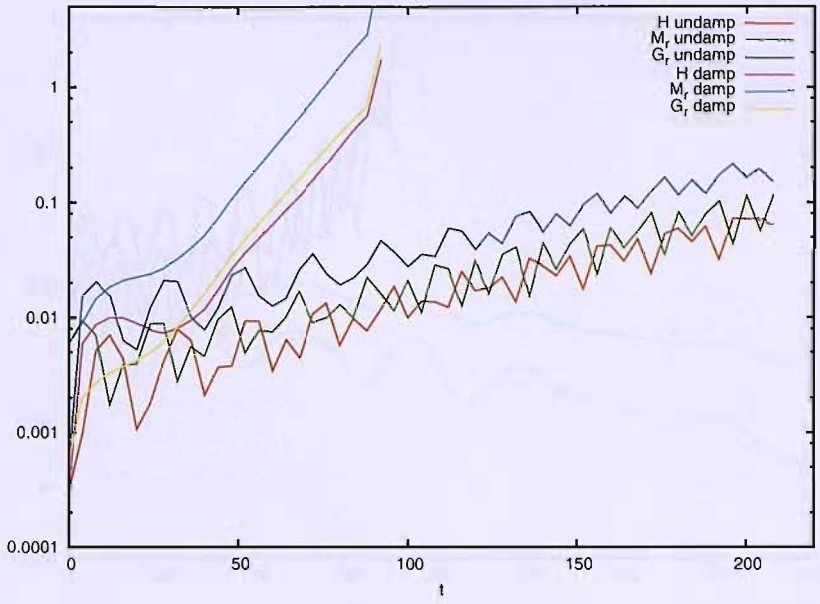


Figure 8.6: The NOR constraints with and without damping, with fixed lapse and densitized shift

damping is essential for long evolutions with live gauge conditions and excision.

**BSSN** The first remarkable thing about the BSSN evolutions with the gauge BMn lapse and fn-driver shift (with source) (7.21,7.22) is that they settle down essentially forever with no constraint damping, in contrast to the behavior of the NOR system. Applying the constraint damping terms near the outer boundary causes an interaction with the boundary condition, resulting in large errors. If the constraints near the outer boundary are left undamped by exponentially cutting off the damping near the boundary, and a small constraint damping coefficient $\kappa = 0.2$ is chosen the damping is partially successful with densitized lapse and fixed shift ($H$ and $G_r$ are damped Fig. 8.9) and completely successful with BMn lapse and gamma-driver shift (Fig. 8.9).

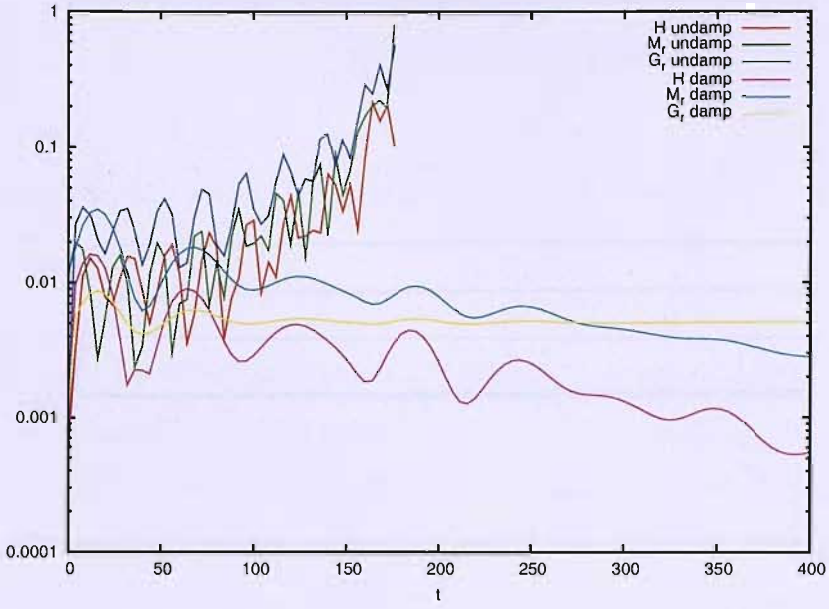


Figure 8.7: The NOR constraints with and without damping with BMn lapse and fn-driver shift (with sources).

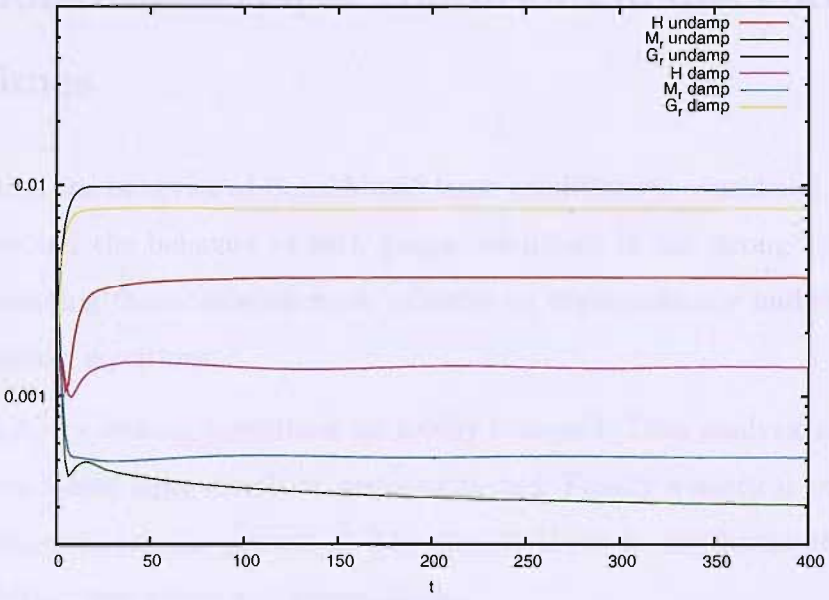


Figure 8.8: The BSSN constraints with and without damping with densitized lapse and fixed shift. $\kappa = 0.2$ was taken in the damped runs.

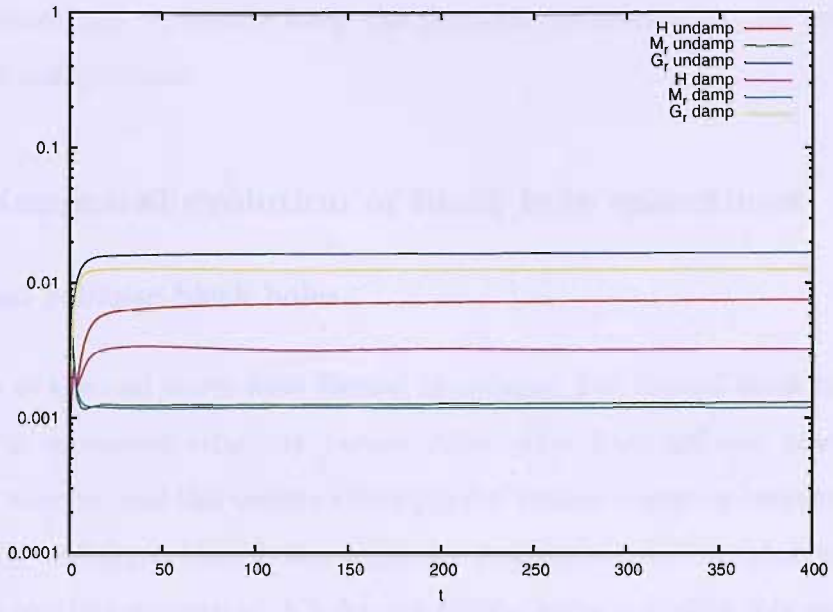


Figure 8.9: The BSSN constraints with and without damping with BMn lapse and gamma-driver shift. $\kappa = 0.2$ was taken in the damped runs.

## 8.4 Bona-Massó lapse conditions in blackhole space-times

In this section the behavior of Bona-Massó lapse conditions is considered. The aim is to understand the behavior of such gauge conditions in the strong-field region before considering their behavior more robustly on asymptotically null slices with the full Einstein equations.

Firstly symmetry seeking conditions are briefly reviewed. Then analytic end-states for the Bona-Massó lapse condition are constructed. Finally numerical pure gauge and Einstein evolutions are presented. The numerical results are discussed in terms of the analytical end-states and gauge shocks.

The work in this section is based closely on that presented in [2], and was written largely by C. Gundlach as part of a collaboration with D. Garfinkle and DH. The

work presented here represents fairly the research undertaken by the author as part of that collaboration.

### 8.4.1 Numerical evolution of black hole spacetimes

#### Eternal and collapse black holes

Black holes in the real world have formed in collapse, but eternal black holes are often used in numerical relativity because they differ from collapse black holes only in the interior, and this cannot affect physics outside. Here we concentrate on non-rotating, uncharged black holes, which are described by the Kruskal extension of the Schwarzschild spacetime. A bifurcate Killing horizon divides this spacetime into past (P), future (F), "left" (L) and "right" (R) regions. The future and past timelike ($i^+$ and $i^-$) and null ($\mathscr{I}^+$ and $\mathscr{I}^-$) infinities and the spacelike infinity $i^0$ all exist in left ($L$) and right ($R$) copies. Slices extending from $i^0_L$ to $i^0_R$ have wormhole geometry, see Fig. 8.10. Binary (or multiple) black hole initial data can be represented by a wormhole leading to a separate copy of $i^0_L$ for each black hole. In the "puncture" method [44], each $i^0_L$ is then represented in coordinates by a point where the conformal factor diverges.

By contrast, black holes formed from regular data through collapse have trivial spatial topology, similar to the Schwarzschild spacetime but with part of R and F, and all of P and L, covered up by the collapsing star [45] – see Fig. 8.13.

#### Singularity-avoiding slicings

Both in collapse and in eternal black holes one can use slicings which avoid the singularity. Any timelike worldline inside a black hole has finite length, while any timelike worldline with limited total acceleration outside the black hole has infinite length. The lapse measures the rate of proper time per coordinate time for an observer normal to the time slices, and so one might think that the lapse must go

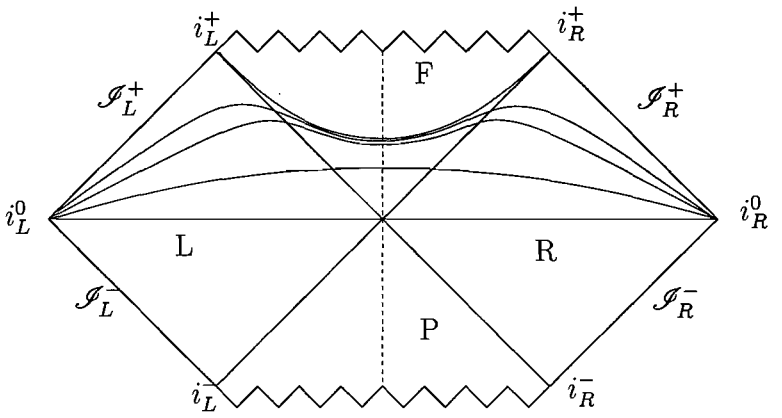


Figure 8.10: Spacetime diagram of the Schwarzschild spacetime, with the angular coordinates suppressed. The horizontal line from $i_L^0$ to $i_R^0$ is the time-symmetric wormhole slice typically used as initial data in puncture evolutions of a Schwarzschild black holes. The curved lines schematically represent the slicing generated from these initial data by BMn lapse with $\alpha = 1$ initially. They approach the slice $R = R_0$, which links $i_L^+$ to $i_R^+$. The vertical dashed line represents the symmetry boundary which can replace the left-right reflection symmetry of this slicing. As the slices approach $R = R_0$, the approximately cylindrical wormhole grows longer linearly with time.

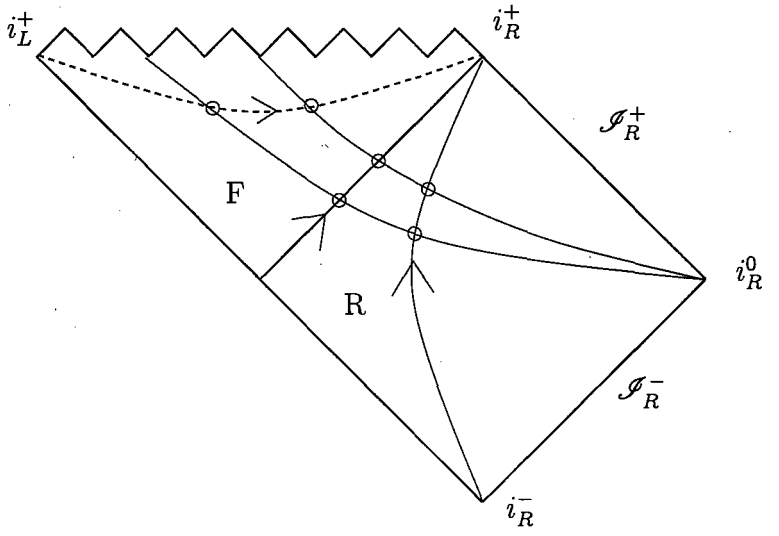


Figure 8.11: The same spacetime diagram, schematically showing a Killing slicing that ends at the future singularity, such as Kerr-Schild slices. The lines with arrows are trajectories of the Killing vector (lines of constant $R$) and the beads on them represent surfaces of constant coordinate $r$ if the Killing shift is used. In particular, the dashed line could serve as a Killing excision boundary.

to zero everywhere inside the black hole in order to avoid the singularity, and that because the slices keep advancing outside the black hole, their intrinsic geometry must deform without limit as time goes on, until large gradients can no longer be resolved. Such "slice stretching" was indeed encountered in early black hole simulations, and motivated the development of black hole excision [20].

Only later it was realised clearly that singularity-avoiding slicings need not lead to slice stretching [46]. If the lapse is chosen such that the slice is Lie-dragged along the Killing vector field everywhere, its intrinsic geometry becomes time-independent. This is true also inside the black hole where the Killing vector field that generates time translations at infinity becomes spacelike (and so the spacetime is not technically stationary), as long as this Killing vector field is nowhere parallel to the slicing. Once the geometry of the slice has become time-independent, a suitable shift condition then makes the spatial metric coefficients explicitly time-independent. With this lapse and shift $\partial/\partial t$ becomes the Killing vector (spacelike inside a black hole). Coordinate conditions which generate Killing coordinates asymptotically starting from generic initial coordinates were called "symmetry-seeking" in [47].

Even more recently it was realised that the lapse need not collapse either [48]. Note that

$$\left(\frac{\partial}{\partial t}\right)^a \equiv \alpha n^a + \beta^i \left(\frac{\partial}{\partial x^i}\right)^a \tag{8.83}$$

is a sum of two terms. Define some scalar $\sigma$ to measure distance from the singularity. (In Schwarzschild spacetime, an obvious choice is the area radius $R$.) For any given $\alpha$ and $\sigma$, $\beta^i$ then can be chosen to set $\dot{\sigma} = 0$, except where $\sigma_{,i} = 0$. (We use a dot to denote $\partial/\partial t$). In other words, the lapse in a Killing coordinate system vanishes only where the time slices are tangential to the Killing vector field. Every regular time slice in a collapse spacetime, and every wormhole slice through an eternal black hole has such an obstruction point, namely a local minimum of $\sigma$ (Fig. 8.10). However, a slice that becomes asymptotically cylindrical

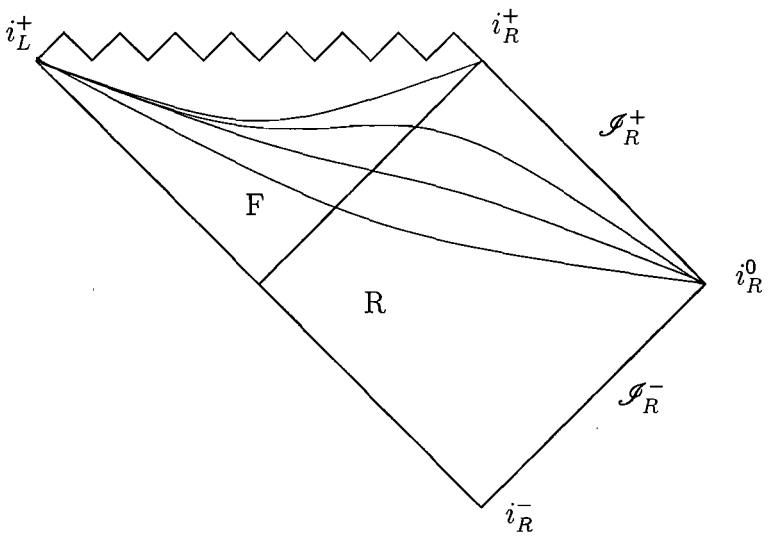


Figure 8.12: The same spacetime diagram, schematically showing the unique regular spherical Killing slicing that is compatible with BMn slicing (for a given $\mu_L(\alpha)$). All slices are isometric to one another, and connect $i_L^+$ with $i_R^0$. The again asymptote to the slice $R = R_0$.

(with $R \to R_0$) and ends at $i_L^+$ avoids this obstruction (Fig. 8.12).

### Excision

An alternative to singularity-avoiding slicings is singularity excision. This means truncating the time slices along a future spacelike surface which is also (at least asymptotically) Killing. In Schwarzschild spacetime, this would be a surface of constant $R < 2M$. One still wants the slice to be Lie-dragged along the Killing field, but one gains more freedom because Killing slices are now acceptable which would intersect the singularity, such as Kerr-Schild slices of Schwarzschild. A Killing slicing with Killing excision boundary is illustrated in Fig. 8.11.

As long as the excision surface is spacelike, all characteristics corresponding to gravitational waves, which propagate on light cones, will be leaving the domain of computation. Depending on the formulation of the Einstein equations and the gauge choice, other characteristics corresponding to constraint modes and gauge

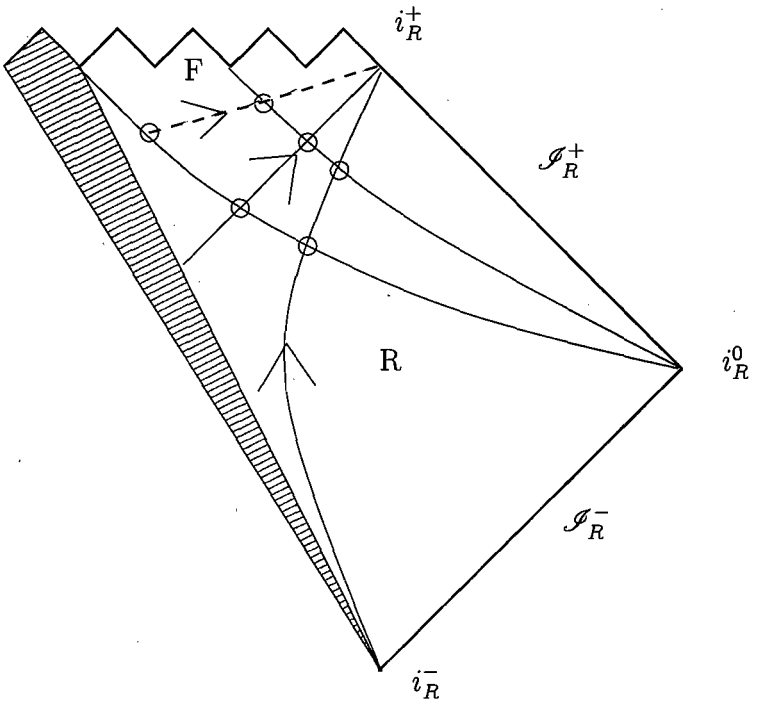


Figure 8.13: Schematic spacetime diagram of the collapse of a spherical star. Outside the collapsing star (shaded) the spacetime is Schwarzschild, comprising parts of regions R and F. A Killing slicing with excision as in Fig. 8.11 is shown. A Killing endstate cannot be reached without excision.

modes may be spacelike, and either this will restrict the excision surface further or explicit boundary conditions need to be imposed on the gauge if the evolution equations are to be well-posed. If the system is not hyperbolic, for example because the gauge conditions are parabolic or elliptic, boundary conditions will be required on any excision boundary.

In [50] and [51], evolutions were carried out from puncture data using BMt 1+log slicing with and without $K_0$, and directly comparing evolutions using either excision or fixed punctures. No explicit boundary condition was imposed at the excision boundary. Excised and non-excised evolutions are claimed to converge to each other to second order everywhere outside the excised region. This is surprising given that the excision problem was ill-posed (the gauge characteristic cone always has one leg pointing into the computational domain cf. 7.18).

### 8.4.2 Killing coordinates on Schwarzschild spacetime in spherical symmetry

We now restrict to spherically symmetric Killing coordinate systems on the Kruskal extension of Schwarzschild spacetime. In the following, $X^\mu$ are preferred coordinates on a given spacetime such as Schwarzschild, while $(t, x^i)$ are the coordinates used for the numerical evolution, in our case with the spherical line element

$$ds^2 = -\alpha^2\, dt^2 + \gamma(dr + \beta\, dt)^2 + R^2\, d\Omega^2. \tag{8.84}$$

We use the shorthands $d\Omega^2 \equiv d\theta^2 + \sin^2\theta\, d\varphi^2$, $R^2 \equiv \gamma_{\theta\theta}$, $\gamma \equiv \gamma_{rr}$ and $\beta \equiv \beta^r$. We use $\dot{f}$ and $f'$ for the partial derivatives with respect to $t$ and $r$.

We use preferred coordinates $(T, R)$ on Schwarzschild with the property that $R$ is the area radius and the Killing vector is $\partial/\partial T$, normalised to unity at infinity, for example Schwarzschild or Kerr-Schild coordinates. In all such coordinates $g_{TT} = 1 - 2M/R$ and $g_{TT}g_{RR} - g_{TR}^2 = -1$.The generic Killing coordinate system $(t, r)$

with $C = 1$ is then given by the ansatz

$$T = t + F(r), \quad R = R(r). \tag{8.85}$$

If we are interested only in the slicing, we can fix the spatial coordinate $r$ for convenience. A better choice than using $R$ itself as a coordinate is to make $r$ proper distance along the slice, so that $\gamma = 1$. (We shall also use the symbol $l$ for proper radial distance.) The Killing lapse and shift are

$$\alpha = R', \tag{8.86}$$

$$\beta = \sqrt{\alpha^2 - 1 + \frac{2M}{R}}. \tag{8.87}$$

The trace of the extrinsic curvature of the Killing slices is

$$K = 2\frac{\beta}{R} + \frac{\beta'}{R'}, \tag{8.88}$$

where $\beta$ is given by (8.87).

### 8.4.3 Compatibility of Killing coordinates with BMn slicing on Schwarzschild spacetime

This subsection reviews and generalises [48]. The BMn Killing slicing condition in spherical symmetry is

$$\beta\alpha' = \mu_L(\alpha)\alpha^2 K. \tag{8.89}$$

Using (8.86) and (8.88) to eliminate $\alpha$ and $K$ gives

$$-\frac{R''}{R'\,\mu_L(R')} + \frac{\beta'}{\beta} + 2\frac{R'}{R} = 0, \tag{8.90}$$

which has an obvious first integral that can be expressed, using (8.86) and (8.87), as

$$-2\int^{R'} \frac{d\alpha}{\alpha\,\mu_L(\alpha)} + \ln\left[\left(R'^2 - 1 + \frac{2M}{R}\right)R^4\right] = c. \tag{8.91}$$

Alternatively, using (8.87) to eliminate $\beta$ from (8.90) gives

$$R'' = -\frac{\mu_L}{R}\frac{N}{D}, \tag{8.92}$$

where

$$N \equiv R'^2\left(2R'^2 - 2 + \frac{3M}{R}\right), \tag{8.93}$$

$$D \equiv [\mu_L(R') - 1]R'^2 + 1 - \frac{2M}{R}. \tag{8.94}$$

For given $\mu_L(\alpha)$ this is a second order ODE for $R(r)$. For the solution to be regular for all $R > 0$, $N$ and $D$ have to vanish at the same $r$, which becomes a regular singular point. This fixes $R$ and $R'$ at this $r$, and hence the constant $c$ in (8.91). (8.91) can then be solved as a first-order ODE for $R(r)$. This means that for any $\mu_L(\alpha)$, there are at most a finite number of twice differentiable spherically symmetric Killing slicings of Schwarzschild, one for each possible regular singular point.

**1+log slicing** The case of 1+log slicing, $\mu_L = 2/\alpha$ has been presented in [48], based on earlier work in [49]. There are two possibilities for regular singular points. One is $R = 2M$ with $R' = 0$. This gives a Killing slicing where each slice goes through the bifurcation point of the horizon, the lapse is positive in R and negative in L, and the slices never reach P or F. It is not of interest for numerical evolutions.

The other regular singular point is $R' = R'_c \equiv -3 + \sqrt{10}$, $R = R_c \equiv M/(4R'_c) \simeq 1.54057M$. In this solution $R \to \infty$ as $r \to \infty$ and $R \to R_0$ from above as $r \to -\infty$. $R_0$ can be found from (8.91) with $R' = 0$, is given in implicit form in [48], and is approximately $R_0 \simeq 1.31241M$. Inside the black hole the slices become asymptotically tangent to the Killing field and terminate at $i^+_L$. The intrinsic geometry of each slice becomes a cylinder of radius $R_0$ as $r \to -\infty$ (Fig. 8.12).

**Harmonic slicing** Harmonic slicing is the special case of BMn slicing with $\mu_L = 1$. The regular singular points are then $R = 2M$ with either $R' = 0$ or $R' = \pm 1/2$. The former can be discarded, and the sign in the latter is trivial, so that the Killing slices are characterised by $\alpha = R' = 1/2$ at $R = 2M$. These slices stretch from $i^0_R$ to the future singularity $R = 0$, and so must be used with excision. The gauge

characteristics are the light cones [17], so the gauge only requires the excision boundary to be spacelike.

**General $\mu_L(\alpha)$** Killing slices cannot have an extremum of $R$ if they are to be stationary points of some slicing condition. From (8.91) we see that if the Killing slices are to approach $i_L^+$, that is $\lim_{r\to\infty} R = R_0 > 0$, the integral

$$\int^0 \frac{d\alpha}{\alpha\,\mu_L(\alpha)} \tag{8.95}$$

must be finite, for example with $\mu_L = 2/\alpha$. We conjecture that, conversely, if this integral diverges, as with $\mu_L = 1$, the Killing slices must intersect the future singularity.

**Excision and uniqueness** One might think that excising a BMn Killing slice would make it less rigid, because the regular singular point $R = R_c$ could be excised. This is correct if one excises at $R_c < R < 2M$ and imposes an explicit boundary condition on the slicing, for example by fixing $\alpha$ at the excision boundary. By function counting one would expect the value of $\alpha$ at the boundary to control the value of the constant $c$ of the slice. However, to excise all modes including the lapse gauge modes, the excision boundary must be in the region where $D < 0$, and so $R = R_c$ must be on the slice. The only possible Killing endstate of the slicing is then the unique one derived above.

### 8.4.4 Initial data

#### Pure gauge data

We use KS coordinates for the background Schwarzschild spacetime. Simple closed form slices which become asymptotically cylindrical at $R = R_0$ may be constructed by making the ansatz $T = t + F(R)$ with

$$F'(R) \simeq -L(R - R_0)^{-1}. \tag{8.96}$$

Constructing 1+log Killing data is straightforward in area gauge where $r = R$. We note that proper distance $l$ is $dl = \sqrt{\gamma} dR$ in area gauge $r = R$, while $R' = dR/dl$ in proper distance gauge $r = l$. Therefore, we obtain an algebraic expression for $\gamma$ in area gauge by replacing $R'$ by $\sqrt{\gamma}$ in (8.91). A single numerical integral must be performed to compute $F(r)$.

A surface with the required isometry in the F region, with a radial coordinate $r$ in which the isometry is $r \to -r$, can be given in Schwarzschild coordinates $(\eta, R)$ as $R(-r) = R(r)$ and $\eta(-r) - \eta_* = -(\eta(r) - \eta_*)$. Here $\eta = \eta_*$ is the reflection surface. Note it is timelike in F. The last condition must be translated into a relation between $T(-r)$ and $T(r)$ using $\eta = T - \phi(R)$ where $\phi(R) \equiv 2M \ln(1 - 2M/R)$. Furthermore, we want the Kerr-Schild time $T$ to be smooth through $R = 2M$, while $\phi(R)$ is not. An ansatz with these properties is

$$T(r) = C(r)r + [1 + D(r)]\phi(R(r)), \tag{8.97}$$

where $C(r)$ and $D(r)$ are smooth odd functions and $D(r)$ is 0 at $r = 0$ and $-1$ on and outside the horizon. To preserve the isometry and the adapted radial coordinate in the evolution the lapse and shift must obey $\alpha(-r) = \alpha(r)$, $\beta(-r) = -\beta(r)$.

### Wormhole initial data for the Einstein equations

To create a numerical evolution in spherical symmetry that is similar to the BSSN moving puncture evolutions in 3D, we use the well-known isotropic radial coordinate

$$R(r) = \left(1 + \frac{M}{2r}\right)^2 r, \tag{8.98}$$

with range $0 < r < \infty$. We use the spherical NOR system described in Sect. 4.6.3, stagger the grid around $r = 0$, and impose as boundary conditions at $r = 0$ that $\gamma_{rr}$, $R$ and $\alpha$ are even in $r$, and $f_r$ and $\beta$ are odd. These conditions hold for the puncture initial data, and it is easy to see that they are compatible with the

time evolution. If $r = 0$ is a regular centre of spherical symmetry, then $(-r, \theta, \varphi)$ represents the same point as $(r, \pi - \theta, \varphi + \pi)$, and these conditions follow from spherical symmetry and regularity. If $r = 0$ represents $i^0_L$ then $r < 0$ is simply not part of the spacetime, the even/odd conditions do not follow from spherical symmetry, and their meaning is unclear. However, for finite differencing purposes they are equivalent to finite differencing across the puncture $x = y = z = 0$ in 3D *as if* it was a regular point, which is what is done in 3D puncture evolutions. Of course in the isotropic radial coordinate the metric is singular at the origin. To get around this problem the evolved variables are rescaled by their analytic growth; the evolved variables are everywhere regular.

In order to resolve both sides of the wormhole, we use the symmetric radial coordinate

$$R(r) = \sqrt{r^2 + 4M^2}, \tag{8.99}$$

with range $-\infty < r < \infty$, and impose isometry boundary conditions at $r = 0$.

### 8.4.5 Black hole evolutions

#### Method

To see empirically if generic black hole evolutions are attracted to the Killing states we have characterised above, we have carried out numerical evolutions of the Schwarzschild spacetime in spherical symmetry, using BMn 1+log slicing.

We can take advantage of the fact that this metric is known in closed form to evolve only the coordinates on the known spacetime, see Sect. 7.1. There is no global coordinate system that covers wormhole slices and which is also Killing. Therefore, in pure gauge evolutions of wormhole slices stretching from $i^0_R$ to $i^0_L$, we restrict to slices with a discrete "left-right" isometry through the coordinate sphere $r = 0$, so that we only evolve explicitly on F and R, where KS coordinates can be used, with a boundary condition at $r = 0$ representing the isometry.

Even this does not work for slices which go through the horizon bifurcation 2-sphere (where KS time and similar Killing time coordinates are $-\infty$), and so for such slices we need to evolve the Einstein equations in the NOR formulation (see Sect. 8.4.4). In all other cases, plots are from pure gauge evolutions, but we have verified that our results are replicated in evolutions of the full Einstein equations in the NOR formulation. The evolutions described here all use the fn-driver shift condition (4.94) except otherwise stated.

### With excision boundary

As initial data for the geometry and the coordinates we have considered:

1a) KS slice, KS lapse, KS shift, area radius;

1b) KS slice, KS lapse, zero shift, area radius;

2) A closed form asymptotically cylindrical slice, unit lapse, zero shift, area radius, see Sect. 8.4.4.

3) The BMn Killing slice, lapse, shift, all in area radius, see Sect. 8.4.4.

We first evolved with area locking (that is, Killing) shift (which is determined algebraically so that the initial value of the shift listed above is irrelevant) and excision. We excised at $R = 1.54M$, which is just inside the maximal excision radius $R = R_c \simeq 1.54057M$ for which all modes are outgoing. We find that 1) and 2) approach the Killing state, and 3) remains there. This is demonstrated in Fig. 8.14, and indicates that the Killing state has a significant basin of attraction.

When combined with the fn shift driver, in 1a) the coordinates $r$ are pushed out of the black hole and further. 1b), and 2) again settle down to the Killing endstate, and 3) remains there. With 1b), the excision radius initially has to be $R \simeq 1.3M$ or the excision surface at constant $r$ will be pushed out so far before it reaches steady state that there a gauge mode is ingoing.

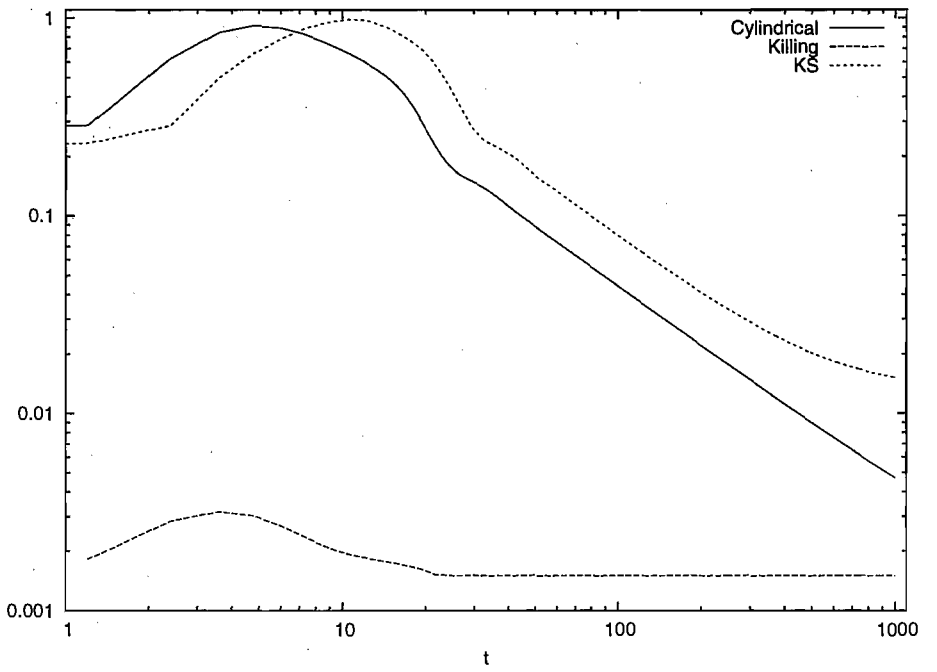


Figure 8.14: The $L^2$ distance of the lapse from the Killing endstate over the range from the excision boundary $R = 1.54$ (just inside the regular singular point) out to $R = 21.54$, with area locking shift. The power law decay indicates $||\alpha - \alpha_{\text{Killing}}|| \sim t^{-1}$.

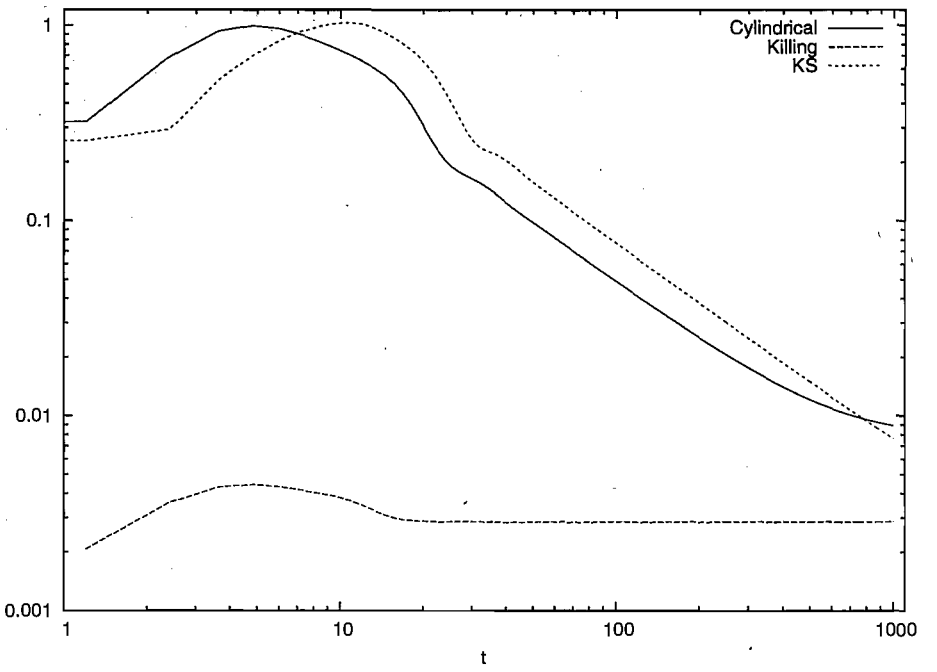


Figure 8.15: The $L^2$ distance of the lapse from the Killing endstate from the excision boundary with approximately the same limits as in Fig. 8.14, using the fn shift driver (4.94). The power law decay again indicates $||\alpha - \alpha_{\text{Killing}}|| \sim t^{-1}$.

### With isometry boundary condition

We begin with NOR evolutions starting from the time-symmetric wormhole slice that goes through the bifurcation 2-sphere $R = 2M$.

We first use spatial coordinates in which $i^0_L$ is represented by the point $r = 0$ (the "puncture"), see Sect. 8.4.4. Evolutions with this method reproduce the behaviour described in [48]: numerical error changes the topology and the evolution settles down to the asymptotically cylindrical Killing state.

If we evolve the same initial data in spatial coordinates that resolve the wormhole (see Sect. 8.4.4), we see the slices begin to form a cylinder at radius $R_0$, but at reasonable resolution constraint violation in the Einstein code makes the result unreliable soon after.

Pure gauge evolutions with wormhole initial data that lie to the future of the bifurcation 2-sphere (so that $R < 2M$ at the throat) and a discrete isometry boundary as described in Sect. 8.4.4 are more stable. At the isometry boundary (where $R$ is minimal) the lapse quickly collapses. In low resolution evolutions, the lapse collapses starting at the minimal $R$ (at the isometry boundary), and a cylinder of radius $R_0$ forms with proper length increasing linearly in time (Fig. 8.16).

### Gauge shocks

However, higher resolution (for example $\Delta r = M/50$) evolutions show that low resolution only hides the formation of a gauge shock where $K$ forms a large negative peak and $\alpha''$ forms a positive peak, at $R \simeq 1.5M$. This does not seem to happen exactly at $R_c$ (we varied $\mu_L(\alpha)$ to check this), and so we do not think that it is a kink instability related to the regular singular point of the Killing endstate slice. Neither is there any indication that the slice has become null. An ODE mechanism by which $K < 0$ makes $\alpha$ grow is also ruled out as not all initial data where $K < 0$ shock.

Rather, we think we see a gauge shock of the type described by Alcubierre [52, 53]. Note that the lapse speeds expressed in terms of proper distance $l$ per coordinate time $t$, relative to the time lines, are $-\beta \pm \alpha\sqrt{\mu_L} = -\beta \pm \sqrt{2\alpha}$, so that a gauge wave propagating "left", from high to low $\alpha$ is expected to steepen. By contrast, the wave propagating "right" and forming the cylinder appears to be stable and translating with constant speed $dl/dt$ without changing its shape much. Alcubierre notes that for the particular choice $\mu_L = 1+k/\alpha^2$ with $k > 0$ the pure gauge system is linearly degenerate, and we have tried this $\mu_L$, but shocks still form, also in agreement with Alcubierre's numerical observations. Alcubierre argues that gauge shocks are generic for evolved gauge conditions.

Although the NOR evolutions of the time-symmetric slice are less reliable, they suggest that evolutions shock when $\alpha$ has a local minimum not at the isometry boundary (Fig. 8.18). They also suggest that with $\alpha = 1$ initially the slicing never shocks (Fig. 8.17). This agrees with the standard numerical literature where the puncture data are approximately the time-symmetric slice through Schwarzschild and the initial lapse is one. It also agrees with the evolution by Brown [54] of these particular initial data. It seem plausible that initial data in a neighbourhood also do not develop shocks, but we have not investigated this.

We note that the shift remains regular during the blow-up, and the same qualitative picture occurs with proper distance radius, zero shift, or fn driver shift.

With BMt slicing and the ft (not fn) shift driver, we see the same gauge shock in both NOR and pure gauge evolutions, but it seems to form earlier and even at low resolution, so that we never see formation of a cylinder before the code crashes.

A troublesome implication of the preceeding analysis and numerical results is that gauge-shocks will generically form in evolutions with Bona-Massó slicing conditions. Why are shocks not seen in puncture evolutions? For some nonlinear wave equations (notably Burgers' equation and the the p-system [5]) it is possible to determine exactly what initial data will evolve to form shocks. For the systems we

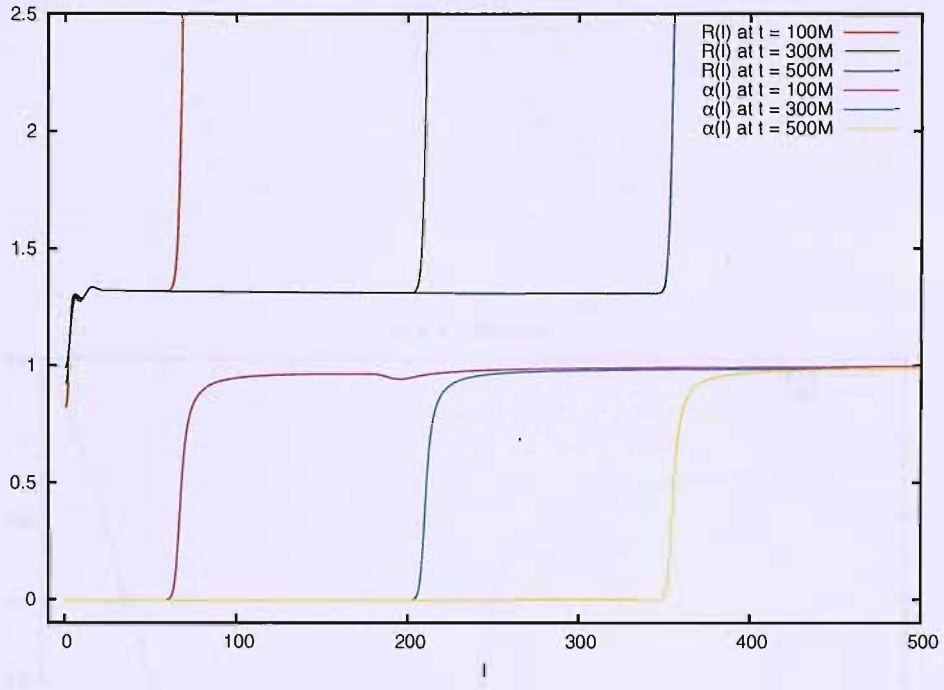


Figure 8.16: Snapshots of $R$ and $\alpha$ against proper distance $l$ from an evolution of an isometric slice as constructed in the "wormhole initial data" subsection 8.4.4. The throat of the slice (initially at $R = 1.5M$) is gradually stretched so that it becomes an infinitely long cylinder. The radius of the cylinder agrees with that computed in [48]. Note that low numerical resolution effectively smears out a gauge shock travelling left, so that this is not a correct continuum solution. The evolution was made with the spherical pure gauge system.

are interested in such analysis is cumbersome. However under the assumption that the field is quiescent in all but a region of compact support the problem may be tractable. One could consider as a toy problem the nonlinear wave equation that forms the principal part of the spherical collapse system discussed in the spherical collapse system evolved numerically in [2],

$$\dot{\alpha} = -2\alpha K, \tag{8.100}$$

$$\dot{K} = -\alpha''. \tag{8.101}$$

This calculation is left for future work.

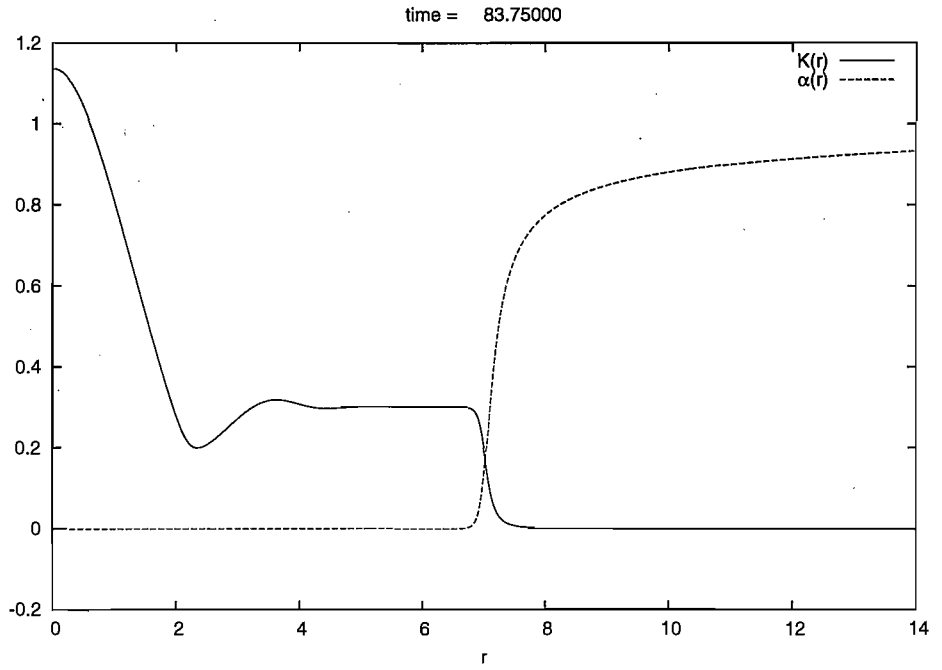


Figure 8.17: The $K = 0$ time symmetric slice through the bifurcation surface of Schwarzschild, evolved with BMn 1+log slicing, with $\alpha = 1$ initially. We show a snapshot of $K$ and $\alpha$ against proper distance radius. The edge at $r \simeq 7$ in this snapshot moves to the right, and leaves behind a cylinder of constant $R$ and $K$ with $\alpha \simeq 0$. The evolution was made with the full spherical NOR system.

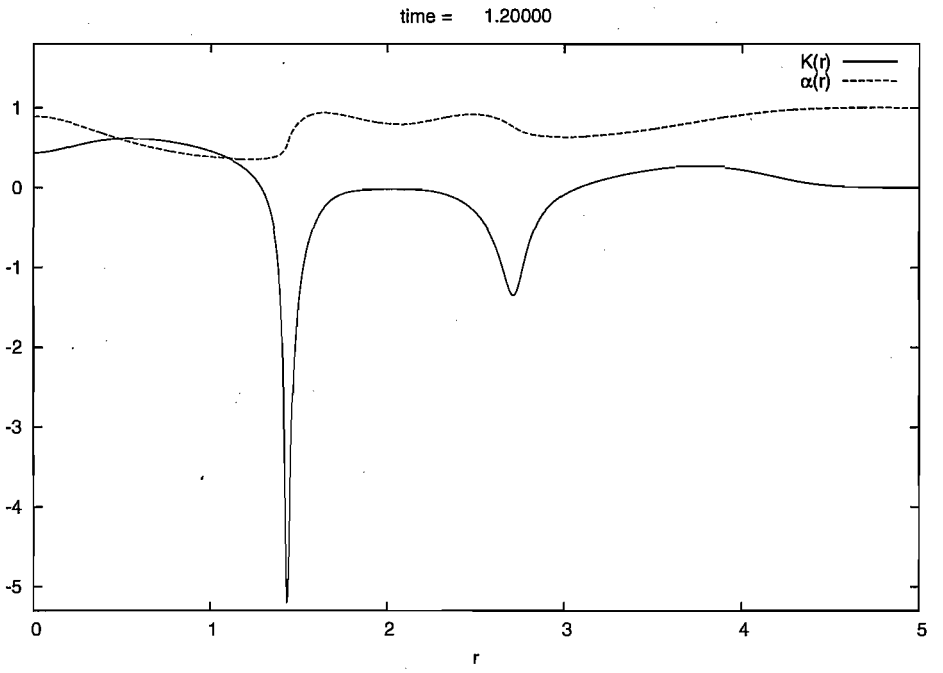


Figure 8.18: As in Fig. (8.17), but with $\alpha$ not constant on the initial slice. The wave on the left travels left and is steepening, about to form a gauge shock, with large negative $K$. The wave on the right travels right and is also steepening: note $\alpha'' > 0$ there.

### 8.4.6 Discussion

**Killing endstates** We have explained why it is possible in evolutions of black holes that all metric coefficients become time-independent without either slice stretching or collapse of the lapse. We have reviewed the Bona-Massó slicing conditions, and have derived a mixed elliptic/hyperbolic PDE on the slice that characterises Killing endstates of the BMn family of slicing conditions. Numerically, we have shown that spherical BMn slicings of the Schwarzschild spacetime are attracted to the Killing endstate from nearby initial data. We do not fully understand the mechanism for this. Initial data further away also appear to be attracted to the Killing state, but on closer inspection this is true only at low numerical resolution.

**Gauge shocks** Increasing the resolution reveals that in the continuum the 1+log BMn slicing *generically* develops gauge shocks of the type described by Alcubierre [52], where the speed of gauge waves associated with the slicing increases with the lapse, so that gauge waves moving from large to small lapse steepen. The only initial data set we have examined that does *not* form a gauge shock with BMn 1+log slicing is the time-symmetric wormhole slice through Schwarzschild spacetime with unit initial lapse, although we suspect that there is at least a neighbourhood of such data. More numerical work is required to explore this.

It may be that gauge shocks would also occur in binary black hole simulations with 1+log BMn slicing in the continuum, but that they are suppressed by low resolution inside the black holes. By contrast, in collapse simulations the central region is typically adequately resolved, and in fact recent work where the collapsing region is never excised seems to require large dissipation for stability [55] (predominantly to control the matter part of the evolution).

**Excision** We find that in both collapse and vacuum simulations the gauge shock can typically be avoided by excising just inside the apparent horizon. There seems to be no clear awareness in the literature that such a boundary still has an incoming gauge mode, and that the resulting continuum problem is ill-posed.

Confirming this, our vacuum (both Einstein and pure gauge) evolutions in spherical symmetry do not converge and often blow up when an incoming mode at the excision boundary is neglected. By contrast, our collapse code, which uses different numerical methods, does not seem to mind. There is also an explicit claim that 3D binary black hole evolutions converge equally well with and without excision [50, 51].

We have also re-derived the previously known [17] fact that if gauge drivers are not of the form $\dot{\alpha} + \beta^i \alpha_{,i} = \ldots$ and $\dot{\beta}^i + \beta^j \beta^i_{,j} = \ldots$, full excision is not possible at any radius.

**Nature of the Killing endstate of BMn slicing** If there is to be no incoming gauge mode at an excision boundary, the equation obeyed by the Killing slice has a transition from elliptic to hyperbolic. Requiring regularity there makes the slice more rigid, and in spherical symmetry makes it unique. The same is true if the slice has no excision boundary.

We have clarified that this unique Killing BMn slicing of a Schwarzschild black connects spacelike infinity outside the black hole to future timelike infinity inside the black hole, where it becomes asymptotically cylindrical. As pointed out independently by Brown [54], initial data which connect two asymptotically flat regions through a wormhole cannot evolve to this endstate in the continuum, although numerical under-resolution gives the false impression that the topology jumps. In the continuum evolution, the wormhole stretches into a cylinder whose length grows without bound.

**Comments on 3D evolutions** In our investigation, we have identified three problems with current gauge choices in 3D numerical evolutions of collapse and black holes with a currently favoured slicing condition, BMn 1+log slicing: 1) wormhole data do not admit a BMn Killing endstate; 2) excision close inside the apparent horizon requires explicit boundary conditions for the gauge; and 3) coordinate shocks form generically. None of these problems have been noted in the binary black hole literature, but we believe that this is only because of limited resolution, and that they will become apparent as a failure of convergence or instabilities at sufficiently high resolution. There are, however, simple ways around these problems:

- Wormhole initial data for eternal black holes ending at $i_L^0$ should be replaced by initial data that are asymptotically cylindrical and end at $i_L^+$. Although the data inside the event horizon ought not to affect the interior, there is nothing to stop superliminal gauge effects, or indeed numerical error from leaving the black hole.

- Continuum boundary conditions should be imposed explicitly at excision boundaries for any incoming gauge modes.

- The initial lapse should be chosen such that gauge shocks do not form. This will require more empirical studies in 3D. In collapse without excision, changing to a smoothly collapsed lapse profile once an apparent horizon has formed may be helpful.

## 8.5 Evolution of asymptotically null slices

As in Chap. 7 the focus is again on the case $n = 1$, so that initially the asymptotic growth of the line-element is given by (8.9-8.11) and in particular,

$$F(R) = \sqrt{L^2 + R^2} - L - \frac{L}{2} \ln\left(1 + \frac{R^2}{L^2}\right) + 2M \ln\left(1 + \frac{R^2}{L^2}\right), \quad (8.102)$$

$$R(r) = L \sinh \frac{r}{L}, \quad (8.103)$$

in the Schwarzschild spacetime with Kerr-Schild slices near the blackhole. The flat space slices are a special case with $M = 0$.

The approach will be to build up the complexity of the evolutions gradually.

The runs are performed with a similar configuration to the pure gauge tests of Chap. 7; second or fourth order differences in space, a grid spacing of $h = 0.1M$, constraint damping and constraint preserving boundary conditions (8.73), using principally the BMn 1+log and fn-driver gauge conditions (7.21,7.22)

$$\dot{\alpha} = -2\alpha(K - K_0) + \beta(\alpha' - \alpha'_0) \quad (8.104)$$

$$\dot{\beta} = (f - f_0) + \beta(\beta' - \beta'_0) - \eta(\beta - \beta_0). \quad (8.105)$$

with an outer boundary imposed at a coordinate radius of $r_{max} = 70$, which with $L = 8$ corresponds to an areal radius $R_{max} \simeq 25000M$.

### 8.5.1 Spherical NOR

#### Minkowski evolutions

For the intial test runs presented in this section the asymptotic growth of the evolved variables (8.9-8.11) was factored out of the evolved variables analytically, so that the evolved quantity remains regular at large radius. Note that the continuum system remains unaltered with this change; it is a change of variables only.

As in other flat space evolutions the origin is dealt with by imposing regularity conditions. Tests with densitized lapse and fixed shift are a miserable failure. At

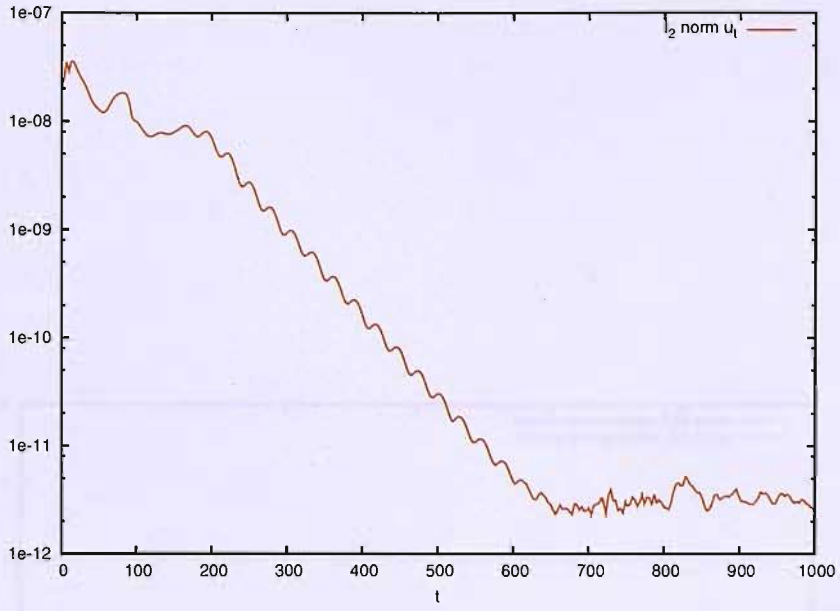


Figure 8.19: The $l2$ norm of the time derivative of the numerical solution. All dynamics cease by $t \simeq 600$.

large radius the solution blows up. Constraint damping does not help, although this is to be expected given the behavior of the system with constraint damping on flat slices. With the evolved gauge the story is much rosier. At both second and fourth order accuracy the evolutions appear to be able to run essentially forever, although with the outer boundary at $25000M$ it is impractical to run the code for many light crossing times. The evolutions are stopped after one crossing time. All dynamics cease by $t \simeq 220M$, after which the whole system is completely frozen (Fig. 8.19). Shorter self convergence tests are performed, and the results indicate perfect second and fourth order accuracy (Fig. 8.20).

Damped and undamped evolutions are compared in Fig. 8.21. Constraint damping prevents undesirable growth at large radius.

Simply being able to evolve flat space in some non-standard coordinates is not terribly impressive. These tests can however be made more robust by pertubing the lapse or shift in the central, flat-slice region and observing the behavior of the

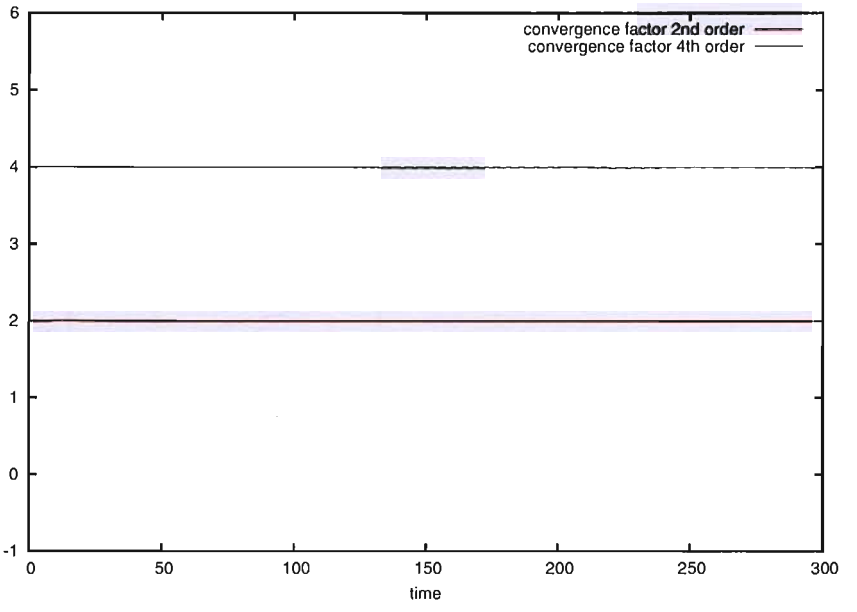


Figure 8.20: Convergence factors for the second and fourth order accurate schemes. The evolutions also display perfect pointwise convergence to the appropriate order.

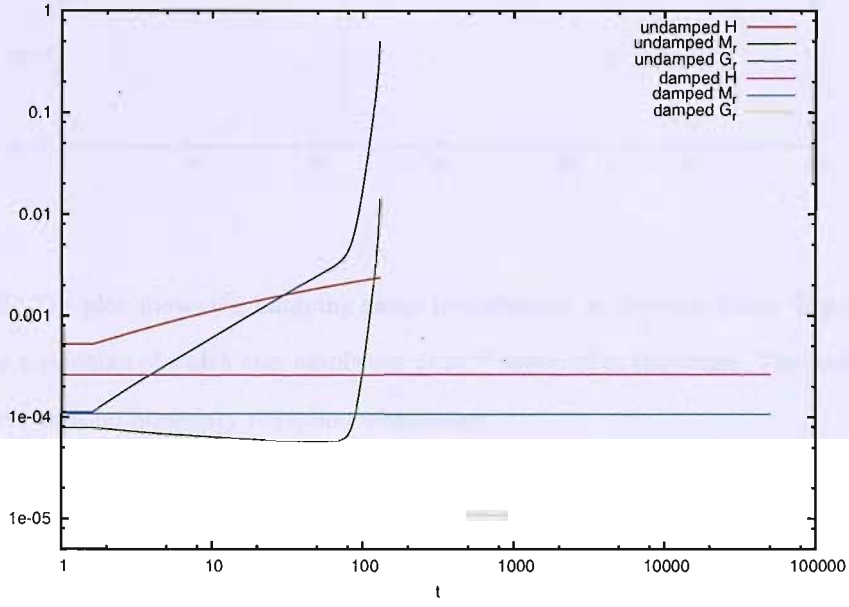


Figure 8.21: This plot compares the growth of constraints on asymptotically null slices in the Minkowski spacetime with and without damping. Clearly damping is essential to keep the constraints under control on asymptotically null slices.

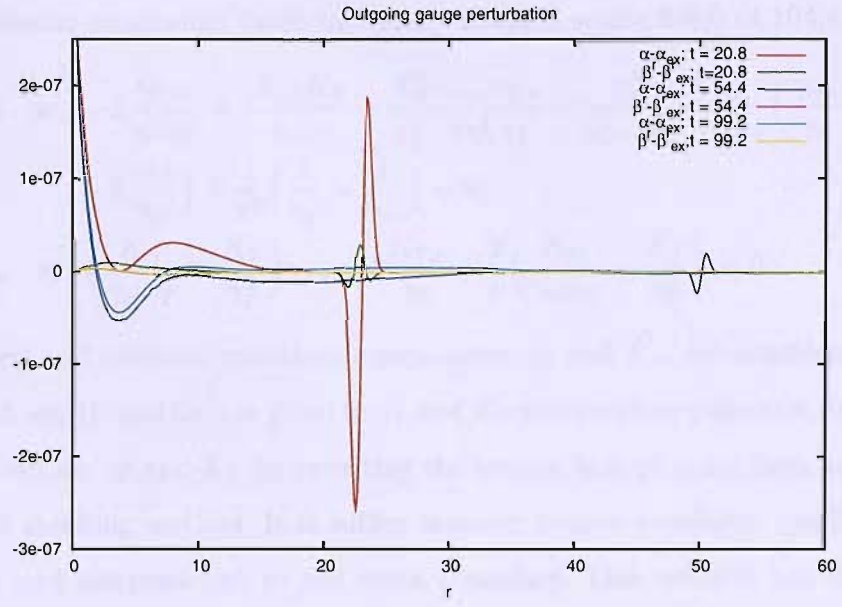


Figure 8.22: The plot shows the outgoing gauge perturbation at different times. The lapse was perturbed by a gaussian of width one, amplitude $1x10^{-4}$ centered at the origin. The perturbation leaves the grid with no boundary reflection whatsoever.

pertubation as it evolves. Altering the size of the perturbation allows the robustness of the system to be studied in a simple context.

Small gaussian perturbations centered at the origin are made to the initial lapse profile. The source terms in the gauge condition are taken from the unperturbed system. Fig. 8.22 shows the outgoing perturbation leaving the numerical domain of evolution. Table 8.1 summarizes the behavior of the system under perturbations of varying amplitude.

The next natural step is to evolve the system with a small scalar field. For simplicity the scalar field is not centered at the origin. The constraints are solved in an ad-hoc method tailored to spherical symmetry. In spherical coordinates the Hamiltonian

and momentum constraints (with minimally coupled scalar field) (4.104,4.105),

$$H \equiv -2\frac{\gamma_{T,rr}}{\gamma_{rr}\gamma_T} + 2\frac{K_{rr}K_T}{\gamma_{rr}\gamma_T} + \frac{K_T^2}{\gamma_T^2}\frac{\gamma_{rr,r}\gamma_{T,r}}{2\gamma_{rr}^2\gamma_T} + \frac{\gamma_T^2}{4\gamma_{rr}\gamma_T^2} + \frac{1}{r\gamma_{rr}}\Big(\frac{\gamma_{rr,r}}{\gamma_{rr}} - 3\frac{\gamma_{T,r}}{\gamma_T}\Big) + \frac{1}{r^2}\Big(\frac{1}{\gamma_T} - \frac{1}{\gamma_{rr}}\Big) = 0, \tag{8.106}$$

$$M_r \equiv \Big(\frac{K_{rr}}{\gamma_{rr}\gamma_T} + \frac{K_T}{\gamma_T^2}\Big)\gamma_{T,r} - 2\frac{K_{T,r}}{\gamma_T} + \frac{2}{r}\Big(\frac{K_{rr}}{\gamma_{rr}\gamma_T} + \frac{K_T}{\gamma_T^2}\Big) = 0. \tag{8.107}$$

If the metric and extrinsic curvature components $\gamma_{rr}$ and $K_{rr}$ are considered given alongside $\phi$ and $\Pi$, and data is given to $\gamma_T$ and $K_T$ at boundary points (4.104,4.105) can be solved for $\gamma_T$ and $K_T$ by rewriting the system in first order form and using a standard shooting method. It is suffice however to give regularity conditions at the origin and integrate out to the outer boundary. This method has the additional effect of altering the slicing outside the scalar-field pulse. The results of the evolutions are summarized in table 8.1. Small pertubations cause no significant problems.

| Gauge Pert. | $L_2$ distance, $t =$ | | | Scalar field | $L_2$ distance, $t =$ | | |
|---|---|---|---|---|---|---|---|
| magnitude | 33.6 | 65.6 | 99.2 | Pert. magnitude | 33.6 | 65.6 | 99.2 |
| $1 \times 10^{-2}$ | $1.67\times10^{-4}$ | $1.13\times10^{-4}$ | $1.13\times10^{-5}$ | $1 \times 10^{-2}$ | $9.98\times10^{-3}$ | $6.57\times10^{-3}$ | $7.08\times10^{-3}$ |
| $1 \times 10^{-4}$ | $1.22\times10^{-6}$ | $1.20\times10^{-6}$ | $7.16\times10^{-6}$ | $1 \times 10^{-4}$ | $1.22\times10^{-6}$ | $7.41\times10^{-7}$ | $9.70\times10^{-7}$ |
| $1 \times 10^{-6}$ | $5.23\times10^{-7}$ | $5.33\times10^{-7}$ | $6.70\times10^{-7}$ | $1 \times 10^{-6}$ | $3.63\times10^{-7}$ | $4.20\times10^{-7}$ | $5.63\times10^{-7}$ |

Table 8.1: $L_2$ distances of the perturbed solution from the static solution. With a very small perturbation, numerical error dominates the distance. These tests were made with the fourth order accurate scheme.

More robust tests could be made by making the scalar field sufficiently large that it will collapse to form a blackhole. To do this the scalar field perturbation could be centered further out. A coordinate width of one in the region where the slice raises corresponds to large width in areal radius and so the scalar field could contain

sufficient energy, (assuming a mostly incoming field), perhaps without bending the coordinates too much.

Instead of this approach, a gauge perturbation of varying magnitude is made until some pathological behavior is found. As seen in Sect. 8.4, a typical way for a blackhole to be dealt with on a numerical grid is by representing the hole as a puncture on the grid. The lapse then collapses at the hole. The effect of the collapsed lapse on an asymptotically null slice can be mimicked in flat space by reducing the lapse significantly at the origin and evolving. Initially subtracting a gaussian (again of width one) with amplitude 0.95 causes no ill behavior. The evolution acts in much the same way as that with a smaller gauge perturbation. The perturbation travels outwards and diminishes in magnitude. Small numerical reflections appear at the boundary as the bulk of the perturbation leaves the numerical grid, but they decrease with resolution. The system does not completely escape from gauge shocks however; if a large gauge perturbation is placed away from the origin then the results of Fig. 8.18 are replicated (likewise on flat slices).

### Schwarzschild evolutions

Numerical evolutions with densitized lapse and fixed shift are equally as unsuccessful as those in flat space.

With the evolved gauge it is possible to evolve successfully for coordinate times in excess of $10000M$. The evolutions eventually ($t \simeq 10400M$) blow up at the excision boundary (Fig. 8.24), but in view of the the behavior of the spherical NOR system on flat slices (cf. Sect. 8.3) the blow-up is unsurprising. This observation, coupled with the successful evolutions of asymptotically null slices in the Minkowski spacetime and the fact that the Schwarzschild evolutions remain essentially static away from the excision boundary forces the conclusion that the growth is not caused by the slice becoming null. For direct comparison, on flat slices one sees a similar breakdown at the excision boundary at $t \sim 1100M$. Since increasing the resolu-

tion increases the time of the blowup (cf. table 8.2), we expect that the problem could be mitigated by either mesh refinement, or a more robust way of treating the blackhole boundary, perhaps by representing the blackhole as a puncture [44].

The characteristic speeds of the system are monitored over the grid. At the excision boundary, the $\beta$-speed can be tricky. Typically, although $\beta$ is negative, its magnitude is small, so even a small perturbation can stop the excision boundary from being a true outflow boundary. If it were not for the numerical evolutions with the BSSN system (on flat slices) one might conclude that poor behavior at an excision boundary is generic to all NOR-like systems. It would be interesting to compare the behavior of the BSSN system before and after the conformal decomposition. Is it the continuum system or the change of variables that gives rise to such favorable error properties at the excision boundary?

In spherical symmetry it is straightforward to track the apparent horizon (outermost trapped surface). The apparent horizon finder just solves the system given in [10] in different variables.

| Resolution | Slice | $t_{\text{blowup}}$ | cause | Slice | $t_{\text{blowup}}$ | cause |
|---|---|---|---|---|---|---|
| 0.1 | MK.flat | $> 20000M$ | N/A | KS.flat | $1100M$ | Excision |
| 0.05 | | $> 20000M$ | N/A | | $1280M$ | Excision |
| 0.1 | MK.asy.null | $> 50000M$ | N/A | KS.asy.null | $10400M$ | Excision |
| 0.05 | | $> 50000M$ | N/A | | $> 20000M$ | Excision$^{\dagger}$ |

Table 8.2: Comparing evolution of asymptotically null and flat slices. The evolutions of Minkowski on with flat slices were given an initial gaussian perturbation in the lapse to avoid trivial evolution. The amplitude of the pulse was $1\text{x}10^{-5}$ and it was centered initially at the origin. †: similar behavior can be seen as in the lower resolution case.

To investigate less trivial evolutions in the Schwarzschild spacetime, we choose to perturb the spacetime with a small, mostly ingoing scalar field to see if the interaction with the blackhole has any detrimental effect on the slices away from

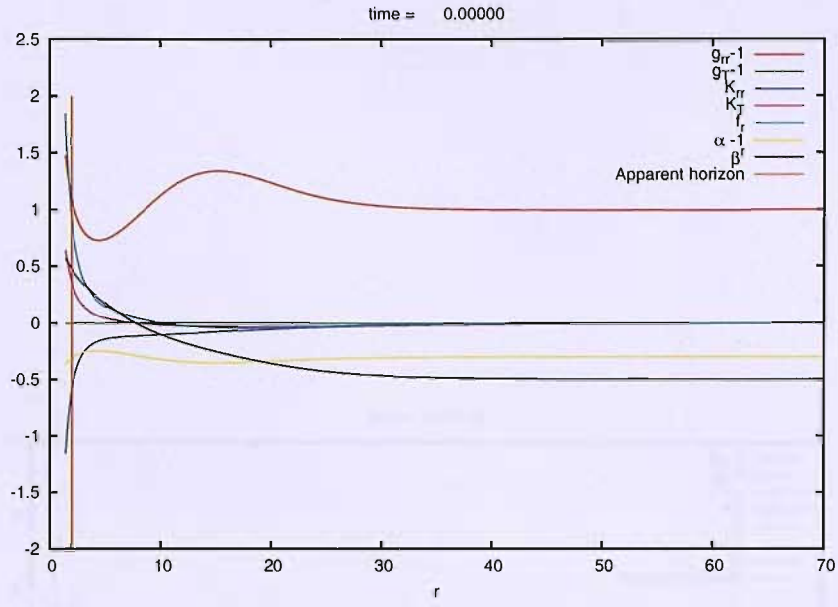


Figure 8.23: This plot shows initial data for asymptotically null evolutions in the Schwarchzschild spacetime.

the strong-field region. To do this the ad-hoc constraint solver described in the previous section was again used. Again the results are promising. Small scalar field perturbations fall into the blackhole, pushing the apparent horizon further out. The far-field region (where the slices become raised) remains basically unaffected.

### 8.5.2 Spherical BSSN

The favourable behavior of the spherical BSSN compared to the spherical NOR system on flat slices, especially at the excision boundary when evolving the Schwarzschild spacetime motivate the use of the spherical BSSN system with asymptotically null slices.

The numerical results in this section were performed without rescaling the evolved variables. However the system presented in Sect. 4.6 is not (unless otherwise stated)

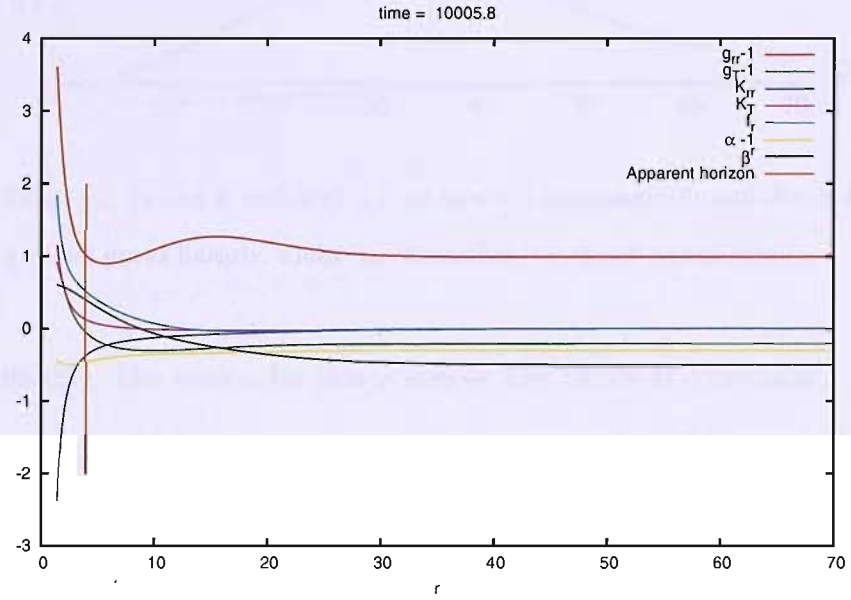


Figure 8.24: This plot shows a snapshot of the data from Fig. (8.23) during the evolution. The slow growth of variables at the excision boundary can be seen. It is this growth that eventually kills the run. The far region of the slice is effectively frozen after about $t \sim 100M$.

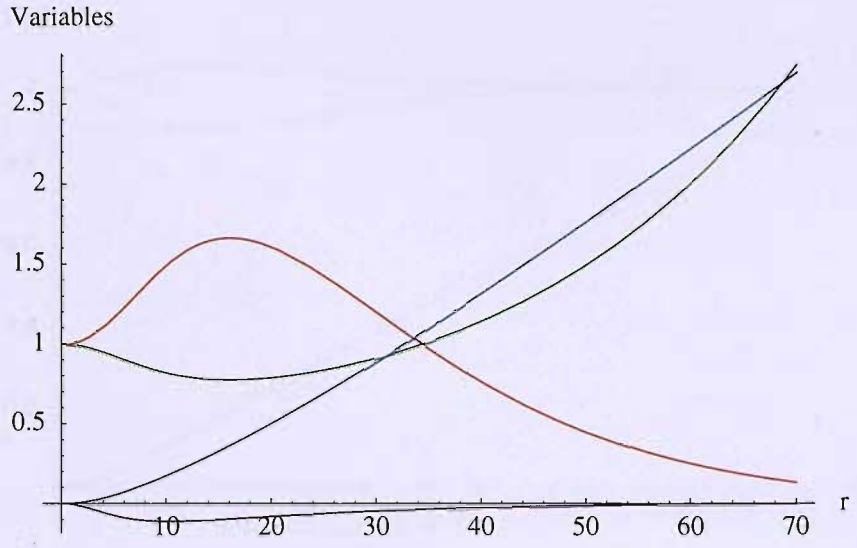


Figure 8.25: $\phi$, $\bar{\gamma}_{rr}$, $\bar{\gamma}_T$ and $K$ with $\tau(r) = r$, on an $n = 1$ asymptotically null slice in Minkowski. Note that $\phi$ (blue) grows linearly, whilst $\bar{\gamma}_{rr}$ diminishes ($\bar{\gamma}_T$ grows) exponentially.

evolved directly. The reason for this is simple; the BSSN $D$ constraint,

$$\ln(\bar{\gamma}_{rr}\bar{\gamma}_T^2) \equiv 0, \tag{8.108}$$

allows pathological behavior in the conformal metric, and subsequently in the auxiliary $\Gamma^i$ variable. For example if the definitions given in Sect. 4.6 are used to define the conformal metric, on asymptotically null slices $\bar{\gamma}_{rr} \to 0$ and $\bar{\gamma}_T \to \infty$ at large radius (Fig. 8.25). If one redefines

$$\phi = \frac{1}{12}\log(\frac{\det\gamma}{\tau^4 \sin^2\theta}), \tag{8.109}$$

and chooses the function $\tau(r)$ carefully then on $n \leq 1$ slices all evolved variables except $\phi$ take finite values in the limit of large radius. In effect, all of the singular behavior of the system has been absorbed by one evolved variable, $\phi$. Better still, this variable is defined with a logarithm; at worst (restricing to $n \leq 1$) it grows linearly with coordinate radius. Fig. 8.26 plots typical initial data for the modified equations.

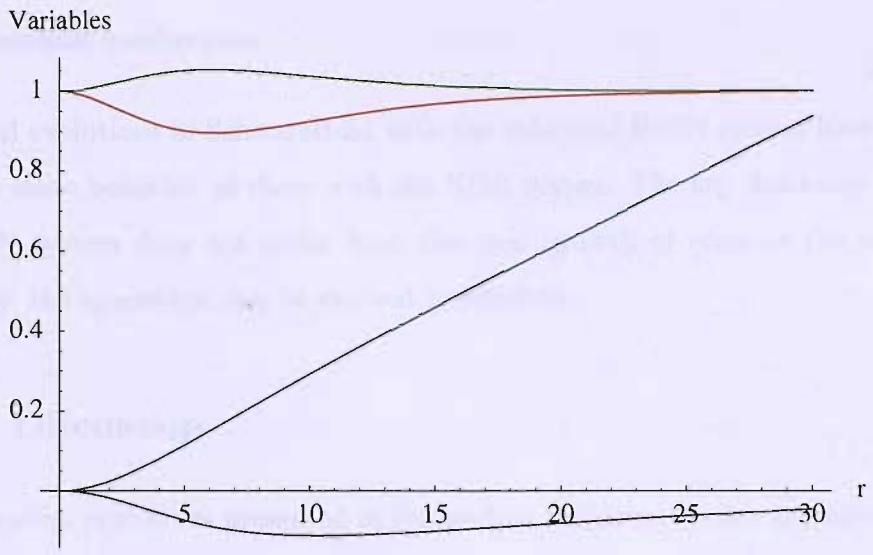


Figure 8.26: As in Fig. 8.25 with $\tau(r) = R(r)(1 + (2R(r)/L)^2)^{-1/4}$. $\phi$ still grows linearly, but $\bar{\gamma}_{rr}$ and $\bar{\gamma}_T$ remain regular at large radius.

### Minkowski evolutions

The numerical tests performed with the spherical NOR system are not all repeated with the BSSN system. Only the most simple tests are repeated.

Numerical evolutions with densitized lapse and fixed shift were not performed.

Numerical tests with evolved lapse and shift give similar results as the NOR evolutions, with one exception: the central region suffers from (relatively) large Hamiltonian constraint violation. Tests on flat slices confirm that the behavior is not caused by the asymptotically null slice. Increasing the dissipation parameter at the origin helps, but does not cure the problem completely. Numerical tests with NOR and $\rho = 2/3$ present similar behavior.

Problems with the constraint damping terms at the outer boundary can be anticipated after the flat slice evolutions in Sect. 8.2.4. In fact on asymptotically null slices there appears to be no problem.

#### Schwarzschild evolutions

Numerical evolutions of Schwarzchild with the spherical BSSN system have essentially the same behavior as those with the NOR system. The key difference is that the BSSN system does not suffer from the slow growth of error at the excision boundary; the spacetime can be evolved indefinitely.

### 8.5.3 Discussion

The numerical evolutions presented in this section indicate that the asymptotically null slices constructed in Chap. 5 can be evolved with a standard formulation used in numerical relativity codes.

There are still questions to be answered in a spherical context. It would be interesting to see whether the spherical puncture method (described in Sect. 8.4) can be adapted to work with asymptotically null slices. Another application for the slices could be collapse evolutions. The benefits of using asymtotically null slices are obvious, but of course there are complications involved in constructing initial data, even, for example with a large scalar field. It would also be interesting to have numerical evolutions of asymptotically null slices with other formulations. Of particular interest are $Z4$ (because of its relationship with the generalized harmonic formulation used by Pretorius), the generalized harmonic formulation and the NOR-$\Theta$ and BSSN-$\Theta$ formulations, which, like $Z4$ have a natural constraint damping scheme for the whole constraint subsystem.

Constructing general initial data will be a challenging problem. Even in spherical symmetry it is unnatural to take the line element in a conformally flat form when constructing asymptotically null slices, and conformal flatness is the key assumption in constructing much of the data numerical relativity codes.

Moving away from spherical symmetry will not be straightforward. There is (of course) no natural radial coordinate. However a multipatch infrastructure such as

that developed by [62, 58] could be naturally invoked. Although the coordinate systems used in these codes are often unintuitive,s uch an approach can be used to achieve a constant angular resolution. With a little work, the partial constraint damping scheme could be added to these standard multipatch codes. The numerical results of Chaps. 6, 7 and 8 indicate that given suitable asymptotically initial data there could be a significant computational advantage to using asymptotically null slices in astrophysical simulations. The outer boundary could feasibly be pushed orders of magnitude larger than is currently possible, allowing more reliable compuation of gravitational wave forms, and of course reducing the chance that wave-forms will be swamped by imperfect data from the outer boundary.

# Chapter 9

# Conclusions

This work has been concerned with the construction of slices of spacetime suitable for the evolution of asymptotically flat spacetimes in numerical relativity.

Popular formulations of the Einstein equations were reviewed. These formulations were faithfully reduced to spherical symmetry for later applications. Partial and full constraint damping schemes for extensions of the NOR, Z4 and BSSN systems were discussed.

Coordinates adapted to the resolution of outgoing gravitational radiation far from a source were constructed. These slicings are asymptotically null in the sense that the Lorentz factor between observers in these slicings and those in coordinates adapted to asymptotic flatness slices diverges in a neighborhood of infinity.

Studying the wave equation in a fixed background in spherical symmetry revealed that the use of asymptotically null slices greatly reduces the computational cost required to evolve a large portion of the spacetime and that in many cases smaller numerical errors may be induced. One may be concerned that although outgoing radiation is well resolved on asymptotically null slices, incoming radiation may be lost. To address these concerns numerical evolutions of the wave equation were made in the Schwarzschild spacetime. Power law decay of the field was clearly

displayed.

One can study the behavior of gauge conditions without studying the full Einstein equations by evolving coordinates on a fixed spacetime. Such evolutions were made of asymptotically null initial data with popular evolved gauge conditions. Without the complication of the Hamiltonian and Momentum constraints it was found possible to evolve such data successfully.

Here the work splits into two related streams. First the behavior live gauge conditions popular in the evolution of binary black holes was studied in the strong-field region. The 1+log Killing endstate reported recently [48] appears to have a significant basin of attraction. We also observed that sufficiently pathological initial data can cause coordinate shocks to form.

The second stream is the evolution of asymptotically null initial data (in spherical symmetry) with the Einstein equations. To do so requires 3 key ingredients; constraint damping, constraint preserving boundary conditions and live gauge conditions.

Constraint damping combined with live gauge conditions which freeze at the desired solution are absolutely essential for asymptotically null initial data. Without damping, the constraints quickly blow up away from the strong field region. To the best of our knowledge this is the first successful use of constraint damping with a BSSN-like formulation.

Constraint preserving boundary conditions are not essential to evolve asymptotically null initial data for long coordinate times, but reducing the constraints near the outer boundary by 5 orders of magnitude makes any physics deduced in that region far more trustworthy.

To evaluate how robust evolutions of asymptotically null intial data are, two types of perturbation were made to the initial data. Firstly, the initial lapse was perturbed in the central region. The aim was to mimic the outgoing behavior of a

large disturbance such as a binary merger. Even with a large perturbation, the slices do not kink, and the numerical solution converges. Secondly small scalar field perturbations were made in the central region. Again the slices do not kink, and the solution continues to converge.

The outlook for asymptotically null slices in numerical relativity is bright. The tests performed in this thesis in spherical symmetry demonstrate that in principle it should be possible to use such initial data in a more realistic scenario.

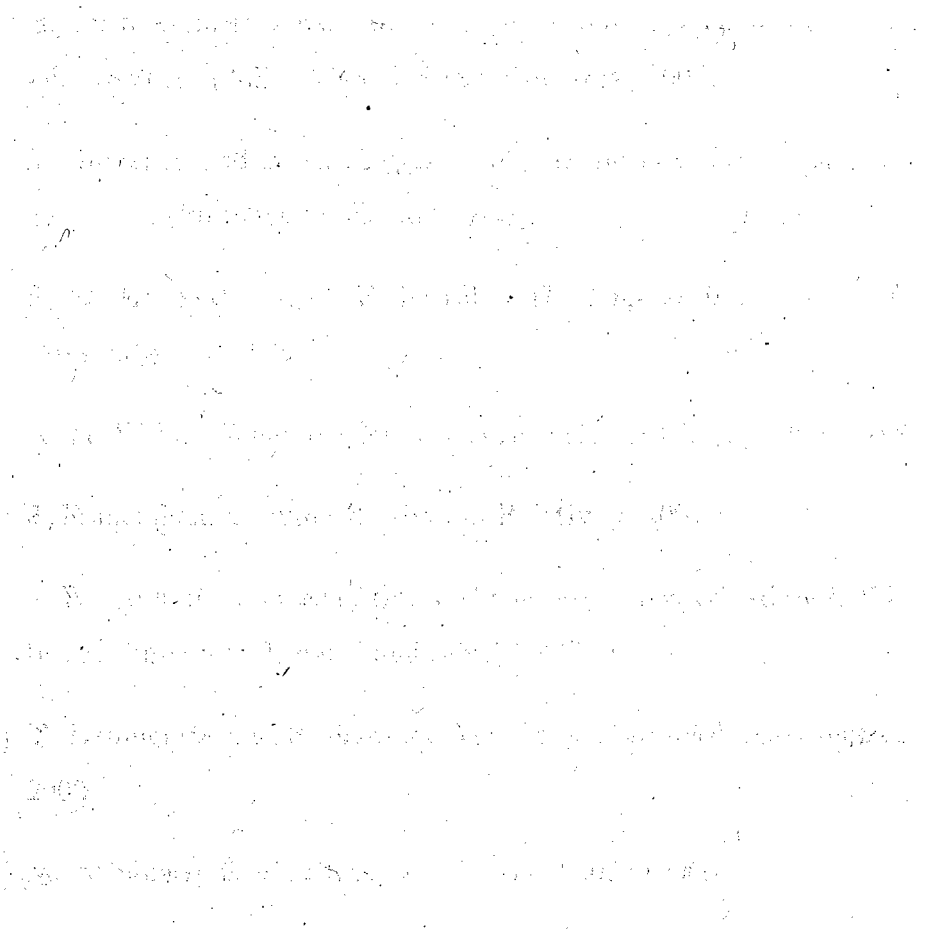

# Bibliography


[1] G. Calabrese, C. Gundlach and D. Hilditch, Class. Quant. Grav. **23**, 4829 (2006).

[2] D. Garfinkle, C. Gundlach and D. Hilditch, eprint arXiv:0707.0626

[3] C. Gundlach, J. M. Martín-Garcıa and I. Hinder, gr-qc/0504114

[4] B. Gustafsson, H. Kreiss and J. Oliger, *Time dependent problems and difference methods* (John Wiley & Sons, New York, 1995).

[5] M. Renardy and R. C. Rogers, 1993, *An introduction to partial differential equations*, (Springer-Verlag New York)

[6] S. W. Hawking and G. F. R. Ellis, *The large scale structure of spacetime*, Cambridge UP 1975.

[7] R. M. Wald, *General Relativity*, (University of Chicago Press, 1984).

[8] J. Frauendiener, Living Reviews in Relativity, 2004-1.

[9] J. W. York, in *Sources of Gravitational Radiation*, edited by L. Smarr, (Cambridge University Press, Cambridge, 1979).

[10] T. Baumgarte and S. Shapiro, *Numerical Relativity and Compact Binaries*, 2002

[11] M. Alcubierre *et al.*, Phys. Rev. D **67**, 084023 (2006).

[12] H. Beyer and O. Sarbach, Phys. Rev. D **70**, 104004 (2004).

[13] Nagy, Ortiz, Reula, Phys. Rev. D **70**, 044012 (2004).

[14] C. Bona and C. Palenzuela, Phys. Rev. D **69**, 104003 (2004).

[15] C. Bona and C. Palenzuela, Phys. Rev. D **69**, 064036 (2004).

[16] C. Bona, T. Ledvinka and C. Palenzuela, Phys. Rev. D **67**, 104005 (2003).

[17] C. Gundlach and J. M. Martín-Garcıa, Phys. Rev. D **74**, 024016 (2006).

[18] Strang, G. Linear Algebra and its Applications, 3rd ed. Philadelphia, PA: Saunders, 1988.

[19] Khoklov and Novikov, Class. Quant. Grav. **19**, 1889 (2002).

[20] E. Seidel and W.-M. Suen, Phys. Rev. Lett. (1992).

[21] C. Bona *et al.*, Phys. Rev. Lett. **95**, 600 (1995).

[22] M. Alcubiere and B. Bruegmann, Phys. Rev. D **63**, 104006 (2001).

[23] S. Bonazzola *et al.*, Phys. Rev. D **70**, 104007 (2004).

[24] F. Pretorius, Phys. Rev. Lett. **95**, 121101 (2005).

[25] H Friedrich and G Nagy, Comm. Math. Phys. **201**, 619 (1999).

[26] G. Calabrese, L. Lehner and M. Tiglio, Phys. Rev. D **65**, 104031 (2002).

[27] L. E. Kidder *et al.*, Phys. Rev. D **71** 064020, (2005).

[28] O. Sarbach and M. Tiglio, Journal of Hyperbolic Differential Equations **2**, 839 (2005).

[29] U. Sperhake *et al.*, Phys. Rev. D **71**, 124042 (2005).

[30] L. Baiotti *et al.*, Phys. Rev. Lett. **94**, 131101 (2005).

[31] M. Miller, Phys. Rev. D **71**, 104016 (2005).

[32] J. Winicour, Living Reviews in Relativity **2005**-10.

[33] E. P. Honda and M. W. Choptuik, Phys. Rev. D **65**, 084037 (2002).

[34] D. Garfinkle and G. C. Duncan, Phys. Rev. D **63**, 044011 (2001).

[35] A. Kansagra, Coordinate compactifications and hyperboloidal slices in numerical relativity, LIGO/Caltech undergraduate project, unpublished (2003). For an online abstract, see http://www.ligo.caltech.edu/LIGO_web/students/ugprojects03.html.

[36] C. Misner, M. Scheel, Wave propagation with hyperboloidal slicings, talk given 12 June 2003 at KITP, unpublished. For an online version see http://online.kitp.ucsb.edu/online/gravity03/misner/. C. Misner, Hyperboloidal slices and artificial cosmology for numerical relativity, e-print gr-qc/0409073. J. R. van Meter, D. R. Fiske, C. W. Misner, Excising das All: Evolving Maxwell waves beyond Scri, e-print gr-qc/0603034.

[37] D Garfinkle and C Gundlach, Class. Quant. Grav. **16**, 4111 (1999).

[38] R. Price, Phys. Rev. D **5**, 2419 (1972).

[39] C. Misner, Hyperboloidal slices and artificial cosmology for numerical relativity, unpublished (2004), gr-qc/0409073.

[40] G. Calabrese and C. Gundlach, Discrete boundary treatment for the shifted wave equation, Class. Quant. Grav. **23**, S343-S368 (2006).

[41] M. Alcubierre *et al.*, Class. Quant. Grav. **20**, 3951 (2003).

[42] C. R. T. Nunn, Masters thesis, Univeristy of Southampton, unpublished.

[43] C. Gundlach and José M. Martin-Garcia, Hyperbolicity of second-order in space systems of evolution equations, Class. Quant. Grav. **23**, S387-S404 (2003).

[44] S. Brandt and B. Brügmann, Phys. Rev. Lett. **78**, 3606 (1997).

[45] J. R. Oppenheimer and H. Snyder, Phys. Rev. **56**, 455 (1939).

[46] M. Alcubierre *et al.*, Phys. Rev. D **67**, 084023 (2003).

[47] D. Garfinkle and C. Gundlach, Class. Quant. Grav. **16**, 4111 (2002).

[48] M. Hannam *et al.*, Geometry and regularity of moving punctures, eprint gr-qc/060699.

[49] F. Estabrook *et al.*, Phys. Rev. D **7**, 2814 (1973).

[50] M. Alcubierre *et al.*, Testing excision techniques for dynamical black hole evolutions, eprint gr-qc/0411137.

[51] M. Alcubierre *et al.*, Phys. Rev. D **72**, 044004 (2005).

[52] M. Alcubierre, Phys. Rev. D **55**, 5981 (1997).

[53] M. Alcubierre, Class. Quant. Grav. **20**, 607 (2003) .

[54] J. D. Brown, Puncture evolutions of Schwarzschild black holes, eprint arXiv:0705.1359.

[55] L. Baiotti and L. Rezzolla, Phys. Rev. Lett. **97**, 141101 (2006).

[56] M. Campanelli *et al.*, Phys. Rev. Lett. **96** 111101 (2006).

[57] J. G. Baker *et al.*, Phys. Rev. Lett. **96**, 111102 (2006).

[58] J. Thornburg, Class. Quant. Grav. **21**, 3665 (2004).

[59] R. Beig and N. Ó Murchada, Phys. Rev. D **57**, 4728 (1998).

[60] O. Brodbeck, S. Fritelli, P. Huebner and O.A. Reula, J. Math. Phys. **40**, 909 (1999).

[61] J. R. van Meter, D. R. Fiske, C. W. Misner, Excising das All: Evolving Maxwell waves beyond Scri, Phys. Rev. D **74**, 064003 (2006).

[62] L. Lehner, O. Reula and M. Tiglio, Multi-block simulations in general relativity: high order discretizations, numerical stability, and applications, Class. Quant. Grav. **22**, 5283 (2005).